Fall 2018

Signal processing for microwave imaging systems with very sparse array

Xiahan Yang

Department: Electrical and Computer Engineering

SIGNAL PROCESSING FOR MICROWAVE IMAGING SYSTEMS WITH VERY SPARSE ARRAY

by

XIAHAN YANG

A DISSERTATION

Presented to the Graduate Faculty of the

MISSOURI UNIVERSITY OF SCIENCE AND TECHNOLOGY

In Partial Fulfillment of the Requirements for the Degree

DOCTOR OF PHILOSOPHY

in

ELECTRICAL ENGINEERING

2018

Approved by

Yahong Rosa Zheng, Advisor
Randy H. Moss
Mohammad Tayeb Ghasr
Kristen M. Donnell
Xiaoming He

PUBLICATION DISSERTATION OPTION

This dissertation consists of the following three articles which have been submitted for publication, or will be submitted for publication as follows:

Paper I, (Pages 7-35) Yang, X.; Manzoor, Z.; Zheng, Y. R.; Ghasr, M. T.; and Donnell, K. M.; "A Low Complexity Image Reconstruction Method for Synthetic Aperture Radar Imaging Systems with Very Sparse Arrays", is submitted to *IEEE Transactions on Instrumentation and Measurement*, August, 2018.

Paper II, (Pages 36-67) Yang, X.; Zheng, Y. R.; Ghasr, M. T.; and Donnell, K. M.; "Microwave Imaging From Sparse Measurements for Near-Field Synthetic Aperture Radar", has been published by *IEEE Transactions on Instrumentation and Measurement*, July, 2017.

Paper III, (Pages 68-81) Yang, X.; and Zheng, Y. R.; "An Image Denoising Method for SAR Images with Low-sampling Measurements", has been published by *SPIE conference on Smart Structures + Nondestructive Evaluation*, Denver, CO, USA, March, 3-7, 2018.

ABSTRACT

This dissertation investigates image reconstruction algorithms for near-field, two-dimensional (2D) synthetic aperture radar (SAR) using compressed sensing (CS) based methods. In conventional SAR imaging systems, acquiring higher-quality images requires longer measuring time and/or more elements in an antenna array. Millimeter wave imaging systems using evenly-spaced antenna arrays also have spatial resolution constraints due to the large size of the antennas. This dissertation applies the CS principle to a bistatic antenna array that consists of separate transmitter and receiver subarrays very sparsely and non-uniformly distributed on a 2D plane. One pair of transmitter and receiver elements is turned on at a time, and different pairs are turned on in series to achieve synthetic aperture and controlled random measurements. This dissertation contributes to CS-hardware co-design by proposing several signal-processing methods, including monostatic approximation, re-gridding, adaptive interpolation, CS-based reconstruction, and image denoising. The proposed algorithms enable the successful implementation of CS-SAR hardware cameras, improve the resolution and image quality, and reduce hardware cost and experiment time. This dissertation also describes and analyzes the results for each independent method. The algorithms proposed in this dissertation break the limitations of hardware configuration. By using 16×16 transmit and receive elements with an average space of 16 mm, the sparse-array camera achieves the image resolution of 2 mm. This is equivalent to six percent of the $\lambda/4$ evenly-spaced array. The reconstructed images achieve similar quality as the fully-sampled array with the structure similarity (SSIM) larger than 0.8 and peak signal-to-noise ratio (PSNR) greater than 25.

ACKNOWLEDGMENTS

Firstly, I would like to express my sincere gratitude to my advisor, Professor Yahong Rosa Zheng, for her continuous support of my Ph.D. study and related research, and for her patience, motivation, and immense knowledge. Her guidance helped me during the research and writing of this dissertation. I did my MS under her supervision and chose to continue with the Ph.D. program with her because I could not have imagined having a better advisor and mentor for my Ph.D. study.

I would also like to thank those who provided the funding support for my research: the graduate assistantship by intelligent systems center of Missouri S& T, the Army Small Business Technology Transfer Program project, and the WilkenâĂŹs Missouri telecommunication endowment fund.

I wish to thank Drs. M. Tayeb Ghasr and Kristen M. Donnell of the Applied Microwave Nondestructive Testing Laboratory for their help with the SAR experiments and writing of technical papers. Their support and guidance during the past three years helped my research in SAR image reconstruction. My close collaboration with them, as well as the students in the AMNTL, has been very fruitful

I would like to thank the other members of my advisory committee, Drs. Randy Moss and Xiaoming He, not only for their insightful comments and encouragement but also for their hard questions that forced me to widen my research from various perspectives.

I would like to thank my fellow labmates: Yiheng Wang, Mohammadhossein Behgam, Huai Huang, Niaz Ahmed, Dongjie Bi, and other visiting scholars for the stimulating discussions, for the sleepless nights we worked together before deadlines.

Last but not least, I would like to thank my family, my father Dr. Zhiheng Yang, and my mother Ms. Fei Li, for their emotional support during the course of this dissertation and for their trust, love, and care throughout my life.

TABLE OF CONTENTS

Page

LIST OF ILLUSTRATIONS

SECTION

1. INTRODUCTION

1.1. BACKGROUND

Imaging at millimeter wavelengths has typically been accomplished by scanning a single sensitive beam systematically across the scene to be imaged. Though this process is traditionally very slow, the quality of the recovered images is high. The latest millimeter-wave imaging systems include two fundamentally different techniques [1, 2]. The first technique applies a focal-plane two-dimensional (2D) array of millimeter-wave detectors placed behind a large lens and can achieve real-time operation, which is its most obvious feature. Additionally, the operation for imagers of this technique is analogous to the operation of an optical camera. However, its disadvantages include (1) relatively low resolution, (2) small aperture, (3) limited field of view, and (4) high cost for the 2D array. The second technique, known as synthetic aperture radar (SAR), uses a holographic linear array of sequentially switched transmitter receivers scanned quickly over a large aperture to actively illuminate the target. Then, the imagers of this technique record the phase and amplitude of the returned signal. The data can be mathematically reconstructed into a focused image of the target without the need for a lens. Advantages of this technique include (1) near real-time operation, (2) high resolution, and (3) three-dimensional (3D) reconstruction. The primary disadvantage of this technique is that the depth of focus is very short.

The SAR imaging method has been widely used in biomedical, security, geophysics, and remote sensing applications. Several high-resolution SAR imaging systems have been developed [3, 4, 5]. Accurate and highly-sensitive imaging probe platforms have been

demonstrated to detect and quantify small flaws within samples under tests (SUTs) [6]. However, based on the traditional sampling theory, high spatial resolution requires a small sampling size, so the spatial sampling rate is greater than the Nyquist sampling rate to avoid aliasing and preserve the quality of image reconstruction [5]. The traditional sampling rate is higher than the Nyquist sampling rate, resulting in many measurements that lead to long acquisition time for reasonably-sized SUTs. As a result, there is a great interest in reducing the number of measured spatial points. This dissertation focuses on the wide-band holographic SAR imaging system for nondestructive evaluation (NDE), which has widespread utility. The image reconstruction method is based on the SAR and compressed sensing (CS) algorithms.

This dissertation develops an innovative millimeter-wave imaging system capable of producing rapid images using a sparse sampling approach. The imaging system consists of 2D transmitter (Tx) and receiver (Rx) antenna arrays with non-uniformly-spaced elements. The RF front-end circuits randomly and electronically activate some pairs of the (2D) Tx-Rx elements sequentially, thereby enabling use of non-uniform and sparse sampling SAR imaging and of the CS technique for image reconstruction.

The CS technique is a signal-processing technique for efficiently reconstructing an image from far fewer samples than required by the Shannon-Nyquist sampling theorem. The proposed millimeter-wave imaging system uses significantly fewer antennas compared to the conventional imaging system for the same area SUTs. This dissertation proposes several CS-based image reconstruction methods and post-processing techniques to maintain the quality of the recovered images while significantly reducing the scanning time for both imaging systems [7]. The CS-based method can effectively improve the quality of reconstruction with under-sampled data. It has been proven that it is possible to perfectly reconstruct images with proper constraints [8]. The constraints can be summarized as randomness (incoherence) and sparsity. In the SAR imaging system, the reconstruction is sparse when

the background area is much larger than the target area. The raw data from the imaging systems are measured randomly in monostatic configurations or measured randomly in bistatic configurations. The details for the CS-based algorithm are shown in Appendix A.

In this dissertation, the main purpose for the CS-based reconstruction technology is to improve the reconstruction. However, few papers directly use image quality as a constraint on CS. Most papers only use total variation, which maximizes the absolute gradient for the images instead of the image quality. In this dissertation, a new constraint based on a non-reference image quality metric has been added to the CS optimization problem to replace the common total variation constraint [9]. This constraint is used to maximize the ïňĄnal reconstruction quality, and the total variation is contained in this quality constraint. The details for the gradient of the non-reference quality metric are derived in Appendix B.

1.2. PROBLEM STATEMENT

This dissertation proposes a bistatic configuration, random antenna, and millimeter and microwave SAR imaging system to sufficiently exert its effect on CS technology. Our research group has configured and tested a prototype for the proposed imaging system. Figure 1.1 depicts the hardware of the bistatic SAR imaging system. The prototype is configured with eight receiver subarrays, eight transmitter subarrays, and other auxiliary equipment. Figure 1.1a shows the photos of transmitter and receiver subarray, and Figure 1.1b shows the photo of the whole imaging system.

The proposed imaging system can be separated into hardware and software. The hardware collects the SAR signal of the SUTs, while the software reconstructs images from collected signals. Both the hardware and software can be divided into three sub-parts. The hardware includes (1) a multi-frequency microwave signal generator, (2) microwave electrical switches, and (3) transmitters and receivers. The software includes (1) signal preprocessing software, (2) a CS-based reconstruction operator, and (3) image denoising and other post-processing software. The signal generator produces wideband signals on the

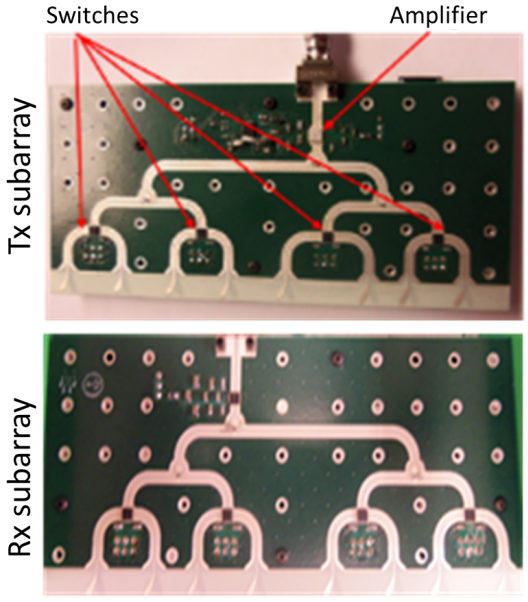

(a) The photos for the transmitter and receiver subarray.

(b) The photo for the prototype imaging system.

Figure 1.1. Photos for the random array imaging system.

Ka-band frequency (26.5 GHz to 40 GHz). High-frequency signals have strong penetration and larger minimal resolution size, while wideband signals improve the reconstruction quality by carrying more information. The electrical switches replace the time-consuming mechanical arm or other complex equipment in the antenna time-division multiple access (TDMA) working method. Each switch connects to one antenna to ensure that each time only one Tx-Rx pair transfers the signals. The transmitter and receivers are separated in the proposed imaging system and take advantage of the fact that the net radar resolution depends on the product of the two gain patterns. The system will thus ensure that the final reconstructions will have a high-resolution size, with low-resolution Tx and Rx subarrays. The signal preprocessing software sorts the raw bistatic data to the under-sampled, uniform, and equally-spaced data. It is also possible to directly apply the raw data via the CS procedures. However, the computational cost in that case is too high to be acceptable. The

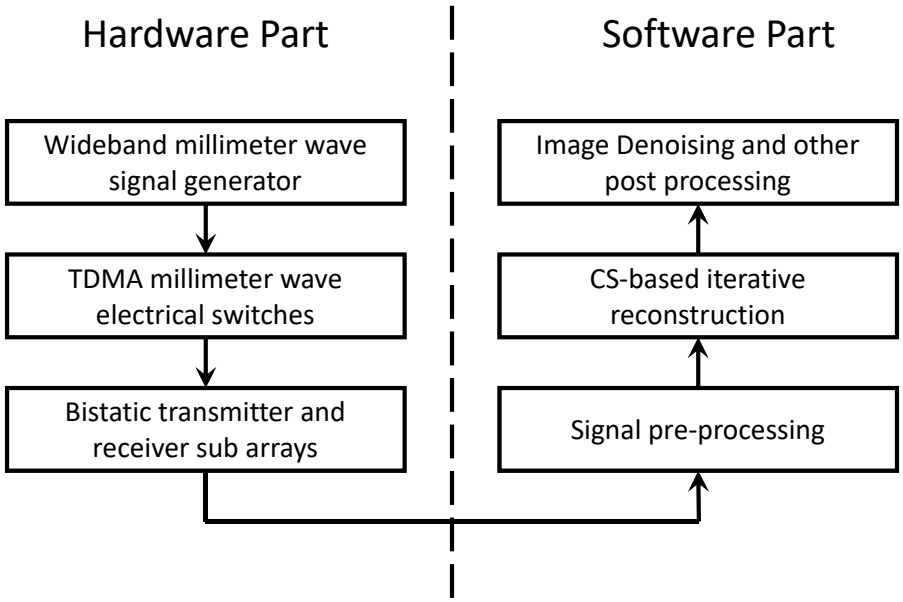

Figure 1.2. The block diagram of image reconstruction for the proposed real-time millimeter wave compressive sensing imaging system.

CS-based reconstruction operator could highly improve the quality of the reconstructions. In the proposed imaging system, there are only 241 samples in each frequency slice, while the resolution size for the final reconstruction could be as high as 200×200. The sampling rate is much lower than the requirement for the Nyquist sampling rate, and the reconstruction should be filled with aliasing with the normal reconstruction method. The final step of image denoising and other post-processing is designed based on the features of the SAR image to further improve the reconstruction quality. The block diagram for the whole proposed imaging system is illustrated in Figure 1.2.

1.3. SUMMARY OF CONTRIBUTIONS

This dissertation proposed several different methods for improving the quality of SAR reconstructions. Several journal publications and conference papers are listed in the publication list that give detailed introductions to these methods. The first journal paper

introduces and analyzes the performance of the system combining all the methods, and other papers introduce and analyze each method separately. My contributions, both published or under review, are as follows:

1. This dissertation proposes a low-complexity image reconstruction method for the sparse array SAR imaging system to reconstruct high-resolution images via adaptive re-gridding and compressed sensing. Experiments using millimeter-wave frequencies in the Ka-band (26.5 - 40 GHz) have been conducted on several samples, and the proposed image reconstruction method has been applied to the sparse measurements. Objective measures (e.g., structure similarity (SSIM) and peak signal to noise (PSNR)) and subjective measures (e.g., details of the object boundary, smoothness of shape, and artifact elimination) indicate the excellent qualities of the reconstructed 2D SAR images.

2. This dissertation proposed a compressed sensing-based image reconstruction method. With this method, only 35% of measurements currently needed by the traditional method are necessary for reconstruction. This dissertation also proposed a feature detection method for the reconstruction. With the reconstruction and detection methods, only 10% of measurements needed by the traditional method are necessary for detection. When compared to the traditional SAR image reconstruction method, experimental and simulation results illustrate this method's accuracy, and the computational cost for this method is acceptable.

3. This dissertation also proposed an image denoising method for the SAR images based on the level set method (LSM) to improve reconstruction in the future. Simulation and experimental results illustrated that only a 20% measurement is necessary for the SAR experiment to identify the objects of interest using the proposed method.

PAPER

I. A LOW COMPLEXITY IMAGE RECONSTRUCTION METHOD FOR SYNTHETIC APERTURE RADAR IMAGING SYSTEMS WITH VERY SPARSE ARRAYS

Xiahan Yang, Yahong Rosa, Zheng, Mohammad Tayeb Ghasr, Kristen M. Donnell

Department of Electrical & Computer Engineering

Missouri University of Science and Technology

Rolla, Missouri 65409–0040

Tel: 573–341–6622, Fax: 573–341–4115

Email: {xy6v4, zhengyr, mtg7w6, kmdgfd}@mst.edu

ABSTRACT

A near-field millimeter wave synthetic aperture radar (SAR) imaging system has been built with very sparse arrays in a bistatic configuration consisting of 128 transmit antennas and 128 receive antennas. This paper proposes a low-complexity image reconstruction method for the sparse array SAR imaging system to reconstruct high resolution images via adaptive re-gridding and compressed sensing. Experiments using millimeter wave frequencies in the Ka-band (26.5 - 40 GHz) have been conducted on several samples and the proposed image reconstruction method is applied to the sparse measurements. The reconstructed 2D SAR images demonstrate excellent qualities in terms of objective measures such as SSIM and subjective measures such as details of object boundary, smoothness of shape, and elimination of artifacts.

Keywords: Synthetic Aperture Radar, random array, bistatic imaging configuration, low-sampling reconstruction, compressed sensing.

1. INTRODUCTION

Microwave and millimeter wave imaging methods based on synthetic aperture radar (SAR) algorithms are efficient in producing two-dimensional (2D) and three-dimensional (3D) holographic images of dielectric structure. These imaging methods have shown tremendous potential for nondestructive evaluation (NDE) with widespread utility. The SAR imaging method has been widely used in biomedical, security, geophysical, and remote-sensing applications [1, 2]. More specifically, our group has applied valuable SAR image methods to inspecting the ever-increasing composite structures replacing metals in plenty of industries [3, 4, 5, 6, 7]. Previous works are based on the monostatic (i.e., transmitting and receiving antennas are collocated) SAR imaging model [3], which is efficient and fast at producing high-quality measurements and reconstructions. However, measuring instruments for monostatic imaging configurations may suffer from limited dynamic range due to difficulties isolating the receiver hardware from the transmitter signals [8], especially when the imaging system model is nearfield with the very large frequency bandwidth required for 3D imaging. The limited isolation leads to signals coupling directly from the transmitter to the receiver due to the limited directivity of aperture reflections in the antenna. These signals saturate the receiver, subsequently reducing the overall dynamic range and thereby limiting the measurement system [8].

Interest in using bistatic configurations to replace the normal monostatic configurations in SAR systems has increased [9, 10, 11]. In a bistatic configuration, the antenna is separated to the transmitter sub-antenna and the receiver sub-antenna. This configuration provides a relatively large dynamic range due to the high isolation between the receiver and the transmitter circuitry, in which one pair of the nearby transmitter and receiver is used as a measuring pair for all specimens under test (SUTs). Switches control each measuring pair transmits and receives signals after the last pair finished. The bistatic configuration can improve isolation as the transmitter and receiver sub-antennas are located separately. Moreover, two sub-antennas make it possible to distinguish targets from clutter [12].

In the new bistatic configuration SAR imaging system, the conventional SAR imaging reconstruction algorithms designed for the monostatic configuration model are applicable. The most serious problem with existing SAR reconstruction algorithms is that they cannot properly estimate the image for a bistatic configuration, which leads to image distortion caused by the algorithms' dependency on the transmitter-receiver geometry [13]. This problem does not exist in monostatic configurations. We approximated the bistatic configuration as a monostatic configuration to reduce image distortion by using an estimated equivalent transceiver to replace the nearest transmitter and receiver pair. In [8], we have shown the hardware processing and proven the possibility of the approximation. The fast and efficient fast-Fourier transform (FFT) based monostatic imaging algorithms are effective in generating 2D or 3Dimages from bistatic measurements [14]. We applied the ω âĹŠ K algorithm on the near-field SAR system where the approximation creates image distortion since the bistatic range will be much larger than the monostatic range [15]. The errors in the approximation will be acceptable.

We proposed a re-gridding method for the monostatic approximation measurements to grid it from a non-uniform grid to a uniform grid to profoundly reduce the computational cost. The proposed re-gridding method is based on the principle of minimizing the truncation error in interpolation with adaptive and adjustable resolution size. The positions of the equivalent transceiver are in a non-uniform grid. The computational cost is too high when directly reconstructing the data from the non-uniform grid. Thus, interpolation is necessary to transfer the data from the non-uniform grid to the uniform grid. The equivalent transceiver can only sample a few points on the interpolated grid, which has high-resolution size. Since no sampling information exists for other points on the high-resolution size grid, we created a uniform grid with the proper offset and resolution size to minimize the truncation error based on the proposed algorithm. We used 'valid points' to present the nearest points on the uniform grid for the equivalent transceiver position. We interpolated the data to the uniform grid after monostatic approximation and kept the data on the valid points to create a virtual

under-sampled data for the compressed sensing (CS) reconstruction method. In this case, the virtual under-sampled data is the uniform data with minimal error compared to the raw data from the SAR imaging system. A 2D Gaussian low-pass filter is applied to convolute interpolated data when the virtual under sampling rate is too low in CS reconstruction. The measurement from the SAR imaging system with the re-gridding method can only be reconstructed in high quality with a CS-based model, as the measurement is in a very low under-sampling rate.

We used a CS-based method to reconstruct the interpolated uniform data. The CS-based method can effectively improve the quality of reconstruction with under-sampled data [16]. It has been proven that it is possible to perfectly reconstruct images with proper constraints [6, 7, 16, 17, 18, 19, 20]. The constraints can be summarized as randomness (incoherence) and sparsity. In the SAR imaging system, the reconstruction is sparse when the background area is much larger than the target area. With the bistatic configuration, monostatic approximation, and re-gridding method to transfer the raw data to a uniform grid, the virtual under-sampled data can be measured randomly and fits the request for the CS-based reconstruction method.

2. SYNTHETIC APERTURE RADAR IMAGING SYSTEM WITH VERY SPARSE ARRAY

In this section, we will give the detailed introduction for the near-field millimeter wave SAR imaging system. This imaging system is designed for the 'random' principle in CS theory to break the limitation of antenna hardware size to measure more details and reconstruct higher resolution image.

2.1. Random Array. Randomness is a significant and essential condition for CS. In the original CS papers [17, 21], the sampling mask was chosen completely at random in mathematical proofs to guarantee a very high degree of incoherence. However, random point sampling for all dimensions is a mostly impractical condition, especially in radar

imaging, as the antenna array in most cases is fixed and hard to change in position. We used a movable antenna array with programmable trajectory from our previous paper [5]. The system can manually choose the sampling grid to satisfy randomness. We have shown that this imaging system could highly reduce the size of the raw measurement while keeping the reconstruction quality with a much smaller antenna array and a CS-based approach. Considering the velocity and flexibility of the hardware, this scanning method is hard to achieve in most cases. Instead, we aim to design a practical incoherent sampling scheme. Building a large entirely random array imaging system is difficult. Therefore, we used an alternative method that configures several sub random arrays, and the hardware limits the randomness of the antenna array. In an ideal random array, each element position should be independent of the others. We first built a 1-D random antenna sub imaging system, and each sub imaging system contains a transmitter PCB board and a receiver PCB board on which is eight antennas respectively. The sub imaging system is fixed on a moving mechanical arm to do the raster scan, which we called it as the 1D random experiment. The entire proposed SAR imaging system configures several sub imaging systems together with different offsets, as shown in Figure 1a. An electrical switch replaced the conventional mechanical arm to save measuring time. The antenna's array for the imaging system model is shown in Figure 1b. The experiments with the proposed imaging system is called 2D random experiment. We will introduce more details for the antenna array.

The random array is separated as the receiver subarray and transmitter subarray in the bistatic configuration SAR imaging model. The random array design has two essential conditions: 1. Distance between the adjacent elements should be larger than the real size of a transmitter or receiver to ensure the combination in hardware board. 2. Distance between two transmitter's (or receiver's) antennas should try to guarantee existing at least one receiver (or transmitter) antenna. These conditions can avoid signals from few transmitters not being received by any receivers and wasting resources.

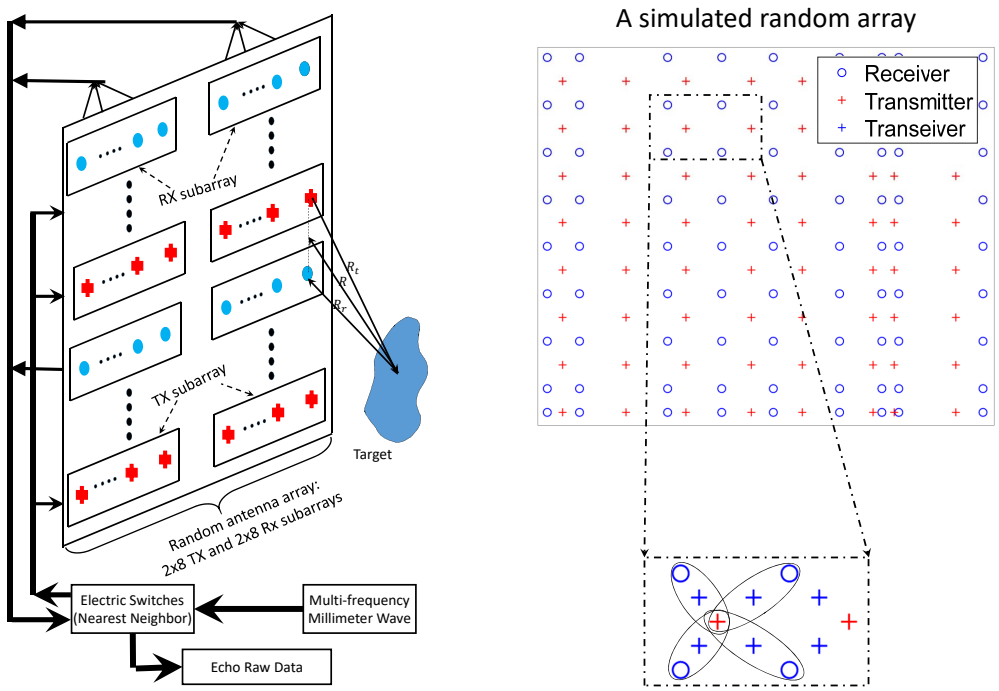

(a) Model for the proposed SAR imaging system

(b) A simulated random array using on the imaging system

Figure 1. Model for the proposed SAR imaging system and its antenna array.

2.2. Features of the Imaging System. The imaging system is a bistatic configuration; as shown in the model, the transmitter and receiver are separated. We also used the electric switches connected to the antenna array to replace the traditional mechanical arm to highly reduce scanning time. However, because the antenna array is fixed, the configuration for the antenna array will highly influence performance for the final reconstructions. The traditional, uniform, equally-spaced antenna array proved to be a hardcover for the whole interested area, and its reconstructions will be in very low-resolution size. Moreover, a compressed sensing method will have few improvements with the uniform equally-spaced data. In the imaging system, the antennas on one antenna board are configured non-uniformly, and several boards configure the final imaging system with non-equal offset as shown in Figure 1. The distance between the interested target and the imaging system is between 0 to 120 millimeters, which can be considered near-field. The imaging system uses the

Ka-band frequency signals in measuring. The top-left board is used as the first board to determine the position for the antennas. The direction from the antenna plane to the target is the z-axis, and with the x- and y-axis and the original point defined in Figure 1a, we can define a coordinate system to describe the position for all antennas and targets. When the adaptive grid is calculated, the position and offset of the grid are also based on this coordinate system.

3. THE PROPOSED IMAGE RECONSTRUCTION METHOD

In this section, we will give the detailed introduction for all the methods used in the SAR imaging system from measuring to reconstructing. Figure 2 illustrates the flow of image reconstruction for the imaging system. The procedures can be simply divided in to monostatic approximation, interpolation, and reconstructions.

3.1. Measuring: Monostatic Approximation in Near Field Bistatic SAR Imaging. There are numerous algorithms for SAR image reconstruction, such as time-domain back projection (TBP) [13], polar formation algorithm [22], range migration algorithm [9]. All of these algorithms are fundamentally implemented for monostatic configuration, and are also available on bistatic configuration. Balancing the computational cost and accuracy, we choose the $\omega - K$ SAR algorithm which is a fast and efficient algorithm in this study. Eq. (1) illustrates the measurement collection from the random array antenna.

$$\tilde{\mathbf{S}} = \sum_{f} \sum_{v_t} \sum_{u_t} \sum_{v_r} \sum_{u_r} \mathbf{G} e^{jK_z R_t} e^{jK_z R_r} \tag{1}$$

where $\tilde{\mathbf{S}}$ is the reconstructed image, f represents frequencies of the millimeter wave signal, v_t and u_t represent the locations of the transmitter and v_r and u_r represent the locations of the receiver locations, j is the imaginary units, $\mathbf{G}$ is the raw measurement, K_z =

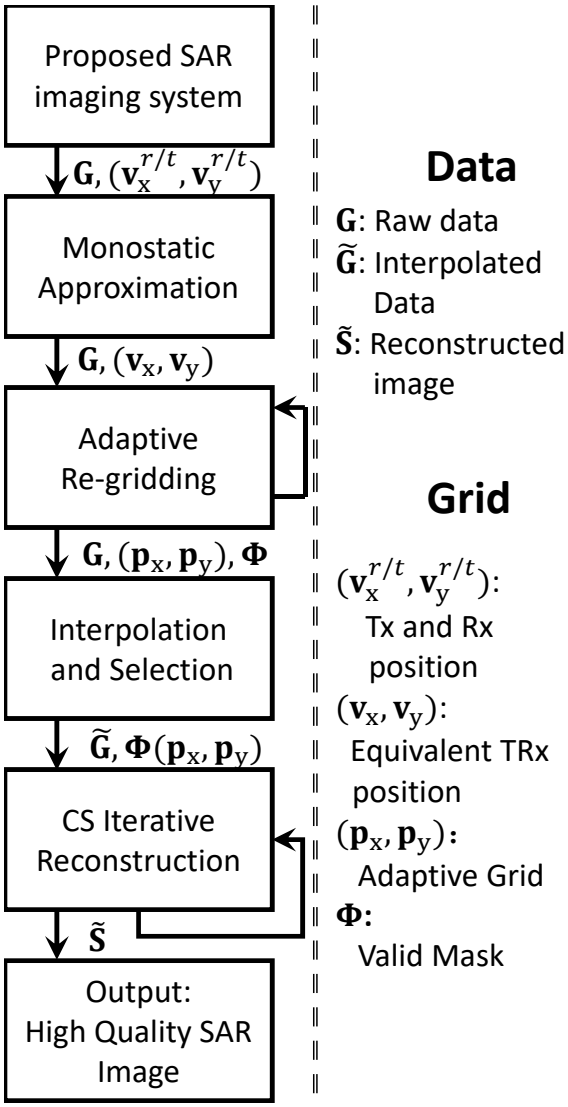

Figure 2. The block diagram for proposed SAR imaging system image reconstruction and the symbols used in this dissertation.

$\sqrt{4K^2 - K_x^2 - K_y^2}$ is the frequency component on the z direction, while K_x and K_y is the frequency component on the x and y direction respectively, and R_r/R_t is the distance between the transmitter/receiver element and the target point.

However, it is apparent that the computational cost of this method is huge. In [8], we proposed an approximation method for bistatic configuration to monostatic configuration (i.e., a quasi-monostatic configuration). In this configuration, we used an equivalent

transceiver to replace the transmitter and receiver, as shown in Figure 3. To simplify, we only show the 1-D model in Figure 3. And the transformation between the measurement and image is shown in Eq. 2, which is derived in [7].

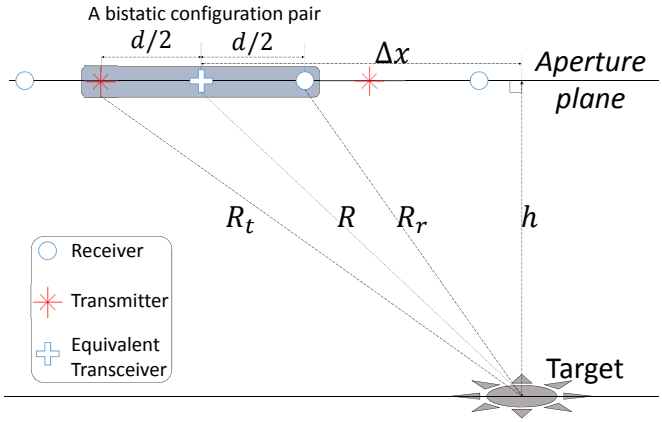

Figure 3. Schematic of a 1-D bistatic scan for imaging a target and the defined baseline range.

$$\begin{aligned}\mathbf{S} &= \sum_{f}\sum_{v_x}\sum_{v_y}\mathbf{G}e^{j2KzR} \\ &= \mathfrak{F}_{NU}\{\mathfrak{F}_{2D}\{\mathbf{G}e^{j2K_zR}\}\}\end{aligned} \tag{2}$$

where (v_x, v_y) is the position of each equivalent transceiver. $R = \sqrt{(x-v_x)^2 + (y-v_x)^2 + h^2}$ is the distance between the target and equivalent transceiver, and $\mathfrak{F}_{2D}$, $\mathfrak{F}_{NU}$ are the 2-D Fast Fourier Transform (FFT) and non-uniform FFT operator.

3.2. Interpolating: Re-gridding and Valid Mask.

3.2.1. Re-gridding method. Interpolation is a common choice for the non-equally-spaced measurement. Compared with other methods such as NUFFT, NFFT, interpolation is faster and easier to achieve. The main disadvantage of interpolation is its accuracy. Iterations in interpolation accumulated truncation errors which will influence the final reconstruction, especially in the iterations in CS-based methods, as we have shown in our previous paper [7]. There are several error minimization methods designed for reducing

the truncation error [23, 24]. For the random array antenna distribution, we propose an adaptive re-gridding method which is based on the minimum error condition. The method is of a low computational cost and can reach very low truncation error.

The re-gridding method can be illustrated as the following optimization problem:

$$\begin{aligned} &\text{minimize} \quad E_d = ||\Upsilon(\mathbf{p}_x, \mathbf{p}_y) - (\mathbf{v}_x, \mathbf{v}_y)||_2^2 \\ &\text{subject to} \quad \mathbf{p}_x, \mathbf{p}_y \text{are equally spaced} \end{aligned} \tag{3}$$

Here, E_d defines the distance error between the raw and interpolated grids. Υ is the valid mask which is the set for the valid point, $(\mathbf{p}_x, \mathbf{p}_y)$ are the positions of the points on an uniform grid, $(\mathbf{v}_x, \mathbf{v}_y)$ are the positions of the equivalent transceiver array.

A uniform grid is fixed if and only if the three following variables are fixed: 1) The x-axis and y-axis direction, 2) the original point position on the space, and 3) the step sizes on x-axis and y-axis. In the proposed imaging system, the interpolated grid is on the same plane for the interested target and the x-axis direction is same as the antenna array direction. We are focusing how to optimized the original point (f_x, f_y) and the step size (d_x, d_y) on the adaptive interpolated grid, and $(\mathbf{p}_x, \mathbf{p}_y) = (f_x + \mathbf{q}_x \cdot d_x, f_y + \mathbf{q}_y \cdot d_y),\ q_x = 0, 1, \ldots M_x - 1, q_y = 0, 1, ..M_y - 1$, M_x, M_y is the number of elements on x and y-axis.

With the principles for the interpolation grid, Eq. 3 can be rewritten in the form with original point, validation points, and the step sizes, as shown in (4):

$$\begin{aligned} \text{minimize} \quad \sum_{q=1}^{N_{tr}} \big(&(f_x + k_x^q d_x - v_x)^2 + \\ &(f_y + k_y^q d_y - v_y)^2 \big) \end{aligned} \tag{4}$$

where (k_x^q, k_y^q) is the index of the non-zero element in the valid mask related to the q^{th} elements in the equivalent transceiver array.

We propose an iteration called adaptive re-gridding method illustrated in Alg. 1 to solve Eq.(4). Figure 4a shows the block diagram for the proposed re-gridding method, and Figure 4b illustrates the steps of the optimization for the proposed re-gridding method.

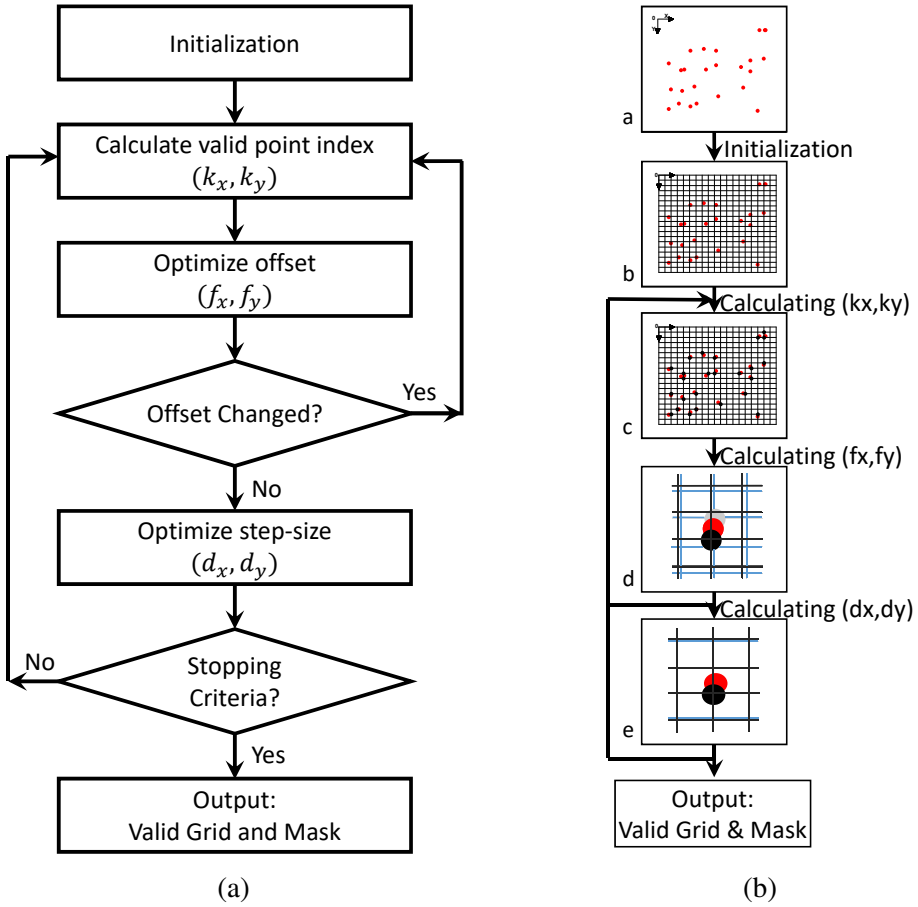

Figure 4. (a) The block diagram for the proposed adaptive re-gridding method. (b) Steps for the uniform grid optimization based on the proposed re-gridding method.

In Figure 4b, the red points are the positions for the raw data, the gray points are positions of the intermediated valid mask, and the black points are the position of the final valid mask point. The black line presents the optimized grid at one step in the iteration, and the gray line presents the grid at the previous step in the iteration. Figure 4b illustrates that the valid points may change during optimizing the (f_x, f_y) and (d_x, d_y). In the proposed algorithm, Each change in (k_x, k_y) will recalculate other parameters.

Algorithm 1 adaptive re-gridding method

Input:
  $(\mathbf{v}_x, \mathbf{v}_y)$ - raw data position.
  $MaxN$ - Max iteration number.
  Dr - Distance Ratio.
Output:
  (f_x, f_y) - original point
  (d_x, d_y) - step size on x-axis and y-axis
  $(\mathbf{k}_x, \mathbf{k}_y)$ - index vector for the non-zero element in the valid mask
  $\mathbf{\Phi}$ - valid mask
Initialization: $k = 0$; $Change = True$, $(f_x, f_y) = (0, 0)$; $(d_x, d_y) = (\sqrt{Dr} * E\{\mathbf{v}_x\}, \sqrt{Dr} * E\{\mathbf{v}_y\}$; $(n_x, n_y) = (\lfloor (max(\mathbf{v}_x) - min(\mathbf{v}_x)/d_x \rfloor, \lfloor (max(\mathbf{v}_y) - min(\mathbf{v}_y)/d_y \rfloor)$, $\mathbf{\Psi} = \mathbf{0} \in R^{M_x \times M_y}$, $\mathbf{p}$ is the grid defined by (f_x, f_y) and (d_x, d_y).
while E_d >threshold or $k < MaxN$) **do**
    while Change == True **do**
        $(\mathbf{k}_x, \mathbf{k}_y, \mathbf{\Phi}) = f_{em}(f_x, f_y, d_x, d_y, n_x, n_y, \mathbf{v}_x, \mathbf{v}_y)$.
        $f'_x = E\{\mathbf{v}_x - \mathbf{k}_x d_x\}$; $f'_y = E\{\mathbf{v}_y - \mathbf{k}_y d_y\}$
        if $f'_x == f_x$, and $f'_y == f_y$ **then**
            Change = False.
        else
            $f_x = f'_x$, $f_y = f'_y$
        end if
    end while
    $d'_x = \mathbf{k}_x^T (f'_x - \mathbf{v}_x)/(\mathbf{k}_x^T \mathbf{k}_x)$; $d'_y = \mathbf{k}_y^T (f'_y - \mathbf{v}_y)/(\mathbf{k}_y^T \mathbf{k}_y)$
    k = k+1
end while
return (f_x, f_y), (d_x, d_y), $(\mathbf{k}_x, \mathbf{k}_y)$, $\mathbf{\Phi}$.

The gridding method requires the enumeration method of f_{em} illustrates in Alg. 2. Figure 5 illustrated the block diagram for the enumeration method.

There are three steps for the proposed re-gridding method, respectively for calculating $(\mathbf{k}_x, \mathbf{k}_y)$, (f_x, f_y), and (d_x, d_y). It is easy to prove that the results for (f_x, f_y) and (d_x, d_y) will be global optimization. However, since $(\mathbf{k}_x, \mathbf{k}_y)$ are using an enumeration method and it is a discrete integer array, the error may be increased with the new $(\mathbf{k}_x, \mathbf{k}_y)$. In practice, we stored all the errors and variable state in each iteration and output the variables with the minimal error.

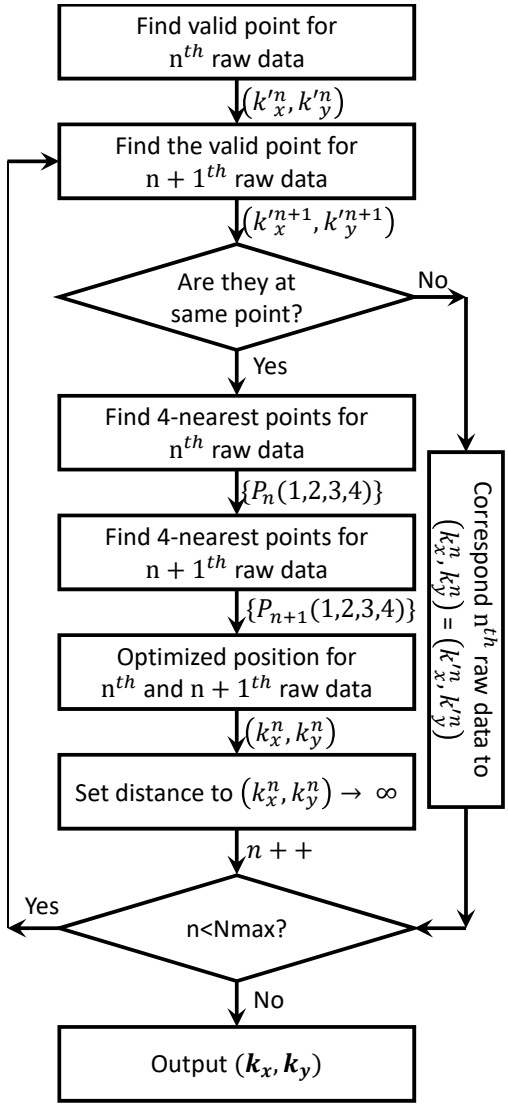

Figure 5. The block diagram for the enumeration method for calculating the valid mask (k_x, k_y).

We simulated several random arrays with different points and different distance ratio Dr. The simulated arrays are limited in an 100×100 square area. The maximum iteration number is 100 during our simulation. For each set of parameters, we repeat the simulation 100 times to reduce influence for randomness. Figure 6 illustrate the normalized average truncation error curve and the normalized minimal truncation error curve during each iteration:

Algorithm 2 Enumeration method for valid mask

Input:
  $(\mathbf{v}_x, \mathbf{v}_y)$ - raw data position
Output:
  $(\mathbf{k}_x, \mathbf{k}_y)$ - index vector for the non-zero element in the valid mask
  $\mathbf{\Phi}$ - valid mask
Initialization: $Mask = \mathbf{0} \in R^{n_x \times n_y}$, $\mathbf{k}_x = 0$; $\mathbf{k}_y = 0$. $q = 0$, $\mathbf{d} = \mathbf{0} \in R^{size(\boldsymbol{\zeta})}$
while $q \leqslant length(\mathbf{v}_x)$ **do**
    $\mathbf{d}$ = Distance matrix for the distance between the point $(v_x(i), v_y(i))$ and all point in the $\boldsymbol{\zeta}$.
    $\mathbf{d} = \mathbf{d} + \mathbf{\Phi} \cdot \max(\mathbf{d})$
    k_x^q, k_y^q = the position for the $\min(\mathbf{d}) \in \mathbf{d}$.
    $\mathbf{\Phi}(k_x^q, k_y^q) = 1$
    q = q+1
end while
return $(\mathbf{k}_x, \mathbf{k}_y)$, $\mathbf{\Phi}$.

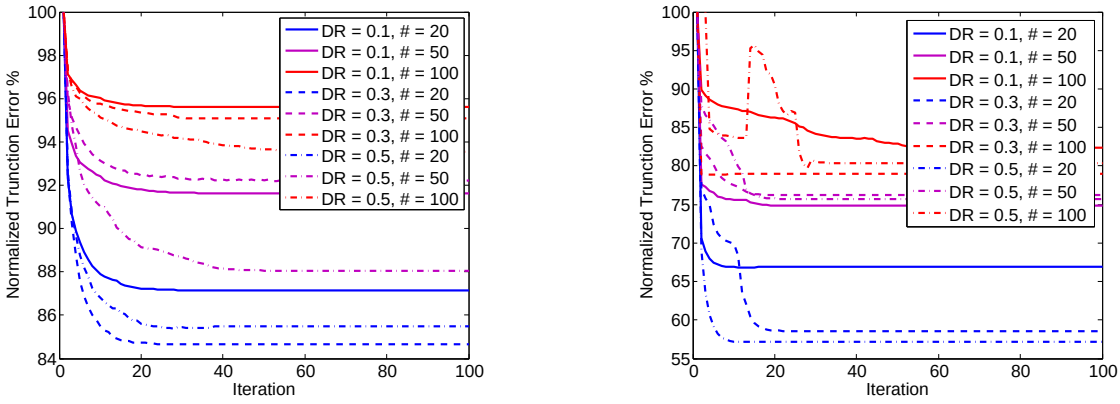

(a) (b)

Figure 6. (a) The normalized average truncation errors which are the average of the results for the adaptive interpolation method in the 100 simulation array. (b) The normalized minimal errors which are the best results for the adaptive interpolation method in the 100 simulation array.

From Figure 6, we can conclude that the adaptive interpolation method can averagely improve 10% performance for truncation error. Less random points and smaller distance ratio will in future improve the performance. In several individual cases, the adaptive interpolation method can reduce as much as 50% truncation errors.

Figure 7 shows the computational time for adaptive interpolated method during iteration with 100 iterations. We can observe that the computational cost for this method is very low and all computation could be finished in three seconds by a home PC with Intel(R) Core(TM) i7-4790 CPU @ 3.60GHz, 16.0 GB RAM.

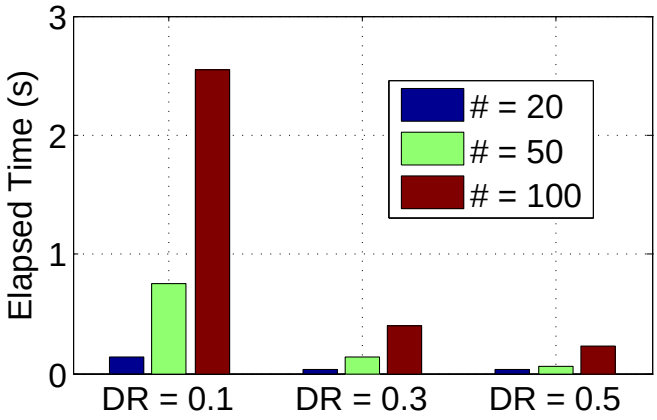

Figure 7. Computational cost for the adaptive interpolated method with the simulated random array.

3.2.2. Interpolation method. The Alg. 1 outputs a 0-and-1 matrix, which is the valid mask. We convolve a Gaussian bandpass filter on it to increase the usage of the raw data. The result of the convolution is considered as the sampling mask applied in the CS-based reconstruction.

There are plenty of interpolation methods for a 2-D grid [25]. We choose the 'cubic' interpolation method [26] in the proposed adaptive interpolation grid. Compared with the most popular 'linear' method [25], and the more accurate 'spline' method [27], the 'cubic' method preserves monotonicity of the data set being interpolated. The interpolated measurement with adaptive interpolated grid is represented as $\tilde{\mathbf{G}} \in \mathbb{R}^{M_{ij} \times N_{ij}}$. The sampling mask ζ_m represents the position of $\tilde{\mathbf{G}}$ with the set of highest accuracy used in this project. The size of ζ_m is as same as the raw measurement $\mathbf{G}$. Other positions are believed to have higher truncation errors and will be re-calculated with compressed sensing method.

3.3. Reconstructing: Compressed Sensing Based Image Reconstruction. This subsection introduces more details for the process of the nonlinear image reconstruction appropriate with CS-based method. CS-based method can help in increasing the resolution size and quality of the reconstruction when the measurements is under sampling [28]. In radar applications, the imaging system could build with less antenna and in future saving the hardware cost and measuring time. In CS-based method, suppose the interested image is $\tilde{\mathbf{S}} \in \mathbb{R}^{M \times N}$, the sparsifying transformation is denoted as $\mathbf{\Psi}$, and let $\mathbf{\Phi}$ denotes the SAR operator, corresponding to bistatic SAR method discussed earlier in (2), and $\mathbf{p}$ denotes the sampling mask calculated from Alg. 1. The reconstruction is obtained by solving the following constrained optimization problem:

$$\begin{aligned} &\text{minimize} \quad ||\mathbf{\Psi}\tilde{\mathbf{S}}||_1 \\ &\text{subject to} \quad ||\mathbf{p} \cdot \mathbf{\Phi}^{-1}\tilde{\mathbf{S}} - \tilde{\mathbf{G}}||_2 < \epsilon_{cs} \end{aligned} \tag{5}$$

where $\tilde{\mathbf{S}}$ is the reconstructed image, $\tilde{\mathbf{G}}$ is the interpolated measurements, and ϵ_{cs} controls the fidelity of the reconstruction to the measured data. It should be noticed that all the variables in (5) has been vectorizing.

There is another popular constraint that is usually added to the objective function in (5). Total-variation (TV) is a finite-differences operator. When a TV operator is added in (5), it can be considered a constraint that the reconstructed image is sparse both on the specific transform and finite-differences at the same time [28]. With TV constraint, the optimized formulation in (5) is rewritten to Eq. (6). In our case, we use the non-reference image quality operator introduced in Appendix B to replace the TV operator to observe better performance.

$$\begin{aligned} &\text{minimize} \quad ||\mathbf{\Psi}\tilde{\mathbf{S}}||_1 + \alpha_{TV} TV(\tilde{\mathbf{S}}) \\ &\text{subject to} \quad ||\mathbf{p} \cdot \mathbf{\Phi}^{-1}\tilde{\mathbf{S}} - \tilde{\mathbf{G}}||_2 < \epsilon_{cs} \end{aligned} \tag{6}$$

where α_{TV} trades $\mathbf{\Psi}$ sparsity with TV, and $(\cdot)$ represents the matrix scalar product.

In our previous work [4, 6, 16, 29], we show several efficient CS approaches suitable to SAR image reconstruction. In the random array application, we choose the non-linear conjugate gradient (CG-CS) method for its robustness and efficiency. Details of CG-CS are introduced in [7, 28].

3.4. Computational Complexity. Accurate or approximated estimation of elapsed time during the SAR imaging system measuring and recovering is a significant research topic. The operation time for the imaging system contains the measuring time, re-gridding time, CS reconstructing time, and the post-processing time. In the measuring part, overall, the bistatic configuration method is asynchronous and needs a longer time than the monostatic configuration system. During the measuring, only one pair of transmitter and receiver transform signals in each time, as we mentioned in section. 2. The measuring time for each pair is near 10 milliseconds (ms). For the whole imaging system, the measuring time is over 30 seconds (s). The post processing contains the normalization and histogram equalization. There are existing and efficient algorithms for both of them. The computational time for these two methods could be ignored (less than 100 ms).

The recovering part contains the re-gridding and CS reconstruction. As when the antenna is fixed, the adaptive interpolated grid will be fixed, and can be reloaded each time. The ‘cubic‘ interpolation time of complex measurements also could be ignored as the size of the measurement is small and only same number of interpolated measurement is necessary in interpolated grid. In the proposed imaging system, interpolating a measurement which contains 241×1 double data to a 250×250 uniform grid, where the density rate is near 0.25, is less than a half second for each frequency. The whole time of interpolation and re-gridding will less than 30 seconds. In 1D experiment, the interpolation time is similar with the 2D experiment and the re-gridding time is faster.

The vast majority of computing time is in CS reconstruction. The iterative reconstruction is more computationally intensive than linear reconstructed methods. The nonlinear conjugated gradient method with backtracking line-search [28] needs longer time

than other CS-based approaches. Figure 8 shows the computing time of CS-based with adaptive interpolated grid method of the reconstructions in the Results part by a home PC with Intel(R) Core(TM) i7-4790 CPU @ 3.60GHz, and 16.0 GB RAM. A parallel computing approach for each frequency can future reduce the computing time.

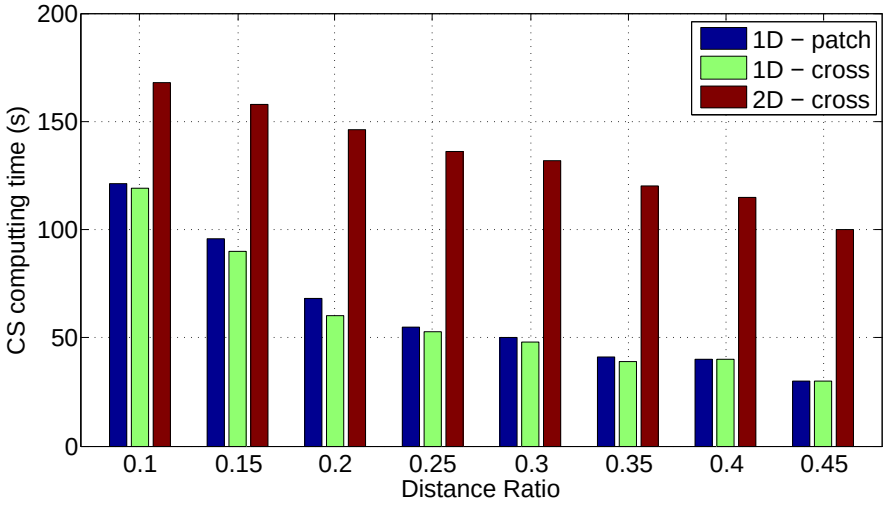

Figure 8. The measuring, interpolating, and reconstructing time for the imaging system in 1D and 2D experiments.

The computing time is inversely proportional to the resolution size or the distance ratio, while the computing time is independent of the size of the interested target. And the CS-based method obtains reconstructions within three minutes with proper frequency slices. Fewer frequency slices will reduce the reconstruction time.

4. EXPERIMENT AND SIMULATION RESULTS

In this section, we will show the reconstructions based on the proposed method and imaging system. First we will give a short introduction for normalization and two objective quality assessment metrics: Structure Similarity (SSIM) and Peak Signal to Noise (PSNR) to assess the quality for the reconstruction.

4.1. Several Pro-processes for the Reconstruction. The recovery $\tilde{\mathbf{S}} \in \mathbb{R}^{M\times N}$ from the CS-based method is a complex 2-D matrix. There are a few more steps to obtain clear and meaningful images.

1. Absolution. An observable image should be a real matrix instead of a complex matrix. The absolution of the CS recovery is computed firstly. $\tilde{\mathbf{S}}_1 = |\tilde{\mathbf{S}}|$.

2. Normalization. The range of pixel intensity value of I_1 should be into a range that is more familiar or normal to the senses and to avoid metal distraction or fatigue. In this project, images are normalized to uint8 ([0,255]). $\tilde{\mathbf{S}}_N = (\tilde{\mathbf{S}}_1 - Min(\tilde{\mathbf{S}}_1))\frac{255}{Max(\tilde{\mathbf{S}}_1)-Min(\tilde{\mathbf{S}}_1)}$.

3. Saving. Output the images for further test and study.

4.2. Reconstruction Quality Assessment. Reconstructing a 'good quality' image is always the target of an image reconstruction method. There are two major theories in image assessment: objective methods and subjective methods. It is easier to do a subjective analysis. For an objective quality assessment, A ground truth image is often useful. In this study, the totally ground truth image is hard to observe. We would like to use the reconstructions from (1) as the ground truth to judge other reconstructions. The SSIM and PSRN index of all reconstructions were calculated. Structural similarity (SSIM) and peak signal-to-noise ratio (PSNR) are commonly used for 2-D image quality evaluation. They are considered consistent with human eye perception. The specific form of the SSIM index between two images ($\mathbf{g}_1$ and $\mathbf{g}_0$) is defined as

$$\mathrm{SSIM}(\tilde{\mathbf{S}}_1, \tilde{\mathbf{S}}_0) = \frac{(2\mu_1\mu_0 + C_1)(2\sigma_{1,0} + C_2)}{(\mu_1^2 + \mu_0^2 + C_1)(\sigma_1^2 + \sigma_0^2 + C_2)} \tag{7}$$

where C_1 and C_2 are the auxiliary variables and (μ_1, μ_0), (σ_1^2, σ_0^2), and $\sigma_{1,0}$ are the mean, variance, and cross-covariance of two images, respectively. The typical parameter settings $C_1 = 10^{-4}$ and $C_2 = 9 \times 10^{-4}$ are used in this study. The SSIM value is in the range of

[0, 1], where the SSIM is 1 if the reconstructed image is exactly the same as the ground truth image. Thus, a large SSIM index corresponds to better reconstruction quality, and vice versa.

The specific form of the PSNR index between two images ($\tilde{\mathbf{S}}_1$ and $\tilde{\mathbf{S}}_2$) is defined as

$$\begin{aligned} \mathrm{PSNR} &= 10 \log_{10} \frac{255^2}{\mathrm{MSE}} \\ \mathrm{MSE} &= \frac{1}{N_{xy}} \sum_{n=1}^{N_{xy}} \left[\tilde{\mathbf{S}}_1(n) - \tilde{\mathbf{S}}_2(n)\right]^2 \end{aligned} \tag{8}$$

where $\tilde{\mathbf{S}}_i(n)$ is the n-th element of the image $\tilde{\mathbf{S}}_i, (i = 1, 2)$. Note that a large PSNR index corresponds to better reconstruction quality. We compare the quality between images reconstructed by normal interpolated and our adaptive interpolated grid with zero-filling (ZF) method and CS-based method with PSNR and SSIM as objective quality assessment metrics.

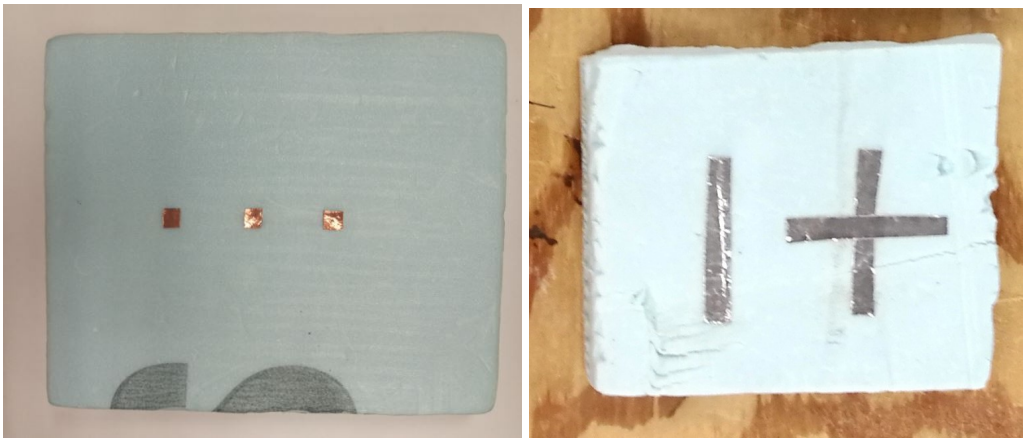

(a) The 'points' sample (b) The 'cross' sample

Figure 9. Photos for the SUTs in the experiment.

4.3. 1D Reconstruction. The size of the receiver subarray is 22×25 and the transmitter subarray is 21×24. We are moving one smaller circuit combined with transmitter and receiver subarray horizontally to simulate a hardware combination. The frequency range in Ka-band which is from $30 - 40$ GHz. It will be fixed on a mechanical arm moved

uniformally. So the grid of the measurements will have evenly-spaced size in one direction and non-uniform-step-size in the other direction. For results shown in this paper, all the experiments are set to be randomly distributed in the horizontal direction, and we named it as 1D experiment, the measurement as 1D measurements, and the reconstructions as 1D reconstructions. The software environment is a Intel(R) Core(TM) i7-4790 CPU @ 3.6GHz and 16.0 GB RAM in a Matlab2012b (The MathWorks, Matick, MA) implementation. There are two targets measured on 1D experiment: the first target contains three circular metal patches on a large wood board, and the second one contains a cross metal patch. Figure 9 shows the photos of the SUTs in our experiments. We named the samples as 'points' and 'cross'. The reflection ratio of the metal material is one while the background area is near zero. The distance between the antenna and SUTs is $Z_0 = 38mm$, where the antenna plane is located in $z_0 = 0$, and the direction is from SUTs to antenna. The size of the background area is $145mm \times 100mm$, and the diameter of the metal patches is over $10mm$. The metal patches have been positioned vertically and horizontally. The contrast ground is reconstructed with normal interpolation and CS-based method. Figure 10 shows the reconstructions from our method with different parameters and the contrast method with the three circular patches target. The 'cross' sample reconstructions in 1D experiment. From left to right: Reconstruction of zero-filling method with normal linear interpolation, CS-based method with normal linear interpolation, zero-filling method with adaptive interpolation method, CS-based method with adaptive interpolation method. From top to bottom, the distance ratio is 0.25, 0.20, 0.15, and 0.1.

Both zero-filling reconstructions, as expected, show a decrease in quality. These reconstructions are filled with obviously horizontal strip artifacts. In these reconstructions. The boundaries for the three material patches are hard to distinguished. The CS-based method with normal linear interpolation grid highly reduces artifacts. Boundaries of the three patches are separated to each other and each individual boundary is continuous. However, there are still apparent horizontal strip artifacts in the reconstruction. With the

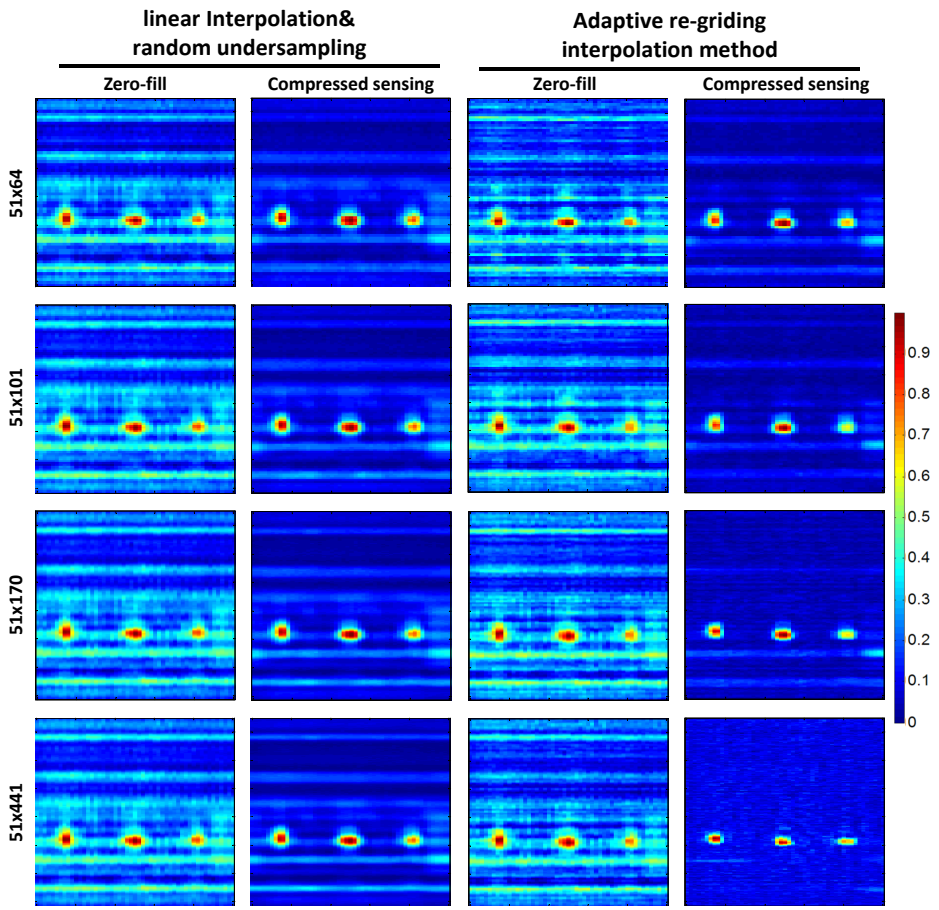

Figure 10. Experimental results. The 'points' sample reconstructions in 1D experiment.

resolution increasing, there is little improvement of the reconstructed quality. For the re-gridding with CS-based method, in a 51×441 grid, we get very high quality recovery with very clear and flat background where only one or two strips are visible. At other smaller resolution, we still get clearer reconstructions compared with other methods. There are few strip artifacts, while the contrast of the whole reconstruction is large enough to distinguish the interested targets when the resolution is larger than 51×101.

Figure 11 presents the objective evaluations for the reconstructions in Figure 10. The reconstruction from re-gridding with CS-based method in 51×441 resolution is used as the ground truth image. Other reconstructions are linearly resized to the same resolution. And all images have been normalized to uint8 format before assessment. The re-gridding with

CS-based method reconstruction has higher quality compared with the other methods. It is interesting to observed that the quality of the reconstructions from normal linear interpolated method with CS-based method is higher in larger resolution size, which is caused by the truncation error increased with higher resolution grid.

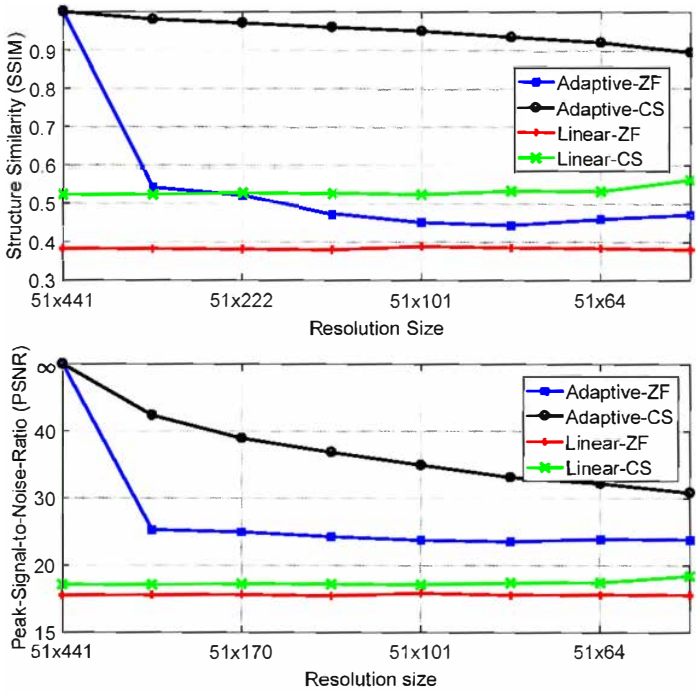

Figure 11. Experimental results. Objective quality curves and computational time.

The quality of ZF methods has an obvious gap between the CS methods either in PSNR or SSIM assessment. The quality of the re-gridding method is proportional with the resolution size since the optimization algorithm.

There is also another SUT named as 'cross' for the new system. In the SUTs, this sample contains a marine cross stuff and a same material strip. Compared with the three small patches target shown in Figure 10, the second SUT could be used to analyze the performance of the boundary of the reconstruction with new imaging system and algorithm. Figure 12 shows all reconstructions from different approaches. The objective quality assessments of the reconstructions in Figure 12 are similar with the results in Figure 11.

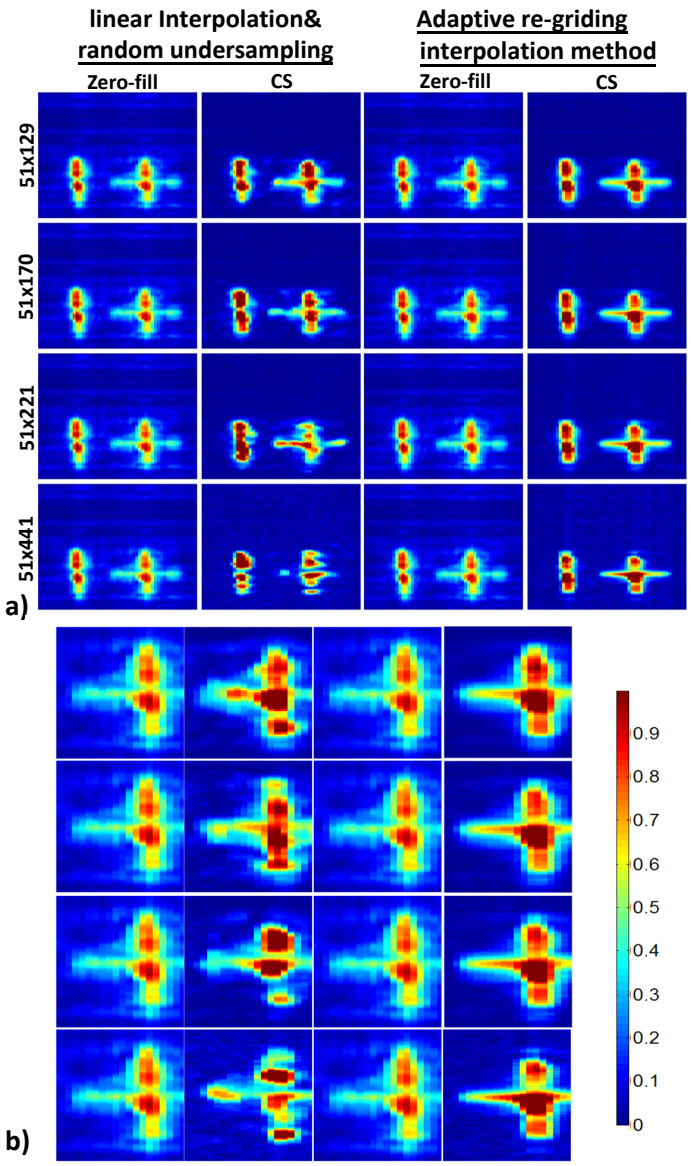

Figure 12. Experimental results.a) The 'cross' sample reconstructions in 1D experiment. b) Drawing of partial enlargement.

'Cross' reconstructions have illustrated the improvement both in re-gridding and CS-based method. Zero-filling reconstructions, same as in Figure 10, are filled with artifacts and noise. Zoomed out boundary images clearly show the blurring noise on boundaries. CS-based without re-gridding reconstructions have 'disappearance' shape. More interested target's pixels are reducing with higher size of resolution with this method. It is caused by the truncation error during interpolation procedure and the threshold in sparsifying procedure

wrongly forced them to zero. Compared with the others, reconstructions from CS-based method with re-gridding has no blurring, disappearing, nor artifacts in all reconstructions. Even with 51×129, the reconstruction has very clear boundary, entire shape, and high contrast. The difference is more obvious in the zoomed out sub-figure.

4.4. 2D Reconstruction. We also test the performance of an entire proposed imaging system. There are totally 16 transmitter and receiver boards configured on it. As we used electric switches to replace the mechanical arm, the measuring time have been highly reduced. We also tested it with the 'cross' sample. Figure 13 shows the reconstructions from the prototype.

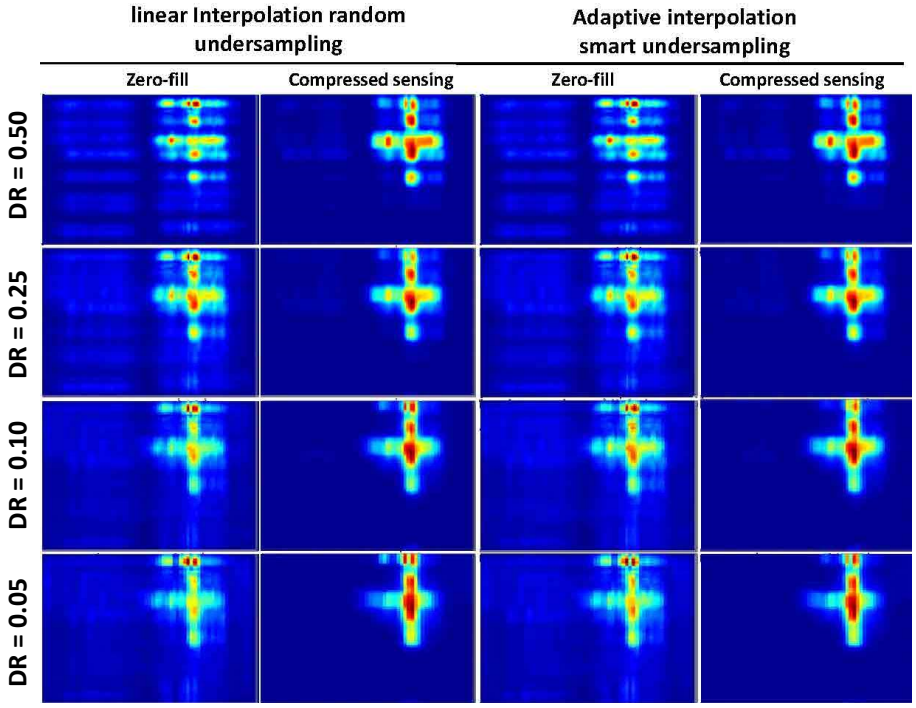

Figure 13. Experimental results. The 'cross' sample reconstructions in 2D experiment.

Though we have much less measurements (only 241 nearest-neighbor transmitter and receiver pairs on the prototype), the reconstructions shown in Figure 13 with the proposed method still have very clear boundary, smooth background, and high-contrast interested area.

4.5. Reconstruction Artifacts. The reconstruction artifacts in our study are mainly from three parts: 1. The phase errors in the imaging system. 2. The truncation errors in interpolation; 3. The shrink errors in l_1 reconstructions.

During the measuring and reconstructing, we assumed the transmitter subarray, the receiver subarray, and the approximated transceiver array are all on the $z = 0$ plane, and totally parallel to the SUTs plane ($z = z_0$). In the practical application, the transmitter and receiver subarrays must staggered up and down. And the parallelism is also hard to ensure. As a result, there are slightly errors for the distance R shown in Figure 3, and in the (2), the phase components will have an error near plus or minus 5° as estimated.

Coefficients from l_1 reconstruction tend to slightly smaller than in the original signal [28]. And to save the computing time, we used the identity matrix as the sparsifying transformation. Several small features have been deleted during the CS iteration shown in Figure 12. However, as the SAR measurements and images have high contrast (The reflection ratios have a obvious difference between the background and the interest) and less small features (the frequency is in Ka-band, the real size of SAR images is in millimeter level, where the most interested features are large enough in reconstruction), CS is particularly attractive in the SAR applications.

5. CONCLUSION

We have presented a novel random bistatic configuration SAR imaging system model, proposed a new re-gridding method for interpolation algorithms, and applied the CS-based method for reconstruction. We demonstrated experimental verification of several implementations for 2D imaging. We showed that with many fewer antenna elements, the novel SAR imaging system can reconstruct high quality images. We demonstrate a high resolution SAR image that only needs less than two minutes in measuring and reconstructing with the new model and the proposed method.

ACKNOWLEDGMENTS

The work was supported in part by the US Department of Defense STTR project W31P4Q-14-C-0146, the Intelligent Systems Center of Missouri University of Science and Technology, and the WilkenâĂŹs Missouri telecommunication endowment fund.

REFERENCES

[1] M. Pastorino, *Microwave imaging*. John Wiley & Sons, 2010, vol. 208.

[2] D. M. Sheen, D. L. McMakin, and T. E. Hall, "Three-dimensional millimeter-wave imaging for concealed weapon detection," *IEEE Trans. Microw. Theory Tech.*, vol. 49, no. 9, pp. 1581–1592, Mar. 2001.

[3] J. T. Case, M. T. Ghasr, and R. Zoughi, "Optimum 2—D nonuniform spatial sampling for microwave SAR-based NDE imaging systems," *IEEE Trans. Instrum. Meas*, vol. 61, no. 11, pp. 3072–3083, Nov. 2012.

[4] M. T. Ghasr, J. T. Case, and R. Zoughi, "Novel reflectometer for millimeter-wave 3-d holographic imaging," *IEEE Trans. Instrum. Meas.*, vol. 63, no. 5, pp. 1328–1336, Jan. 2014.

[5] H. Kajbaf, J. T. Case, Z. Yang, and Y. R. Zheng, "Compressed sensing for sar-based wideband three-dimensional microwave imaging system using non-uniform fast Fourier transform," *IET. Radar, Sonar & Navigation*, vol. 7, no. 6, pp. 658–670, May. 2013.

[6] Z. Yang and Y. R. Zheng, "Near-field 3-D synthetic aperture radar imaging via compressed sensing," in *Acoustics, Speech and Signal Process. (ICASSP), 2012 IEEE Int. Conf. on*. IEEE, Aug. 2012, pp. 2513–2516.

[7] X. Yang, Y. R. Zheng, M. T. Ghasr, K. M. Donnell, and R. Zoughi, "Microwave synthetic aperture radar imaging using sparse measurement," in *Instrum. Meas. Conf. Proc. (I2MTC), 2016 IEEE International*. IEEE, Jul. 2016, pp. 1–5.

[8] Z. Manzoor, M. T. Ghasr, and K. M. Donnell, "Image distortion characterization due to equivalent monostatic approximation in near field bistatic sar imaging," in *2017 IEEE Int. Instrumentation and Measurement Technology Conference (I2MTC)*, May 2017, pp. 1–5.

[9] Y. L. Neo, F. Wong, and I. G. Cumming, "A two-dimensional spectrum for bistatic sar processing using series reversion," *IEEE Trans. Geosci. Remote Sens. Letter*, vol. 4, no. 1, pp. 93–96, Jan. 2007.

[10] I. Walterscheid, J. H. G. Ender, A. R. Brenner, and O. Loffeld, "Bistatic sar processing and experiments," *IEEE Trans. Geosci. Remote Sens.*, vol. 44, no. 10, pp. 2710–2717, Sep. 2006.

[11] O. Loffeld, H. Nies, V. Peters, and S. Knedlik, "Models and useful relations for bistatic sar processing," *IEEE Trans. Geosci. Remote Sens.*, vol. 42, no. 10, pp. 2031–2038, Oct.2004.

[12] Y. Wu, Y. Huang, and X. Wu, "A equivalent monostatic imaging algorithm for bistatic synthetic aperture radar," in *Synthetic Aperture Radar, 2007. APSAR 2007. 1st Asian and Pacific Conference on*. IEEE, 2007, pp. 94–97.

[13] M. Xu and L. V. Wang, "Universal back-projection algorithm for photoacoustic computed tomography," *Physical Review E*, vol. 71, no. 1, p. 016706, Jan. 2005.

[14] I. G. Cumming and F. H. Wong, "Digital processing of synthetic aperture radar data," *Artech house*, vol. 1, no. 2, p. 3, 2005.

[15] A. S. Milman, "SAR imaging by ω- κ migration," *Int. J. of Remote Sensing*, vol. 14, no. 10, pp. 1965–1979, May. 1993.

[16] Z. Yang and Y. R. Zheng, "A comparative study of compressed sensing approaches for 3-D synthetic aperture radar image reconstruction," *Elsevier Digital Signal Process.*, vol. 32, pp. 24–33, May 2014.

[17] D. L. Donoho, "Compressed sensing," *IEEE Trans. Inf. Theory*, vol. 52, no. 4, pp. 1289–1306, Apr. 2006.

[18] D. Bi, Y. Xie, X. Li, and Y. R. Zheng, "Efficient 2-d synthetic aperture radar image reconstruction from compressed sampling using a parallel operator splitting structure," *Digital Signal Processing*, vol. 50, pp. 171–179, 2016.

[19] D. Bi, L. Ma, X. Xie, Y. Xie, X. Li, and Y. R. Zheng, "A splitting bregman-based compressed sensing approach for radial ute mri," *IEEE Trans. on Applied Superconductivity*, vol. 26, no. 7, pp. 1–5, 2016.

[20] D. Bi, Y. Xie, and Y. R. Zheng, "Synthetic aperture radar imaging using basis selection compressed sensing," *Circuits, Systems, and Signal Processing*, vol. 34, no. 8, pp. 2561–2576, Sept. 2015.

[21] E. J. Candès, J. Romberg, and T. Tao, "Robust uncertainty principles: Exact signal reconstruction from highly incomplete frequency information," *IEEE Trans. Inf. Theory*, vol. 52, no. 2, pp. 489–509, Jan. 2006.

[22] B. D. Rigling and R. L. Moses, "Polar format algorithm for bistatic sar," *IEEE Trans. Aerosp. Electron. Syst.*, vol. 40, no. 4, pp. 1147–1159, Oct. 2004.

[23] K. Gröchenig and T. Strohmer, "Numerical and theoretical aspects of nonuniform sampling of band-limited images," in *Nonuniform Sampling*. Springer, 2001, pp. 283–324.

[24] J. Keiner, S. Kunis, and D. Potts, "Using NFFT 3 — a software library for various nonequispaced fast fourier transforms," *ACM Trans. on Mathematical Software (TOMS)*, vol. 36, no. 4, p. 19, Aug. 2009.

[25] J. Bergh and J. Lofstrom, *Interpolation spaces: an introduction*. Springer Science & Business Media, 2012, vol. 223.

[26] F. N. Fritsch and R. E. Carlson, "Monotone piecewise cubic interpolation," *SIAM Journal on Numerical Analysis*, vol. 17, no. 2, pp. 238–246, Jul, 1980.

[27] C. De Boor, C. De Boor, E. U. Mathématicien, C. De Boor, and C. De Boor, *A practical guide to splines*. Springer-Verlag New York, 1978, vol. 27.

[28] M. Lustig, D. L. Donoho, and J. M. Pauly, "Sparse MRI: The application of compressed sensing for rapid MR imaging," *Magnetic Resonance in Medicine*, vol. 58, no. 6, pp. 1182–1195, Oct. 2007.

[29] A. S. Khwaja and J. Ma, "Applications of compressed sensing for SAR moving-target velocity estimation and image compression," *IEEE Trans. Instrum. Meas.*, vol. 60, no. 8, pp. 2848–2860, Aug. 2011.

II. MICROWAVE IMAGING FROM SPARSE MEASUREMENTS FOR NEAR FIELD SYNTHETIC APERTURE RADAR (SAR)

Xiahan Yang, Yahong Rosa, Zheng, Mohammad Tayeb Ghasr, Kristen M. Donnell

Department of Electrical & Computer Engineering

Missouri University of Science and Technology

Rolla, Missouri 65409–0040

Tel: 573–341–6622, Fax: 573–341–4115

Email: {xy6v4, zhengyr, mtg7w6, kmdgfd}@mst.edu

ABSTRACT

This paper reports experimental studies for four image reconstruction methods from sparse measurement using wide-band microwave synthetic aperture radar (SAR) systems. The four methods include two denoising methods using zero-filling (ZF) and non-uniform fast Fourier transform (NUFFT), and two compressed sensing methods using the orthogonal matching pursuit (OMP) and the conjugate gradient (CG) algorithms. The specimens under test (SUTs) consist of a tray of small rocks with different densities with/without one piece wrapped in aluminum foil. The raw measurements of the SUTs are randomly undersampled in the spatial domain and the images are reconstructed from measurements of 10% – 60% sparse-sampling rates. The results show that the CS method achieves good image quality with as low as 30% sparse-sampling rate, while ZF and NUFFT require 50% to obtain acceptable quality. An enhanced Otsu's method is also proposed to detect the foiled rock from sparse reconstructions, which improves detection performance for sparse-sampling rate of 5% - 15%. The reduction of spatial measurement leads to reduced cost or reduced measurement time.

Keywords: Synthetic Aperture Radar, Compressed Sensing, Microwave Imaging, Nondestructive Evaluation

1. INTRODUCTION

Microwave and millimeter-wave imaging techniques have shown tremendous potential for nondestructive evaluation (NDE) because these techniques can effectively inspect a wide range of complex composite structures, materials, and applications [1, 2]. An imaging radar uses the relative motion between the antenna platform and the specimen under test (SUT) to interrogate a scene with frequency swept wideband signals that reveal the spatial distribution of the target. When the phase coherency is maintained at the receiver from sweep to sweep, it is equivalent to a larger aperture replacing a diverse set of short apertures, hence the term synthetic aperture radar (SAR). Wide-band SAR can evaluate the inner structure of a SUT to render a comprehensive image for inspection. For NDE applications, microwave and millimeter wave frequencies in the range of 3 - 100 GHz are widely used which produce high cross-range resolution. Furthermore, due to the available large bandwidth, high range resolution is also achieved.

Several high-resolution SAR imaging systems have been developed [1, 2, 3]. An accurate and highly sensitive imaging probes platform has been demonstrated to detect and quantify small flaws within SUTs [4]. However, based on the traditional sampling theory, high spatial resolution requires a small sampling size so that the spatial sampling rate is greater than the Nyquist sampling rate to avoid aliasing and to preserve the quality of image reconstruction [2]. The traditional sampling higher than Nyquist sampling rate results in a large number of measurements, which leads to long acquisition time for reasonably sized SUTs. As a result, there is great interest in reducing the number of measured spatial points.

Image reconstruction methods with sparse measurement include two categories [5]: (1) the denoising method which includes zero-filling (ZF) and non-uniform fast Fourier transform (NUFFT) [6]; (2) compressed sensing (CS) techniques. The basic idea of CS image reconstruction is to recover the sparse representation of the images from sparse measurements. If the sparsity of the images is lower than the number of sparse measure-

ments and the coherence between the sparse representation matrix and the measurement matrix satisfies the *restricted isometry property* (RIP), then the images can be perfectly reconstructed.

In recent years, CS techniques have been applied to radar signal processing and radar imaging [7, 8]. Since the CS approach requires non-convex optimization of L_1 norm, iterative methods are often used to solve the CS reconstruction. CS reconstruction can achieve small reconstruction errors and satisfactory image qualities with less than 50% of the fully-sampled measurements. In the microwave SAR experiment, fewer measurements points means saving time or reducing cost while maintaining resolution. In raster scanning SAR imaging systems, if only 30% spatial points are visited, then scanning time is reduced to a half [9]. In near-field array imagers, if the numbers of transmit and receive antenna elements are reduced to 30%, then the cost of the imager is reduced to 20% of the full cost. Additionally, millimeter wave antenna elements are usually large in size, which constrains the minimum distance between each two elements, which in turn limits the imaging resolution with the conventional Nyquist sampling approach. The CS approach allows sparsely-spaced elements, and if designed properly, can obtain resolution as high as those reconstructed from densely sampled data in equally-spaced arrays.

The commonly used CS iterative algorithms include the orthogonal matching pursuit (OMP) algorithm [10], the majorization-minimization algorithm [11], and the nonlinear conjugate gradient (CG) algorithm [12]. Commonly used sparse representation matrices in CS include the Identity matrix, discrete cosine transform (DCT), and many types of wavelet transforms [13], such as Battle, Beylkin, Daubechies, Symmlet Vaidyanathan, and Haar. CS has been proposed as an efficient signal reconstruction method for random samples of spectrally sparse signal/image. The selection of CS iterative algorithms and the design of proper sparse representation matrix can have significant impact on the quality of reconstructed images. In [14], the authors used CS in an SAR algorithm to estimate moving target velocities. Furthermore, online compression of processed SAR images with

the help of curvelet sparsity-promoting offline decoding was performed. In [15], the author used curvelet thresholding for CS to recover remote sensing images. In [16], the authors proposed a fast and simple CS recovery algorithm to reduce the computational cost. In [17], the authors used CS-based method to acquire high-resolution images with a low-resolution camera. In [9] and [18], we implemented under-sampling in physical SAR measurements and MRI measurements simulated measurement.

To guide the selection of image reconstruction algorithms and sparse measurement parameters, this paper reports experimental studies on several SUTs consisting of different densities of rocks placed on a tray with and without a center piece of rock wrapped by aluminum foil. As foil is a significant scatter, it was included to create a high scattering contrast in the different scene complexities provided by the varying rock densities. The microwave SAR measurements were then taken with full grid scanning, and the data was sampled to yield different sparse sampling rates of the raw measurements. Although this study uses electronic selection to generate the sparse sampling data, the developed microwave imaging system can sample directly with any sparse sampling rate, as reported in [9, 19].

Reconstructions from four methods are then compared: ZF, NUFFT denoising, CS with OMP, and CS with CG algorithms. The results show that the two CS methods always perform better than the two denoising methods when the sparse sampling rate is lower than 50%. The presence or absence of the foiled rock in the SUT can be detected in the CS-reconstructed images with a sparse sampling rate as low as 5%, while the denoising methods require a minimum sparse sampling rate of 15% to detect the presence/absence of the foiled rock. To classify the density of the normal rocks, however, the CS-reconstructed images require 30% sparse sampling rate and the denoising-based reconstructions require 50% sparse sampling rate. Structural similarity (SSIM) [20] and peak signal-to-noise ratio (PSNR) [21] are commonly used metrics for 2-D image quality evaluation. They are considered consistent with human eye perception. The SSIM and PSNR metrics of

the reconstructed images over fully-sampled reconstructions are also used in this study, and results demonstrate high gain in CS-based methods over denoising-based methods, especially at low sparse sampling rates. In addition, the performance of the CG-CS method depends heavily on the choice of the sparse representation matrix. When the matrix is selected properly, the CG-CS shows large gain over the other three methods in low sparse sampling rate less than 30% [18].

We also introduce an object detection method for the SAR sparse reconstructions. It is reasonable to detect a large scattering object, which is the conductor in the SAR case. Many different methods have been studied [22, 23]. Nevertheless, reconstructed images using the CS methods with sparse measurements may suffer heavily from noise and artifacts. Therefore, we enhanced the Otsu's method by adding a new denoising method to detection masks [13]. This enhanced Otsu's detection method is effective and robust for detecting compressed sensing reconstructions. This algorithm has more than 90% accuracy in the conductor detection with only 15% measurements for CS reconstructed images.

2. SPARSE SAR IMAGING RECONSTRUCTION METHODS

A wideband monostatic 2-D SAR imaging system is illustrated in Figure 1 in a 3-D Cartesian space. A probe is located on the XY-plane and scans the SUT located on the 2-D plane defined by $z = z_0$. Assume the size of the measurement region is $R_x \times R_y$ and the scanning step sizes in the X and Y dimensions are a_x and a_y, respectively. At each probing point $(u, v, 0)$, the probe transmits a set of pulse $\omega_i \in [\omega_{min}, \omega_{max}]$ with a step size $\triangle\omega$, so that the total number of frequencies $N_\omega = (\omega_{max} - \omega_{min})/\triangle\omega + 1$. A point (x, y, z_0) on the SUT reflects the incident microwave energy. The measurement is characterized by its complex reflectivity function $g_i(x, y, z_0)$ at the probing frequency ω_i.

The imaging probe is located at $(u, v, 0)$ and the SUT is located on the plane defined by $z = z_0$. The range between the probe and a point on the SUT (x, y, z_0) is R. If the system is near-field (*i.e.* the value z_0 is small), then the wavefront curvature is no longer negligible.

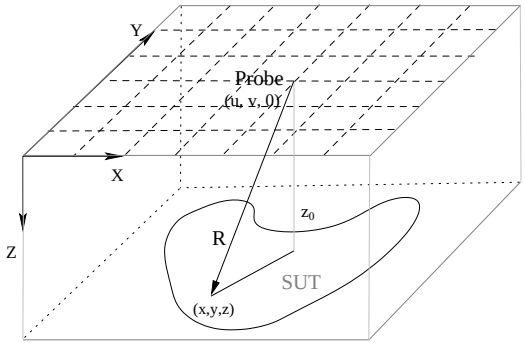

Figure 1. The SAR system model.

The received spherical signal $r(u, v, \omega_i)$ satisfies [3]:

$$r(u, v, \omega_i) = \iint g_i(x, y, z_0) e^{j2\kappa_i(z_0 - R)} dx dy \tag{1}$$

where $R = \sqrt{(u-x)^2 + (v-y)^2 + z_0^2}$, $j = \sqrt{-1}$, and $\kappa_i = \omega_i / v$ is the wavenumber, with v being the velocity in the medium.

Using the plane wave decomposition for the spherical wave and Stolt transform[24], the reconstructed image of the SUT at the probing frequency ω_i is given by [8]:

$$\hat{g}_i(x, y, z_0) = \Im_{2D}^{-1} \left\{ \Im_{2D} \left[r(u, v, \omega_i) e^{-j z_0 \kappa_z} \right] \right\}, \; i = 1, 2, \ldots N_\omega. \tag{2}$$

where κ_z is the wavenumber in the Z axis, related to angular frequency ω_i by the dispersion relation: $\kappa_z = \sqrt{(2\omega/c)^2 - \kappa_x^2 - \kappa_y^2}$. which provides phase correction for all frequencies when back propagating the data to form an image at z_0 [3, 18, 2]. The operator $\Im_{2D}[\cdot]$ denotes the 2-D discrete Fourier transform (DFT) operator and $\Im_{2D}^{-1}$ denotes the inverse 2-D

DFT operator along the XY-plane defined by

$$\begin{aligned} F(u,v) &= \mathfrak{F}_{2D}\left[f(x,y)\right] \\ &= \frac{1}{\sqrt{MN}} \sum_{x=0}^{M-1} \sum_{y=0}^{N-1} f(x,y) e^{-j2\pi(ux/M+vy/N)} \\ f(x,y) &= \mathfrak{F}_{2D}^{-1}\left[F(u,v)\right] \\ &= \frac{1}{\sqrt{MN}} \sum_{u=0}^{M-1} \sum_{v=0}^{N-1} F(u,v) e^{j2\pi(ux/M+vy/N)} \end{aligned} \tag{3}$$

where $f(x, y)$ is a digital image with size $M \times N$, and $M = R_x/a_x$ and $N = R_y/a_y$.

With measurements from all frequencies, the final reconstructed image is the average of N_ω images of individual frequencies:

$$\hat{g}(x, y, z_0) = \frac{1}{N_\omega} \sum_{i=1}^{N_\omega} \hat{g}_i(x, y, z_0) \tag{4}$$

To utilize matrix notations, we concatenate the fully-sampled raw measurement $r(u, v, \omega_i)$ and the reconstructed image $\hat{g}_i(x, y, z_0)$ into $N_{xy} \times 1$ vectors $\mathbf{r}_i$ and $\hat{\mathbf{g}}_i$, respectively, where $N_{xy} = MN$. Correspondingly, the 2-D DFT can be expressed as an $N_{xy} \times N_{xy}$ matrix $\mathbf{W}$ with its (p, q)-th element being $w_{pq} = \frac{1}{\sqrt{MN}} e^{j2\pi \frac{pq}{MN}}$. Therefore, the SAR operator in (1) can be rewritten as

$$\boldsymbol{\Upsilon}_i = \mathbf{W}^{-1} \mathbf{P}_i \mathbf{W} \tag{5}$$

where $\mathbf{P}_i$ is the diagonal phase correction matrix for frequency ω_i and its n-th diagonal element is defined as $p_i(n) = e^{jz_0\sqrt{4\kappa_i^2 - \kappa_x(n)^2 - \kappa_y(n)^2}}$, with $n = 1, 2, \cdots, N_{xy}$.

The reconstructed image from the fully-sampled measurements can be calculated as

$$\hat{\mathbf{g}} = \frac{1}{N_\omega} \sum_{i=1}^{N_\omega} \hat{\mathbf{g}}_i = \frac{1}{N_\omega} \sum_{i=1}^{N_\omega} \boldsymbol{\Upsilon}_i \mathbf{r}_i \tag{6}$$

2.1. Sparse Measurement and Image Reconstruction with ZF and NUFFT. In this study, we use a measurement matrix $\mathbf{\Phi}$ designed to randomly take a small number of samples from the full measurement vector $\mathbf{r}_i$. This matrix is satisfied by the trajectory of the imaging probe or the spatial placement of array structure. If the number of sparse measurements is Q, then the sparse sampling rate is $\rho = Q/N_{xy}$. The random measurement matrix is thus a $Q \times N_{xy}$ matrix with all elements as zero except for those of Q. Only a single element in each row is one and each column contains at most one 1 in $\mathbf{\Phi}$. The received sparse measurement signal can be expressed as

$$\mathbf{s} = \mathbf{\Phi r} \tag{7}$$

Note that the subscript i is dropped for notation convenience with the understanding that the sparse measurement and image reconstruction is performed for all frequencies. The final image is an average of all reconstructions as in (6).

For the data sampled as the Nyquist sampling rate (i.e., 100%)[18], the uniform $\omega - k$ algorithm generates the ground truth SAR image for this investigation. The block diagram for this algorithm is shown in Figure 2a.

For sparse measurements, a straightforward method for image reconstruction is zero-filling (ZF) which simply fills the missing data points with zeros. Let $\mathbf{\Theta}$ be the ZF operator thus making $\mathbf{\Theta} = \mathbf{\Phi}^T$, where the superscript T denotes matrix transpose. The image is then reconstructed by taking SAR over the zero-filled signal as

$$\mathbf{\Upsilon}_{\text{ZF}}\mathbf{s} = \Im_{2D}^{-1}\left[\Im_{2D}(\mathbf{\Theta s}) \cdot e^{-jz_0\kappa_z}\right] \tag{8}$$

It is clear that $\mathbf{\Upsilon}_{\text{ZF}}$ is a linear operator that can result in aliasing when the sparse sampling rate is low. There is no additional computational cost in the reconstruction over the conventional full sampling SAR. The block diagram of the ZF algorithm is shown in Figure 2b.

In this study, we also applied the non-uniform fast Fourier transform (NUFFT) as a reconstruction method in the SAR imaging experiment [2]. The NUFFT method was first applied to nearfield 3D SAR image reconstruction [6] in the Z-axis to combat the non-uniform spacing. The NUFFT method was recently applied to a sparse-measurement SAR image reconstruction in [2, 8, 9] to replace 2D DFT in the XY domains. The NUFFT operator in the XY domains is defined as

$$\mathfrak{F}_{\text{NUFFT}}[s(u,v,\omega)] = \sum_{n=1}^{N_{xy}} a_n s(u,v,\omega) e^{-j(uk_x+vk_y)} \tag{9}$$

where a_n is the nth coefficient of the kernel function found from the polygons of a Voronoi diagram [25] and $s(u,v,\omega)$ is the sparse measurement at location (u,v) with frequency ω.

With (9), the image reconstruction from the sparse measurements is then

$$\boldsymbol{\Upsilon}_{\text{NU}}\mathbf{s} = \mathfrak{F}_{2D}^{-1}\left[\mathfrak{F}_{\text{NUFFT}}(\mathbf{s}) \cdot e^{-jz_0\kappa_z}\right] \tag{10}$$

A computationally efficient 2-D NUFFT algorithm is given in [6]. However, the NUFFT method may result in a high level of image artifacts when the sparse sampling rate is low, as shown in the experimental results section. The block diagram of the NUFFT algorithm is shown in Figure 2c.

The raw sparse measurements $\mathbf{s} = \{s(u,v,\omega)\}$ are converted into full images $\hat{g}(x,y,z_0)$. Figure 2 illustrates (a) the $\omega - k$ method to reconstruct fully-sampled measurements, (b) the zero-filling method to reconstruct sparse-sampled measurements, and (c) the NUFFT method to reconstruct sparse-sampled measurements.

2.2. Compressed Sensing Image Reconstruction. In contrast to the two conventional methods of sparse reconstruction, the CS-based method takes advantage of the sparse representation of the images and iteratively recovers the coefficients of the sparse domain representation from the sparse measurements. Let $\boldsymbol{\Psi}$ be the sparse representation matrix of

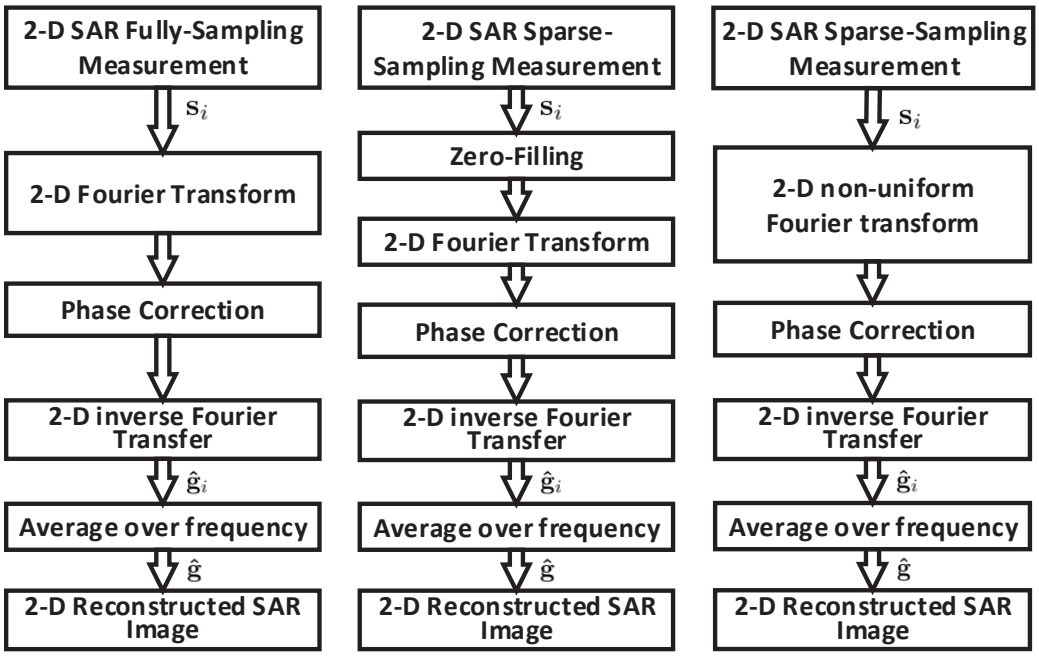

(a) $\omega - k$ (b) ZF (c) NUFFT

Figure 2. Block diagrams of conventional reconstruction methods with sparse measurement.

the image. The CS image reconstruction requires that the following be solved:

$$\begin{aligned} \hat{\mathbf{g}} &= \underset{\mathbf{g}}{argmin}\, ||\mathbf{\Psi g}||_1, \\ &\text{subject to } ||\mathbf{\Phi \Upsilon}^{-1}\mathbf{g} - \mathbf{s}||_2^2 < \epsilon_0^2 \end{aligned} \tag{11}$$

where $\hat{\mathbf{g}}$ is the reconstructed image in matrix form, $||\cdot||_i$ is the l_i norm with $i = 1, 2$, parameter ϵ is the error tolerance, and $\mathbf{\Upsilon}$ is the SAR operator defined in (5).

A number of CS algorithms have been successfully implemented for near-field SAR image reconstruction from sparse measurements [8, 9]. This work adopts the Orthogonal Matching Pursuit (OMP) [26] and nonlinear conjugate Gradient (CG) algorithms by incorporating the 2D near-field SAR operator into the CS iterative algorithms. A summary of

the two CS algorithms is given in Figure 3, where the sparse representation matrix is pre-selected. Note that in OMP-CS method, the sparse representation matrix is not necessary. The details of the OMP and CG algorithms are shown in Algorithm 1 and 2 respectively.

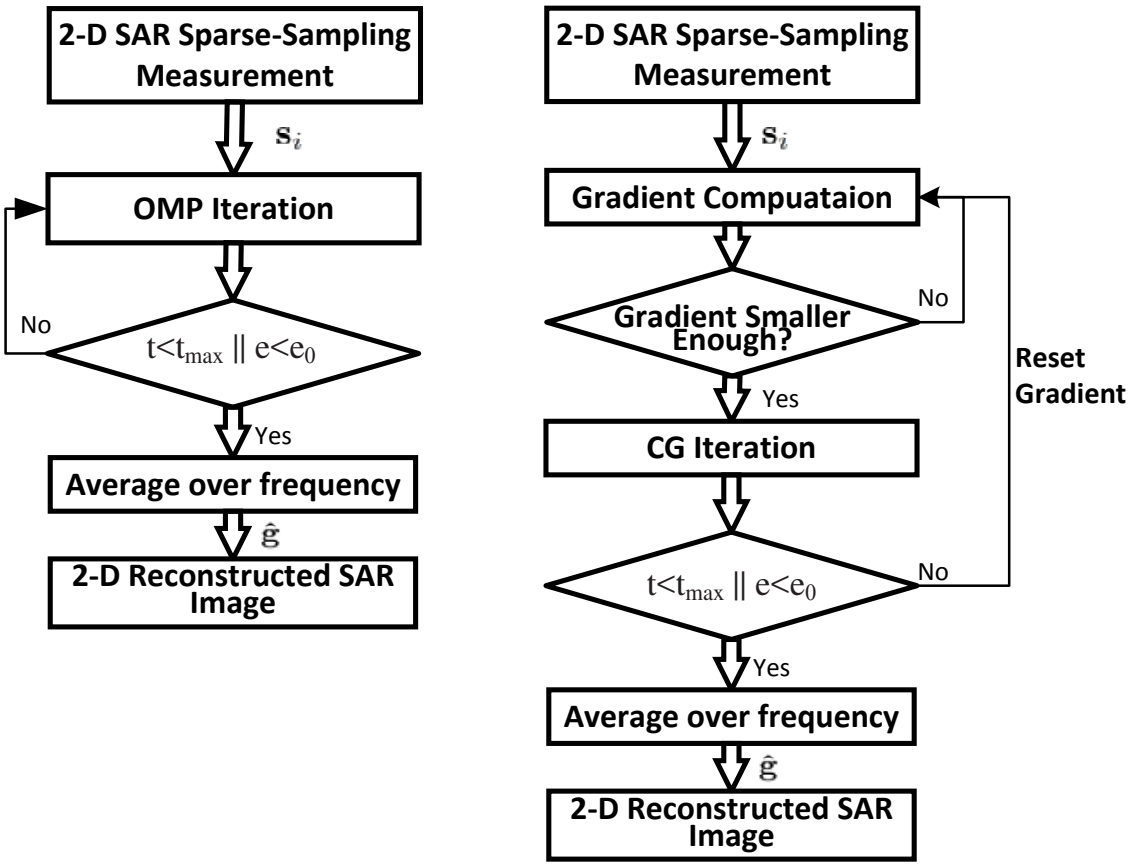

(a) OMP-CS (b) CG-CS

Figure 3. Flow diagrams of CS reconstruction algorithms.

There are several apparent differences between the OMP and CG algorithms. First of all, the OMP method does not need a priori knowledge of sparsity of the image, which is necessary in the CG-CS method. In the microwave SAR experiments, we have used wavelet transform with different bases as sparse transform in the CG-CS method.

Second, OMP is a greedy algorithm with low computational complexity, while the CG algorithm is sophisticated with two layers of iterations. Compared with the OMP method, the computational cost of the CG method is much higher. However, the quality of reconstruction using the CG method is usually higher than that of the OMP because the CG

Algorithm 3 Orthogonal Matching Pursuit

Require:

Sparse measurements $\mathbf{s}$;
Sparse domain $\mathbf{\Psi}$;
SAR operator $\mathbf{\Upsilon}$;
Stopping criteria t_{max} and TolGrad

Ensure:

Reconstructed image $\hat{\mathbf{g}}$;
Initialization: $\beta_0 = \mathbf{s}$; $\lambda_0 = \emptyset$; $t = 1$;
$\mathbf{B} = \mathbf{\Psi}\mathbf{\Upsilon}^{-1}$;
$\mathbf{\Gamma}_0 = \{\mathbf{B}_j\}_{j=1}^{\hat{N}_{xy}}$;
while $(t \geqslant t_{max})$ and $(||\mathbf{g}_t||_2$ <TolGrad) **do**
    $\mathbf{\Gamma}_t = \mathbf{\Gamma}_{t-1} \setminus \lambda_{t-1}$;
    $\lambda_t = \underset{\lambda_j \in \mathbf{\Gamma}_t}{argmax} | < \beta_{t-1}, \lambda_j > |$
    $\hat{\mathbf{g}} = \underset{\mathbf{g}}{argmin} ||\mathbf{s} - \mathbf{B}\mathbf{g}||_2$
    $\beta_t = \mathbf{s} - \mathbf{B}\hat{\mathbf{g}}$;
    $t = t + 1$.
end while

algorithm guarantees a global optimal solution, while the OMP algorithm may only achieve a local optimal solution. Let the quadratic function $f(\mathbf{g})$ be the cost function that computes the "distance" between the recovery signal and the ideal signal.

Selecting a sparse representation matrix in CS is essential for an accurate recovery of the measurement, especially where neither the raw data $\mathbf{r}$ or the reconstructed SAR image $\hat{\mathbf{g}}$ is sparse. The efficiency of sparse representations in different wavelet transforms, such as Haar, Coiflet, and Daubechies, depends mostly on the regularity of the raw signal, the number of vanishing moments, and the size of support. As SAR signals have different characteristics, such as the rock density in this study, applying one fixed basis to all conditions is often inflexible in capturing the regularity in some special cases.

Algorithm 4 Conjugate Gradient

Require:

Sparse measurements $\mathbf{s}$;
Sparse representation domain $\mathbf{\Psi}$;
SAR operator $\mathbf{\Upsilon}$;
Stopping criteria t_{max} and TolGrad;
Gradient step size: η

Ensure:

The estimated recovery image $\hat{\mathbf{g}}$;
Initialization: $t = 0$; $\mathbf{g}_0 = \mathbf{0}$; $\mathbf{m}_0 = \nabla f(\mathbf{g}_0)$; $\triangle \mathbf{g}_0 = -\mathbf{m}_0$
while $(t \geqslant t_{max})$ and $(||\mathbf{g}_t||_2 <$TolGrad) **do**
    $\delta = 1$
    while $f(\mathbf{g}_t + \eta \triangle \mathbf{g}_t) > f(\mathbf{g}_t) + \alpha\delta \text{Real}[\mathbf{m}_t^* \triangle \mathbf{g}_t]$ **do**
        $\delta = \eta\delta$
    end while
    $\mathbf{g}_{t+1} = \mathbf{g}_t + \delta \triangle \mathbf{g}_t$
    $\mathbf{m}_{t+1} = \nabla f(\mathbf{g}_t)$
    $\nabla \mathbf{g}_{t+1} = -\mathbf{m}_{t+1} + \dfrac{||\mathbf{m}_{t+1}||_2^2}{||\mathbf{m}_t||_2^2} \triangle \mathbf{g}_t$
    $t = t + 1$;
end while
return $\hat{\mathbf{g}} = \mathbf{g}_{t-1}$

3. OBJECTIVE DETECTION

The reconstructed images are post-processed for identification, classification, or object detection. Image detection uses features such as color histograms, texture measures, and shape measures. Detection methods for strong scattering objects have been surveyed for rock detection and object detection in [13, 22, 23, 27, 28], mostly with colored images. However, the reconstruction in the microwave SAR experiment is a grayscale image, which highly reduces the complexity in detection. In this study, the foil-wrapped rock is the strongest scattering object in the SUT since it is a conductor with irregular shape. However, images reconstructed from the sparse-sampled measurements contain strong noise and

artifacts, which reduced accuracy and robustness and increased the false alarm rate in existing algorithms. In this study, we enhance the Otsu's method for conductor detection of sparsely-sampled reconstructions.

Otsu's method, as an optimum global thresholding method, is an attractive method used to automatically threshold a gray level image to a binary image [13]. It is particularly suited for the SAR images because SAR images are grayscale image. We choose Ostu's method because it is self-adaptive and requires low computational resources. Otsu's method calculates the optimum threshold that maximizes the between-class variance. Furthermore, Otsu's method performs well for grayscale images in this investigation and more complex methods may not provide better performance given their complexities. The enhanced Otsu's method has low-computational cost, requires no learning process, and needs only one external parameter which thresholds the conductor reflective rate. The accuracy of the proposed method will be shown in Sec. 4.

The enhanced Otsu's method has six steps:

Step 1): Obtain Otsu's threshold of the SAR reconstructed image $\hat{\mathbf{g}}$:

$$\begin{aligned} k = \ & arg\min_{k} \frac{[m_g P_i(k) - m(k)]^2}{P_i(k)[1 - P_i(k)]} \\ \text{s.t.} \quad & P_i(k) = \sum_{i=0}^{k} n_i/N_g, \ m_g = \sum_{i=0}^{L-1} iP_i(k), \ m(k) = \sum_{i=0}^{k} iP_i(k), \end{aligned} \tag{12}$$

where N_g is the number of pixels in $\mathbf{g}$ and n_i is the number of pixels in $\mathbf{g}$ with intensity equal to i.

Step 2): Compute Otsu's thresholding image, B, using Otsu's threshold k from step 1.

Step 3): Compute the denoising mask, $\tilde{B}(i, j)$, using the following:

$$\tilde{B}(i,j) = \begin{cases} 1, & \sum_{n_i=-1}^{1} \sum_{n_j=-1}^{1} B(i \pm n_i, j \pm n_j) = 9 \\ 0, & \text{otherwise.} \end{cases} \tag{13}$$

Step 4): Label the denoising mask with a set of small region masks $\mathbf{C} = \{C_1, \ldots C_n\}$ using Algorithm. 5.

Step 5): Obtain the masked images $\hat{\mathbf{g}}(C_i)$ using:

$$\hat{\mathbf{g}}(C_i) = \hat{\mathbf{g}} \cdot C_i, \; i = 1, 2, \ldots n \tag{14}$$

Step 6): Detect whether $\hat{\mathbf{g}}(C_i)$ is a conductor, using:

$$\mathrm{H}_i = \begin{cases} 1, & E\{\hat{\mathbf{g}}(C_i)\} > T \\ 0, & \text{otherwise} \end{cases} \tag{15}$$

where T is the detection threshold and H is the hypothesis that the i-th masked image contains a conductor. Note that $\sum_i H_i$ gives the number of conductors contained in the rock tray in the enhanced Otsu's detection method. The rock tray contains the foiled rock.

Figure 4 shows the diagram of the enhanced Otsu's method. The measurements are of full-density rock sample that includes the conductive rock with 20%.

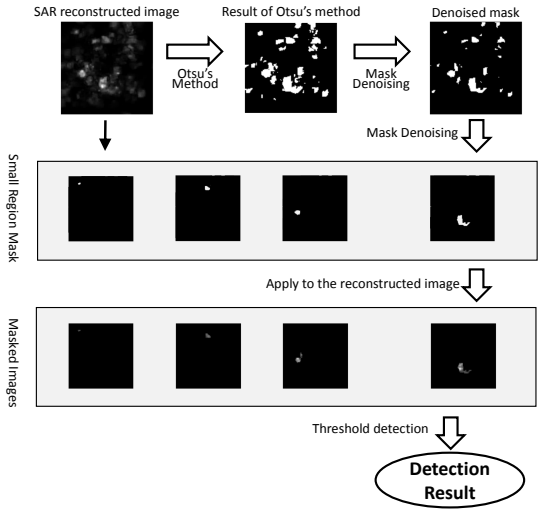

Figure 4. Intermediate images in detecting procedures of full-density without conductor by 10% measurements.

Algorithm 5 Label the Denoising Mask

$i = 1$; $j = 1$
while $\exists \tilde{B}_j = 1$ that $\tilde{B}_j \notin C_m,\ m = 1, 2, \cdots, n$ **do**
    If $\exists j < i\ : ||\tilde{B}_i - \tilde{B}_j||_2 \leqslant 2$
      Add $\tilde{B}_i$ to C_m where $\tilde{B}_j \in C_m$
    Else
      Create a new set C_{n+1} and add $\tilde{B}_i$ to C_{n+1}
      $n \leftarrow n + 1$
    End If
    $i \leftarrow i + 1$
end while
return C $= \{C_1, C_2, \cdots, C_n\}$

4. EXPERIMENTAL RESULTS

The SUTs consisted of a tray with four different arrangements or rocks, herein referred to as different rock densities. For all four cases, an image was taken with and without the presence of an additional rock covered in aluminum foil (in order to provide a scene with a high and low electromagnetic scattering contrast). These rocks were large compared to the wavelength of the microwave signal and had irregular shape. Therefore, they represent a complex scene in both the spatial and spectral domains. The distance between the radiating antenna and the surface of the SUTs was 21 mm. The scanning area was 120 mm $\times$ 120 mm, with a step size of 1 mm in both the X and Y axis. The range of frequencies was $50.0 - 75.0$ GHz with 101 equally-spaced frequencies (the measured data had dimensions of $120 \times 120 \times 101$). The probe polarization was along the X-axis.

Four different rock densities, namely: full, medium, low and lowest were used for this study. Furthermore, each rock density sample was scanned with and without the presence of the foil wrapped rock for a total of eight different samples. Photos of the studied samples are shown in Figure 5.

In all four samples, a scan was performed with the conductor and without the conductor among the rocks. A total of eight different samples were processed in this study. Photos of the samples are shown in Figure 5. From left to right: the density of samples is full, medium, low, and lowest.

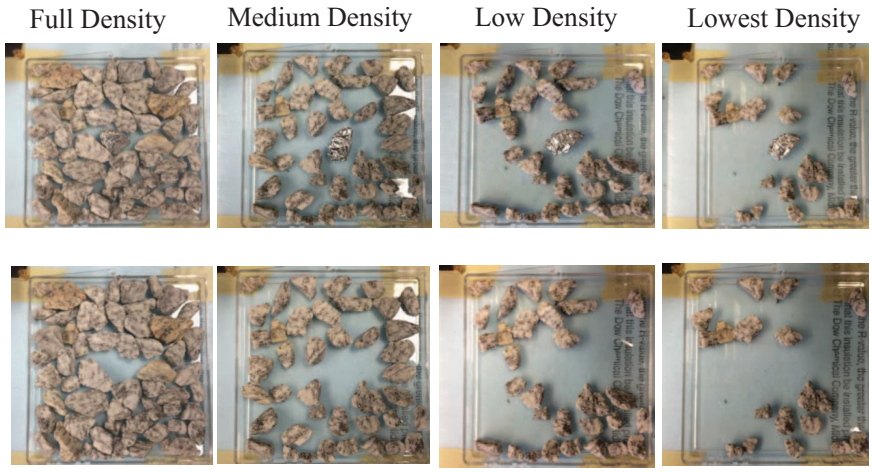

Figure 5. Rock samples applied in the microwave SAR experiment.

The rest of the experiment involves four steps:

1. Generate measurement samples on the aperture for a particular sparse-sampling rate $\rho \in [5\%, 95\%]$,
2. Reconstruct SAR images with the methods discussed above.
3. Analyze the relationship between the wavelet bases and OMP-CG reconstructions.
4. Evaluate the SAR images according to the SSIM and PSNR metrics defined in (16) and (17), respectively.

The raw measurement was randomly under-sampled to generate the sparsely-sampled data (at different sampling rates). Figure 6 shows the images reconstructed from 30% sparsely-sampled measurements with the ZF, NUFFT, CS-OMP, and CS-CG method, respectively. CS-OMP uses the identity transform, and CS-CG uses the wavelet transform with “Battle” base. "Battle" wavelet function was used to generate the CS-CG images

in this paper. Thirty-percent measurements are sufficient for CS methods to reconstruct high quality images for all kind of measurements, while the ZF and NUFFT methods are unable to reconstruct the same quality images. CS methods allow reconstruction with lower measurements as the results will later show. The last set of measurement in Figure 6 show the ground truth image with reconstructed images from 100% raw data.

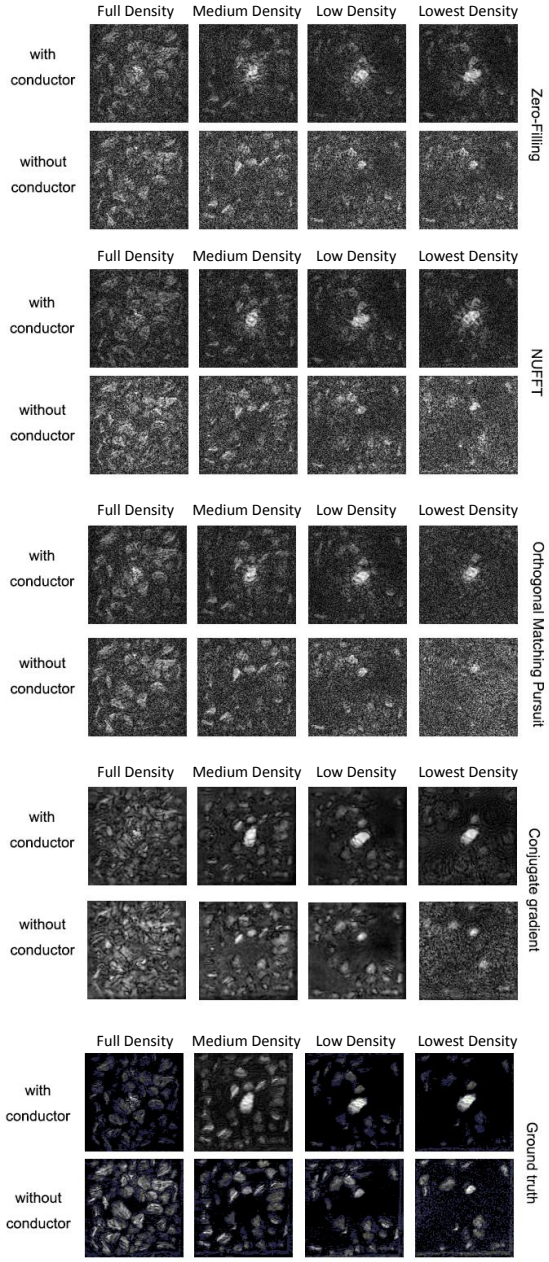

Figure 6. The reconstructions with the ZF, NUFFT, CS-OMP and CS-CG methods with a 30% sparser sampling rate.

Figure 6 shows that reconstructions created with the ZF method are difficult to identify in most cases. Based on the Nyquist theory, artifacts exist in sparsely-sampled reconstructions. Reconstructions using the NUFFT method are clearer than the ZF method in most cases, where the occurrence of artifacts is reduced and the images are much smoother. However, the rocks are still hard to identify subjectively in the low density image without the conductor present and in the lowest dense image with and without the conductor present.

Additional gain can be expected for 2-D CS reconstructions based on the above derivation that CS can reconstruct perfect images with a low sampling rate. It is observed that the edges and contrast of rocks are unambiguous compared to the ZF/NUFFT method. The reconstructions from the two CS methods are less noisy and easier to identify in most cases. Artifacts shown in ZF/NUFFT reconstructions from the limited aperture of the imaging operator are absent in CS images. Compared with samples reconstructed by the ZF/NUFFT method, results from CS methods have a higher subjective quality assessment. There are also differences between the results of CS-OMP and CS-CG. The eight samples of medium density with conductor, low density with conductor, and lowest density without conductor have higher performance with both the OMP algorithm and CG algorithm. In five other cases, the OMP algorithm performs better in full density with conductor, full density without conductor, and medium density without conductor, while the CG algorithm performs better in SSIM and PSNR metrics in the low density without conductor and lowest density without conductor.

The results clearly indicate that a sparse-sampled measurement could be reconstructed with proper methods instead of losing quality. CS works well with the high-frequency SAR measurement. The noise and artifacts have been highly reduced with the two CS methods. However, CS-OMP and CS-CG perform differently with different densities. As concluded from Figure 6, the OMP algorithm performs better with high density while the CG algorithm performs better with low density.

Different sparse-sapling rates were also used for recosntruction to illustrate their performance with various methods. The results of full density with conductor measurements and lowest density without conductor measurements using sparse-sampling rates from 5% to 100% are represented by Figure 7 and Figure 8, respectively. The sparse-sampling rate of each result is from 0.1 to 0.9 from left to right and top to bottom.

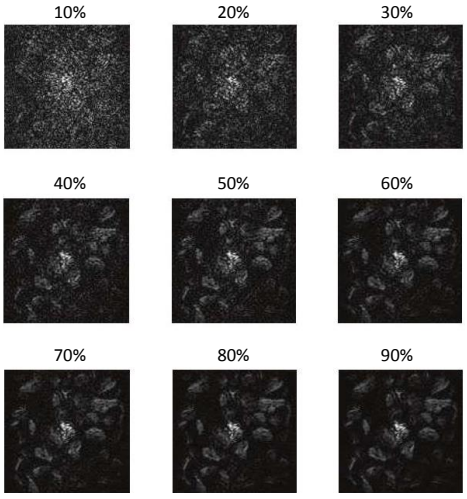

(a) ZF method.

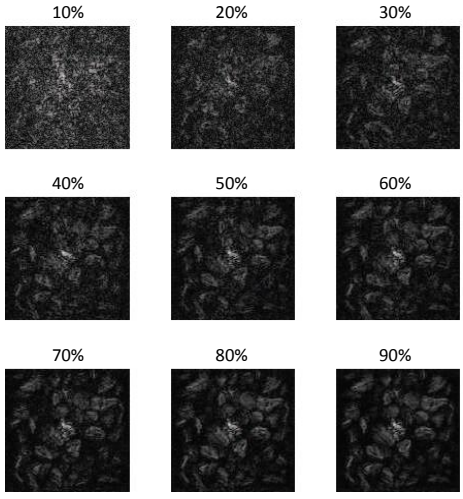

(b) NUFFT method.

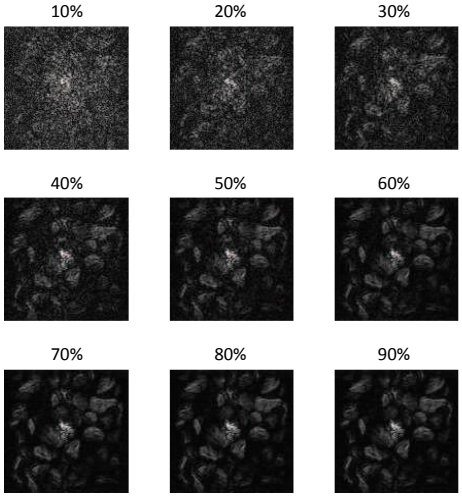

(c) CS-OMP method.

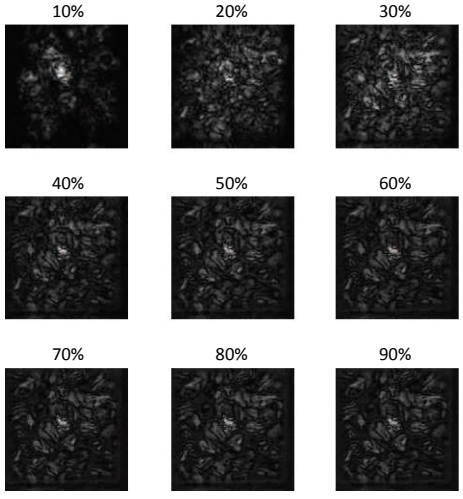

(d) CS-CG method.

Figure 7. The reconstructions of full density with conductor measurements using the ZF, NUFFT, CS-OMP, and CS-CG methods.

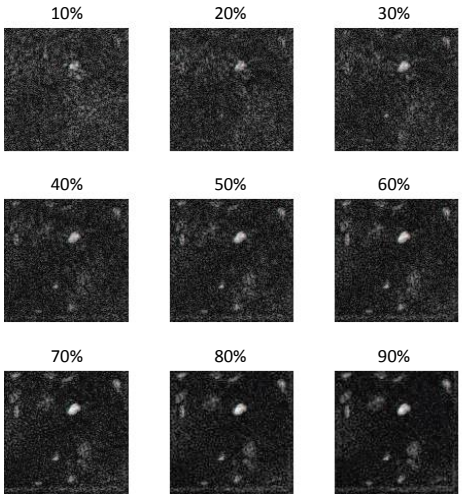

(a) ZF method.

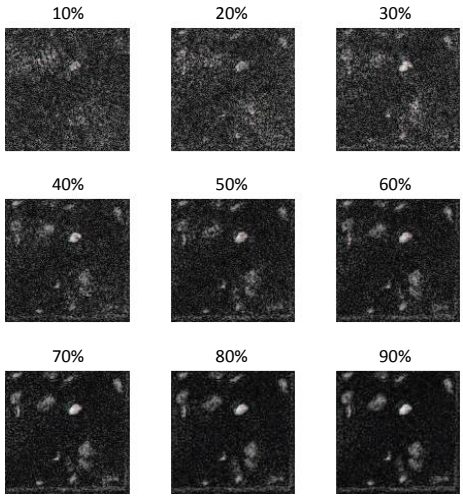

(b) NUFFT method.

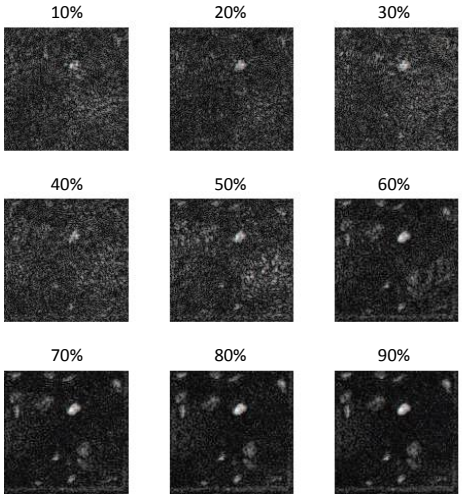

(c) CS-OMP method.

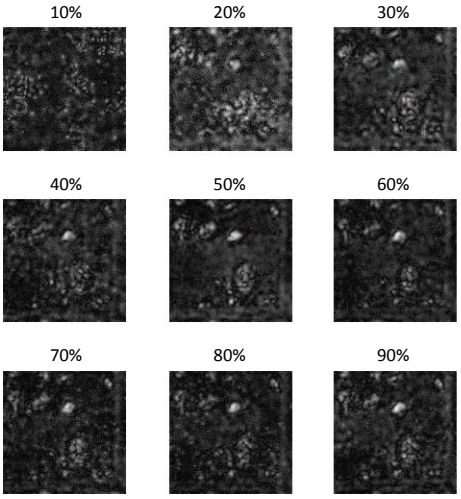

(d) CS-CG method.

Figure 8. The reconstructions of lowest density without conductor measurements using the ZF, NUFFT, CS-OMP, and CS-CG methods.

Figure 7 and Figure 8 show that the reconstructions of CS methods improve from the reconstructions using the ZF/NUFFT method. The CS-OMP and CS-CG methods reconstruct an image with fewer horizontal shadows of both the cross profiles and the circle profiles than the ZF and NUFFT methods. The images have been histogram equalized to be

clearly shown. More specifically, when the sampling rate is lower than 30%, reconstructions from the CS methods have apparent improvement. In Figure 7c, the reconstruction with only 30% measurements has fewer artifacts and the conductor is evident and identified. It is difficult to obtain useful information from the reconstructions with the same sampling rate from the ZF and NUFFT methods shown in Figure 7a and Figure 7b due to noisy and blurred images. When the sparse-sampling rate is higher than 20%, the noise and artifacts in the reconstructions are eliminated with all methods.

Conductor identification is also an exciting project in this study. From Figure 7d, a conductor can be easily identified with only a 10% sampling rate in the CS-CG method. In the CS-OMP method, a 30% sampling rate is enough for subjective identification. In the ZF and NUFFT methods, the conductor is subjectively identified when the sparse-sampling rate is higher than 50% and 70%, respectively.

To objectively assess the reconstruction quality, The SSIM and PSRN index of all reconstructions were calculated. Structural similarity (SSIM) and peak signal-to-noise ratio (PSNR) are commonly used for 2-D image quality evaluation. They are considered consistent with human eye perception. The specific form of the SSIM index between two images ($\mathbf{g}_1$ and $\mathbf{g}_0$) is defined as

$$\mathrm{SSIM}(\mathbf{g}_1, \mathbf{g}_0) = \frac{(2\mu_1\mu_0 + C_1)(2\sigma_{1,0} + C_2)}{(\mu_1^2 + \mu_0^2 + C_1)(\sigma_1^2 + \sigma_0^2 + C_2)} \tag{16}$$

where C_1 and C_2 are the auxiliary variables and (μ_1, μ_0), (σ_1^2, σ_0^2), and $\sigma_{1,0}$ are the mean, variance, and cross-covariance of the two images, respectively. The typical parameter settings $C_1 = 10^{-4}$ and $C_2 = 9 \times 10^{-4}$ are used in this study. The SSIM value is in the range of $[0, 1]$, where the SSIM is 1 if the reconstructed image is exactly the same as the ground truth image. Thus, a large SSIM index corresponds to better reconstruction quality, and vice versa.

The specific form of the PSNR index between two images ($\mathbf{g}_1$ and $\mathbf{g}_0$) is defined as

$$\begin{aligned} \text{PSNR} &= 10 \log_{10} \frac{255^2}{\text{MSE}} \\ \text{MSE} &= \frac{1}{N_{xy}} \sum_{n=1}^{N_{xy}} [\mathbf{g}_1(n) - \mathbf{g}_0(n)]^2 \end{aligned} \tag{17}$$

where $\mathbf{g}_i(n)$ is the n-th element of the image $\mathbf{g}_i, (i = 0, 1)$. Note that a large PSNR index corresponds to better reconstruction quality.

Figure 9 illustrates the averaged SSIM and PSNR between the ground truth images and the reconstructed images with sparse-sampling rate varying from 10% to 60%. From the image quality assessment, it is easier to evaluate the quality of the reconstruction objectively. CS methods have much higher assessed values in SSIM index, especially when the sampling rate is lower than 30%. In SSIM assessment, CS-CG performs much better than the other methods. With increasing sampling rate, the performance of CS-OMP grows more quickly than ZF and NUFFT. Since SSIM compares the structure of two images, the results prove that CG-CS methods have better quality overall. The images with high SSIM values are smoother with clearer edges, just as they are in subjective observation. In PSNR assessment, CS methods also perform better than ZF and NUFFT methods. CS-OMP results in a higher value, which represents less noise in reconstructions. Conclusions from the objective evaluation confirms the subjective observation.

After proving that the CS approaches could work well with the microwave SAR, the next step was to improve the reconstruction quality. One of the most valuable parts of SAR imaging is that reconstructions suppress speckle noise and simultaneously present the edges of the original image that often include features of interest. For the NDE application, the SUTs typically exhibit the nature of sparsity, but may not be acceptable in all cases. Selecting a proper sparse transform is an effective method to improve the CS accuracy and quality. Seven kinds of different wavelet transform bases were applied using the CS-

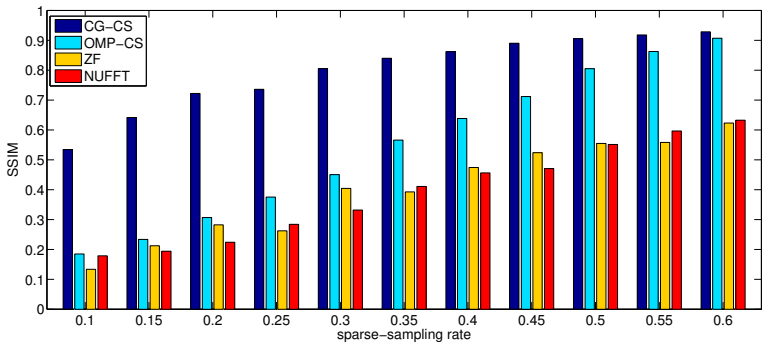

(a) SSIM.

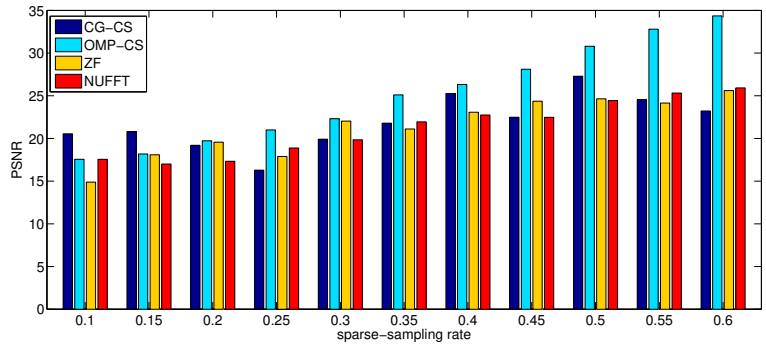

(b) PSNR.

Figure 9. (a) SSIM of the reconstructed images with reference to the 100% reconstructions. (b) PSNR of the reconstructed images with reference to the 100% reconstructions.

CG approach. Figure 10 shows the results of low density reconstructions with conductor measurements. From left to right are 5% to 35% sparse-sampling rates. From top to bottom are different reconstruction methods. (Daub = Daubechies, Vaidy= Vaidyanathan).

Figure 10 illustrates the comparison of the reconstructed images with a 5% to 35% sparse-sampling rate using the CS-CG methods with different wavelet bases. Figure 11 shows objective quality curves. In the subjective evaluation, the qualities of the seven types of reconstructions are similar to the lowest density case with conductor. When the sparse-sampling rate is 5%, SAR images are not correctly reconstructed. As there is less information that can be used for reconstruction, images are too blurry to extract useful information, especially with the simplest “Haar” basis, where the conductor cannot be recognized at all. Among the 5% reconstructions, nearly all the bases could correctly show the conductor,

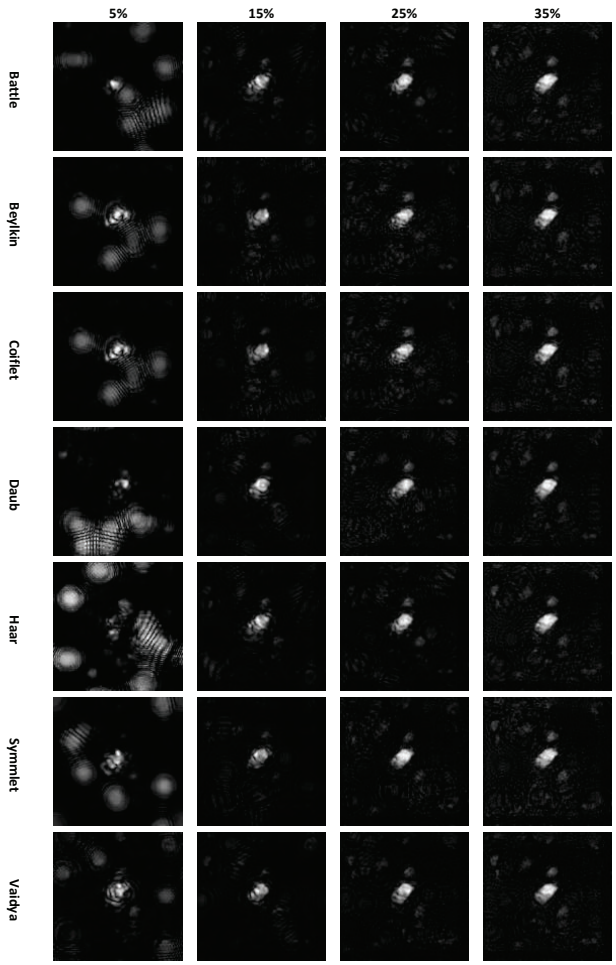

Figure 10. Reconstructions by CS-CG method of different wavelet bases of the lowest density SUT with conductor.

which is reflected as a much brighter region in the reconstructions. In conclusion, only 5% data is necessary to make simple identifications. Quality of the reconstructions is increased appreciably with a sparse-sampling rate higher than 15%. Artifacts are still easy to identify in 15% reconstructions. When the sampling rate increased to 25%, aliasing was reduced, and surrounding rocks that did not contain the alumina became clearer. Until the sparse sampling rate is higher than or equal to 35%, reconstructions of all bases have extremely high similarity with the fully sampled reconstructions. The conductor and surrounding rocks have a clear edge and good contrast in all reconstructions.

By comparing reconstructions from the CS-CG method, it is clear that not all of the wavelet bases are satisfied with the SAR measurement. Subjectively, reconstructions from the CS-CG method applied with the proposed wavelet bases performed noticeably better than the CS-OMP, especially when the sparse-sampling rate was lower. Objective evaluations of each image are shown in Figure 11.

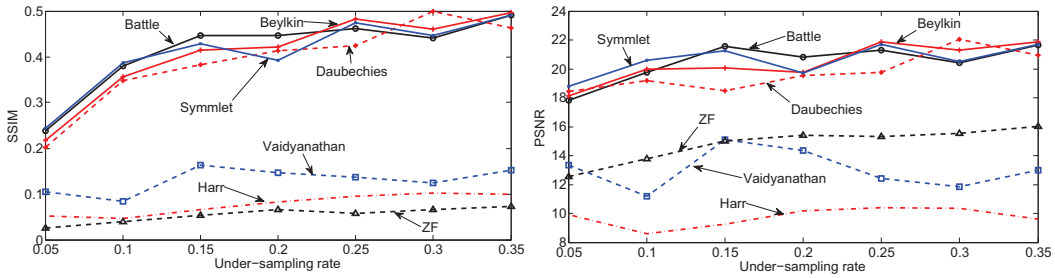

(a) SSIM (b) PSNR

Figure 11. (a) SSIM of the reconstructed images with reference to the 35% reconstructions. (b) PSNR of the reconstructed images with reference to the 35% reconstructions.

After comparing the results of the eight CS sparse representation domains, it is concluded that different types of sparse domains lead to different qualities of reconstruction. With the proper sparse transform, it is possible to reconstruct high-frequency SAR images with a sparse-sampling rate as low as 15%.

A detecting algorithm is then applied to the low-sampling rate reconstructions. In this study, the intensity of reconstructions was normalized to $[0, 1]$. The normalization images can verify the threshold's detecting method. All detecting samples from CG-CS method have been reconstructed by the CG method with the Identity base. In each density, the SAR images were reconstructed from 1% to 20% sparse sampling rate with a 1% as step size. In each percentage, 30 sample measurements were randomly simulated and reconstructed with the CG-CS and ZF method, respectively.

Setting a global threshold for all the reconstructions is difficult, so applying an adaptive thresholding method is an attractive alternative. Otsu's thresholding method is an efficient adaptive method when the image is smooth and clear. Unfortunately Otsu's method will fail in segmentation when the image is noisy because the region is so small.

To solve this problem, Otsu's thresholding image was processed with the denoising method introduced above. There are four types of detecting results (These definitions are not totally as same as in the normal medical image): 1. Detected a conductor in the measurements with conductor, denoted as true positive (TP); 2. Did not detect a conductor in the measurements with conductor, denoted as true negative (TN); 3. Detected a conductor in the measurements without conductor, denoted as false positive (TP); 4. Did not detect out a conductor in the measurements without conductor, denoted as false negative (FN). We use (18) to compute the accuracy of detection ϱ_d:

$$\varrho_d = \frac{\sum(TP + FN)}{\sum(TP + TN + FP + FN)}; \tag{18}$$

A high value of ϱ_d denotes that the method could successfully detect conductor from the measurements with conductor and would not detect conductor from the measurements without conductor. With the robust and accurate image detection method, it is possible to measure very low-sampled data to check whether there is conductor or not.

To accelerate the CG-CS reconstruction in this detecting project, only the first half-frequency slides were calculated in reconstruction. We used the "Identity' matrix as the sparse matrix instead of wavelet bases to reduce the complexity of reconstruction. The computational cost has been highly reduced, but the image quality may also be lowered. Figure 12 shows the rates of four kinds of results of the full-density measurements reconstructed with the CS and ZF methods, respectively.

It can be observed from Figure 12a that true positive (TP) rate and false negative (FN) rate increase rapidly with the sampling rate. The enhanced Otsu's thresholding method is proven to be efficient in SAR image detection. Only 6% measurement is needed to detect whether there is conductor or not and the TP rate and the FN rate are similar. Overall, the method is independent of the measurements and the accuracy was not affected by conductor. Shown in Figure 12b, the TP rate keeps near 1, which denotes that the enhanced Otsu's method could correctly detect conductor from measurements with conductor from

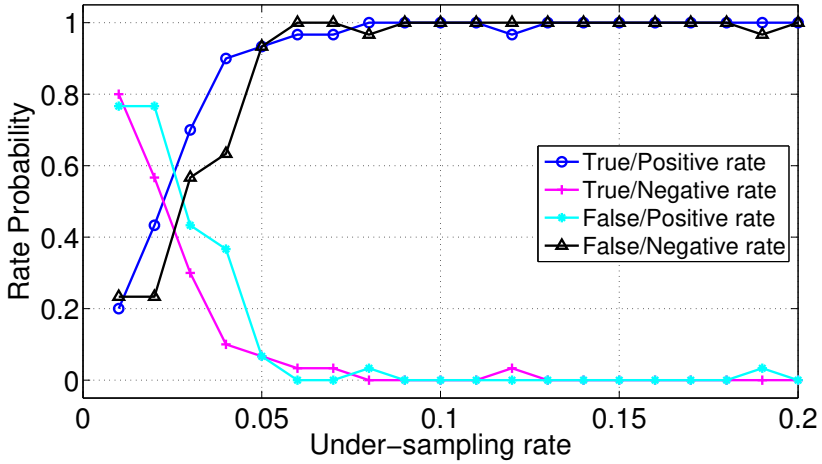

(a) Compressed Sensing

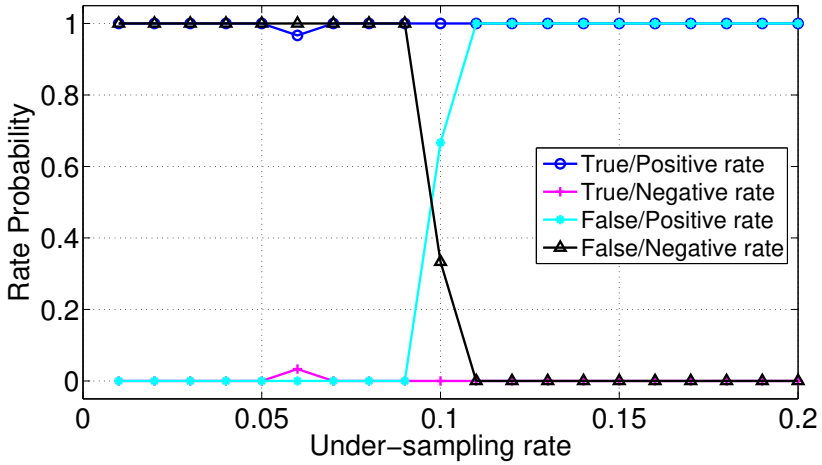

(b) Zero Filling

Figure 12. The rate of true positive, true negative, false positive, and false negative of detecting results with full-density measurements.

ZF reconstructions. However, the FN rate will reduce to 0 when the sampling rate is higher than 1%, which denotes that this method fails for the measurements without conductor from ZF reconstructions. It emphasizes the significance of the CS method in the SAR image detecting method, while ZF method may misdetect conductor from measurements without conductor.

The accuracy rate of all four density measurements was then calculated. The accuracy rate is defined in (18) and shown in Figure 13. The results of the CG-CS method and the ZF method with the various densities and thresholds of the conductor reflective rate were compared. Figure 13a shows the results of the CG-CS reconstructions when the threshold of reflective rate is set to 0.8. The advanced detection method fits all four density measurements. The accuracy increases very fast when the sampling rate is lower than 6%. The accuracy rate stabilizes at levels higher than 90% when the sampling rate is higher than 10%. In our study, the reconstruction has been highly simplified to accelerate the computation. As a result, the unsimplified complete procedures can further improve the detection accuracy of the reconstruction. As shown in Figure 13b, Figure 13c, and Figure 13d, the compressed sensing method is much more stable than the ZF method. The accuracy rate of CS reconstructions has less fluctuation with various densities and parameters.

5. CONCLUSION

Microwave SAR images reconstructed with the ZF, NUFFT, OMP-CS, and CG-CS methods have been compared in terms of their reconstructive qualities through experimental studies of different SUTs and sparse-sampling rates. The experimental results have demonstrated that the OMP-CS and CG-CS methods perform significantly better than the ZF and NUFFT denoising methods for both SSIM and PSNR when the sparse-sampling rates are lower than 50%. The performance of the CG-CS method depends heavily on the choice of the sparse representation matrix. When the matrix is selected properly, the CG-CS method showed larger gain over the other three methods in low sparse-sampling rates less than 30%. We also introduced a conductor detection method for sparse SAR measurements. The current accuracy of our conductor detection method is higher than 90% with less than 10% measurements.

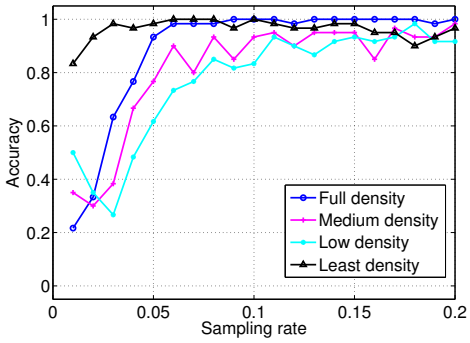

(a) Compressed Sensing, Threshold = 0.80

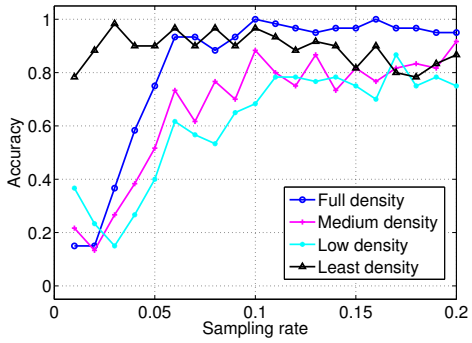

(b) Compressed Sensing, Threshold = 0.75

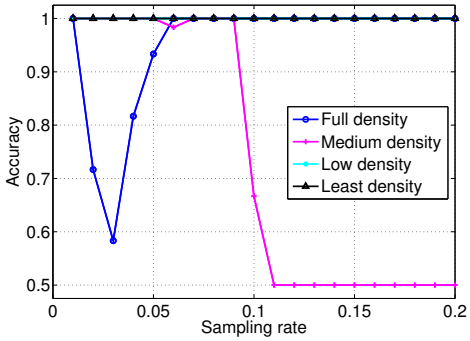

(c) Zero Filling, Threshold = 0.80

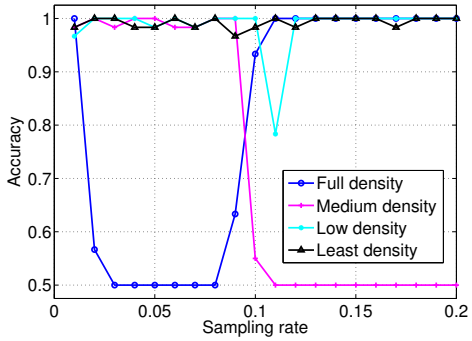

(d) Zero Filling, Threshold = 0.75

Figure 13. The accuracy of detection with CG-CS and ZF methods.

ACKNOWLEDGMENTS

The work was supported in part by the US Department of Defense STTR project W31P4Q-14-C-0146 and the Intelligent Systems Center of Missouri University of Science and Technology.

REFERENCES

[1] S. Kharkovsky and R. Zoughi, "Microwave and millimeter wave nondestructive testing and evaluation — Overview and recent advances," *IEEE Instrum. Meas. Mag.*, vol. 10, no. 2, pp. 26–38, Feb. 2007.

[2] J. T. Case, M. T. Ghasr, and R. Zoughi, "Optimum 2—D nonuniform spatial sampling for microwave SAR-based NDE imaging systems," *IEEE Trans. Instrum. Meas*, vol. 61, no. 11, pp. 3072–3083, Nov. 2012.

[3] M. Soumekh, *Synthetic aperture radar signal processing*. New York: Wiley, 1999.

[4] M. T. Ghasr, J. T. Case, and R. Zoughi, "Novel reflectometer for millimeter-wave 3-d holographic imaging," *IEEE Trans. Instrum. Meas.*, vol. 63, no. 5, pp. 1328–1336, Jan. 2014.

[5] S. G. Chang, B. Yu, and M. Vetterli, "Adaptive wavelet thresholding for image denoising and compression," *IEEE Trans. Image Process.*, vol. 9, no. 9, pp. 1532–1546, Sep. 2000.

[6] Q. H. Liu and N. Nguyen, "An accurate algorithm for nonuniform fast fourier transforms (nufft's)," *IEEE Microw. and Guided Wave Lett.*, vol. 8, no. 1, pp. 18–20, Jan 1998.

[7] C. D. Austin, E. Ertin, and R. L. Moses, "Sparse signal methods for 3-D radar imaging," *IEEE J. Sel. Topics Signal Process.*, vol. 5, no. 3, pp. 408–423, Jun. 2011.

[8] Z. Yang and Y. R. Zheng, "A comparative study of compressed sensing approaches for 3-D synthetic aperture radar image reconstruction," *Elsevier Digital Signal Process.*, vol. 32, pp. 24–33, May 2014.

[9] H. Kajbaf, J. T. Case, Z. Yang, and Y. R. Zheng, "Compressed sensing for sar-based wideband three-dimensional microwave imaging system using non-uniform fast Fourier transform," *IET. Radar, Sonar & Navigation*, vol. 7, no. 6, pp. 658–670, May. 2013.

[10] M. Elad, "Optimized projections for compressed sensing," *IEEE Trans. Signal Process.*, vol. 55, no. 12, pp. 5695–5702, Dec. 2007.

[11] M. A. T. Figueiredo, J. M. Bioucas-Dias, and R. D. Nowak, "Majorization-minimization algorithms for wavelet-based image restoration," *IEEE Trans. on Image Process.*, vol. 16, no. 12, pp. 2980–2991, Dec 2007.

[12] M. Lustig, D. L. Donoho, and J. M. Pauly, "Sparse MRI: The application of compressed sensing for rapid MR imaging," *Magnetic Resonance in Medicine*, vol. 58, no. 6, pp. 1182–1195, Oct. 2007.

[13] R. C. Gonzalez and R. E. Woods, *Digital image processing,* 3^{rd} *ed.* Addison-Wesley, 2008.

[14] A. S. Khwaja and J. Ma, "Applications of compressed sensing for SAR moving-target velocity estimation and image compression," *IEEE Trans. Instrum. Meas.*, vol. 60, no. 8, pp. 2848–2860, Aug. 2011.

[15] J. Ma, "Improved iterative curvelet thresholding for compressed sensing and measurement," *IEEE Trans. Instrum. Meas.*, vol. 60, no. 1, pp. 126–136, Jan. 2011.

[16] A. Ravelomanantsoa, H. Rabah, and A. Rouane, "Compressed sensing: A simple deterministic measurement matrix and a fast recovery algorithm," *IEEE Trans. Instrum. Meas.*, vol. 64, no. 12, pp. 3405–3413, Dec. 2015.

[17] T. Edeler, K. Ohliger, S. Hussmann, and A. Mertins, "Super-resolution model for a compressed-sensing measurement setup," *IEEE Trans. Instrum. Meas.*, vol. 61, no. 5, pp. 1140–1148, May. 2012.

[18] X. Yang, Y. R. Zheng, M. T. Ghasr, K. M. Donnell, and R. Zoughi, "Microwave synthetic aperture radar imaging using sparse measurement," in *Instrum. Meas. Conf. Proc. (I2MTC), 2016 IEEE International*. IEEE, Jul. 2016, pp. 1–5.

[19] Y. Tsaig and D. L. Donoho, "Extensions of compressed sensing," *Signal Process.*, vol. 86, no. 3, pp. 549–571, Mar. 2006.

[20] Z. Wang, A. C. Bovik, H. R. Sheikh, and E. P. Simoncelli, "Image quality assessment: from error visibility to structural similarity," *IEEE Trans. Image Process.*, vol. 13, no. 4, pp. 600–612, Apr. 2004.

[21] H. S. Prashanth, H. L. Shashidhara, and M. K. N. Balasubramanya, "Image scaling comparison using universal image quality index," in *2009 International Conference on Advances in Computing, Control, and Telecommunication Technologies*, Dec 2009, pp. 859–863.

[22] D. R. Thompson, D. S. Wettergreen, and F. J. C. Peralta, "Autonomous science during large-scale robotic survey," *Journal of Field Robotics*, vol. 28, no. 4, pp. 542–564, Jun. 2011.

[23] L. Li, W. Huang, I. Gu, and Q. Tian, "Statistical modeling of complex backgrounds for foreground object detection," *IEEE Trans. on Image Process.*, vol. 13, no. 11, pp. 1459–1472, Nov. 2004.

[24] A. S. Milman, "SAR imaging by ω- κ migration," *Int. J. of Remote Sensing*, vol. 14, no. 10, pp. 1965–1979, May. 1993.

[25] F. P. Preparata and M. Shamos, *Computational geometry: an introduction*. Springer Science & Business Media, 2012.

[26] J. Tropp, A. C. Gilbert *et al.*, "Signal recovery from random measurements via orthogonal matching pursuit," *IEEE Trans. Inf. Theory*, vol. 53, no. 12, pp. 4655–4666, Dec. 2007.

[27] V. Gor, E. Mjolsness, R. Manduchi, R. Castano, and R. Anderson, "Autonomous rock detection for mars terrain," in *AIAA Space Conf. and Exposition*, 2001, p. 4597.

[28] G. C. Feng and P. C. Yuen, "Multi-cues eye detection on gray intensity image," *Pattern recognition*, vol. 34, no. 5, pp. 1033–1046, May, 2001.

III. AN IMAGE DENOISING METHOD FOR SAR IMAGES WITH LOW-SAMPLING MEASUREMENTS

Xiahan Yang, Yahong Rosa Zheng

Department of Electrical & Computer Engineering

Missouri University of Science and Technology

Rolla, Missouri 65409–0040

Tel: 573–341–6622, Fax: 573–341–4115

Email: {xy6v4, zhengyr} @mst.edu

ABSTRACT

In this study, an image denoising method for the synthetic aperture radar (SAR) images is proposed. When reconstructed from low-sampling-rate measurements using a compressed sensing (CS) based method, the reconstructions still suffer from noise and aliasing for the sampling rate is much lower than the Nyquist sampling rate (15%-25%). To in future improve the reconstruction, we proposed an imaging denoising method for CS-based reconstructed SAR image. In this proposed denoising method, the pending SAR image is treated as a level set function. We design a step curvature flow function using which the aliasing and noise are eliminated and the clarity of objects of interest in the SAR images are enhanced. Simulation and experimental results illustrated that only a 20% measurement is necessary in the SAR experiment to identify the objects of interest with the proposed method.

Keywords: Synthetic Aperture Radar, Image Denoising, Low-Sampling Reconstruction

1. INTRODUCTION

Synthetic Aperture Radar (SAR) is a well-established and widely-fielded technique for reconstructing images with higher spatial resolution stationary aperture and target [1]. Microwave and millimeter-wave imaging techniques applied in SAR system have shown tremendous potential in applications related to biomedical, security, and nondestructive evaluation (NDE) [2, 3, 4, 5]. The traditional high-resolution SAR images require a large sampling measurement. We have proposed a compressed sensing (CS) based method for a SAR system that can reduce the 60%-70% measurement overhead needed by a SAR imager [6]. Saving measurements sampling could help in saving time and expense, which is important in SAR applications. In this study, we focus on very low-sampling measurement overheads (15%-20%) for SAR image reconstruction. To improve the quality of these reconstructions, we present an image denoising and enhancement method as a post-processing option for reconstruction.

The method presented in this study is proposed for enhancing the SAR images which are reconstructed with the CS-based method requiring a very low-sampling measurement. According to the Nyquist sampling theory, reconstruction will be aliased when the sampling rate is lower than the Nyquist sampling rate. Dr. Donoho has proved in his paper that when the restricted isometry property (RIP) condition is satisfied, the reconstruction of the entire signal based on a low-sampling rate is highly probable [7]. Limited by computational error and a very low-sampling rate, the quality of the reconstructions are not as good as the fully-sampled reconstruction in SAR experiment (which suffer from the noise and aliasing as well). We propose an image denoising method to improve the quality of SAR reconstruction.

The essential idea in image denoising is to filter noise present in the image, without sacrificing the useful detail. Meanwhile, image enhancement focuses on preferentially highlighting certain image features and works synchronously with image denoising [8]. These procedures are precursors to many low-level vision procedures such as edge finding,

shape segmentation, and shape representation. In this study, we present a method developed from the geometric heat equation to denoise and enhance the SAR images reconstructed based on a low-sampling rate. The idea is based on the level set method, which evolutes the shape curve based on the curvature [9]. This method offers several key benefits. First, it contains only three outer parameters, which in most cases are fixed. Second, the iteration scheme automatically picks the stopping criteria. Third, the method is one of the fastest possible methods based on image denoising. To evaluate the performance of the method, we applied a non-reference image quality evaluation method [10]. Because our method is effective in denoising and enhancing the noised images and subjectively improving their quality, the images have been enhanced; notably, several referenced-image-quality methods cannot correctly detect the change. The estimated quality values from the referenced-image-quality assessments are not accurate in this application.

2. ALGORITHM

2.1. Level Set Function for Image Denoising. Consider a closed moving curve $\Gamma(t)$ on a plane. Let $\Phi(t)$ be the region that $\Gamma(t)$ encloses. The level set function associated with $\Phi(t)$ is $\phi(\mathbf{x}, t)$ is defined as [11]

$$\begin{cases} \phi(\mathbf{x}, t) < 0, & \text{in } \Phi(t) \\ \phi(\mathbf{x}, t) = 0, & \text{on } \Gamma(t) \\ \phi(\mathbf{x}, t) > 0, & \text{otherwise} \end{cases} \tag{1}$$

where $\mathbf{x} = \{x, y\} \in R^2$ is the spatial coordinates on the plane, and $t \in R^+$ is the time index. Conversely, $\Gamma(t)$ can be located by finding the zero level set of ϕ as: $\Gamma(t) = \{\mathbf{x} : \phi(\mathbf{x}, t) = 0\}$. Therefore, moving the interface is equivalent to updating ϕ. Suppose $\mathbf{x}(t)$ is a particle trajectory on the interface $\Gamma(t)$ moving with velocity $\tilde{u} = \partial \mathbf{x}(t)/\partial t$, then we have:

$$\partial \phi(\mathbf{x}, t)/\partial t + \tilde{u} \cdot \nabla \phi = 0. \tag{2}$$

It is obvious that the only vertical component of $\tilde{u}$ can move Γ, and Eq. (2) can be rewritten as:

$$\partial\phi(\mathbf{x}, t)/\partial t + u_v \cdot |\nabla\phi| = 0 \tag{3}$$

In Figure 1, the relationships in the level set method are shown.

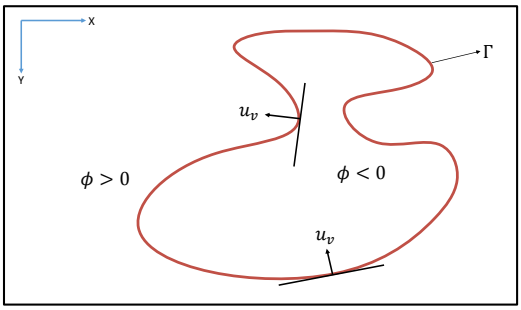

Figure 1. Zero contour of ϕ representing the front Γ and the velocity vertical component u_v.

Taking derivative with respect to t on both sides of Eq. (3)

$$\frac{\partial\phi(t)}{\partial t} + |\nabla u| = 0 \tag{4}$$

where Eq. (4) is an Hamilton-Jacobi equation. To solve this kind of problem, Osher and Sethian outline the importance of upwind methods for Hamilton-Jacobi equations in level set applications [9].

Now, let us consider the case when the normal velocity is $\tilde{u} = -\kappa$ where κ is the mean curvature. The relationship between the mean curvature and the ϕ is: $\kappa = \nabla_s \cdot n$, where ∇_s is the surface divergence and n is the outward drawn normal $n = \frac{\nabla\phi}{|\nabla\phi|}$. Since $\nabla_s = \nabla - n\partial_n = \nabla$; then, $\kappa = \nabla \cdot n$, where ∇ is the usual divergence operator. Therefore the mean curvature can be expressed as:

$$\kappa = \nabla \cdot \left(\frac{\nabla\phi}{|\nabla\phi|}\right) \tag{5}$$

where $\nabla()$ is the gradient of the image and the divergence $\nabla \cdot ()$ is an operator that produces a scalar measure of a vector field's tendency to originate from or converge upon a given point.

The level set equation for motion by mean curvature is:

$$\frac{\partial \phi}{\partial t} - \kappa |\nabla \phi| = 0 \tag{6}$$

It has been proven in [9] that if the $\phi(\mathbf{x}, t)$ is the evolution with $-\kappa$, then $\lim_{t \to \infty} \Gamma(t) = \varnothing$. In the image domain, it can be expressed as a simple curve will eliminate if it is evolving with $-\kappa$. This is the basic idea for the level set method in an image denoising application. The noise will reduce with evolution. The basic iteration of a level set method in image denoising application can be expressed as:

$$\phi(\mathbf{x}, t+1) = \phi(t) - k \cdot \kappa |\nabla \phi| \tag{7}$$

where the step size k is related to the size of the image.

In the image denoising application, the initial level set function is equal to the image intensity matrix: $\phi(\mathbf{x}, 0) = I(\mathbf{x})$. In the image domain, the gradient of a scalar field g is defined as:

$$\nabla g = x \partial g / \partial x + y \partial g / \partial y \tag{8}$$

where x,y are the unit vectors of x and y direction, respectively.

The divergence of a vector field $\mathbf{F} \in \mathbf{R^2}$ is defined as:

$$\nabla \cdot \mathbf{F} = \partial F_x / \partial x + \partial F_y / \partial y \tag{9}$$

The unit normal vector $\frac{\nabla \phi}{|\nabla \phi|}$ in Eq. (5) can be expressed in the image domain as:

$$\frac{\nabla\phi}{|\nabla\phi|} = \frac{x \cdot \phi_x + y \cdot \phi_y}{\sqrt{\phi_x^2 + \phi_y^2}} \tag{10}$$

where $\phi_x = \partial\phi/\partial x$, $\phi_y = \partial\phi/\partial y$.

With Eq. (8), Eq. (9), Eq. (10), the curvature κ can be expressed as:

$$\begin{aligned} \kappa &= \nabla \cdot \left(\frac{\nabla\phi}{|\nabla\phi|}\right) \\ &= \frac{\phi_{xx}\phi_y^2 + \phi_{yy}\phi_x^2 - 2\phi_x\phi_y\phi_{xy}}{(\phi_x^2 + \phi_y^2)^{3/2}} \end{aligned} \tag{11}$$

where $\phi_x = \partial\phi/\partial x$, $\phi_y = \partial\phi/\partial y$, $\phi_{xx} = \partial^2\phi/\partial x^2$, $\phi_{yy} = \partial^2\phi/\partial y^2$, and $\phi_{xy} = \partial^2\phi/\partial x\partial y$.

In an image denoising application, the mean curvature method based on Eq. (7) is the simplest method. In this method, the “mean curvature" for each pixel is calculated; then, evolute images with the “mean curvature" matrix, whose size is the same as that of the pending images, are created. Based on the mean curvature, the shapes will be eliminated to reach the target of denoising, as described previously. Because the noise areas are much smaller than the object areas of interest, a denoised image can be obtained from this mean curvature method. However, in most cases, the performance of the simplest method is not satisfactory. Many different evolution methods have been proposed to address different situations. [8, 11, 12, 13, 14, 15]. Notably, all the methods can be summarized in this formula:

$$\phi(\mathbf{x}, t+1) = \phi(\mathbf{x}, t) - k \cdot F(\kappa, \phi)|\nabla\phi| \tag{12}$$

where we named $F(\kappa, \phi)$ as the curvature flow function. This function expresses the evolution of the image and replaces the mean curvature κ in the mean curvature method.

The method proposed in this study is a new curvature flow function with two steps especially designed for denoising and enhancing the SAR images reconstructed from low-sampling measurements.

2.2. Our Method for SAR Image. In this study, we solve the problem of denoised SAR images reconstructed based on low-sampling measurements by using the CS-method. There are two key properties for these reconstructions. 1) The image is gray-scale while the histogram of the image is discrete. The SAR image represents the reflection rate of different objects within a specific area that satisfy this condition; 2) The image reconstructed from low-sampling measurement is filled using aliasing, where the interested object may not have a clear boundary and shape. In this project, we design the curvature flow function based on these two properties [6].

This design method is developed from two previous methods [8, 11]. In this study, we take the advantage of both the methods and propose a more effective method for enhancing the SAR images that have aliasing. A non-reference image quality evaluation method in [10] has been applied to set the thresholds in our algorithm. In our algorithm, the threshold and adaption to different SAR sample cases can be automatically set. The curvature flow function designed for SAR is as follows:

$$F(\kappa, \phi) = \begin{cases} G(\kappa), & \exists t,\ \delta_Q(t) \leqslant Q_{threshold} \\ c(\phi) \cdot \kappa, & \text{otherwise} \end{cases} \tag{13}$$

where $\delta_Q = Q(t) - Q(t-1)$ and $Q(t)$ is the non-reference image quality in t time. $G(\kappa) = \alpha\kappa + (1-\alpha)\kappa_{min/max}$ is developed from the min/max curvature. The min/max curvature flow function is defined as:

$$\kappa_{min/max} = \begin{cases} \min(\kappa, 0), & (\phi(\mathbf{x})) < 0 \\ \max(\kappa, 0), & \text{otherwise} \end{cases} \tag{14}$$

and the cutoff function $c(\phi)$ is defined as:

$$c(\phi) = \begin{cases} 1, & |\phi| \leqslant \beta \\ C(\phi), & \beta \leqslant |\phi| < \gamma \\ 0, & |\phi| > \gamma \end{cases} \tag{15}$$

where $C(\phi) = (|\phi| - \gamma)^2(2|\phi| + \gamma - 3\beta)/(\gamma - \beta)^2$, γ and β are proportional with the mean of the image intensity:

$$\begin{cases} \beta = c_\rho E\{\phi'(t)\} \\ \gamma = (1 - c_\rho)E\{\phi'(t)\} \end{cases} \tag{16}$$

where the range parameter c_ρ is less than 0.5 and greater than 0. We applied the expectation of normalized images $E\{\phi'\}$ to accumulated β and γ.

In our method, the images evolute based on the mean curvature with an auxiliary cutoff function, till the quality of improvement reaches the threshold. The auxiliary cutoff function $c(\phi)$ is applied to protect the objects of interest on an image while maintaining its shape and size during evolution, which will help in merging the object of interest. As the pending images are filled with aliasing, function $c(\phi)$ will merge the near small pixels which have a high probability of belonging to an entire larger object; using this method will not affect the farther pixels. Meanwhile, the larger object evolutes in a smaller area that will be protected from blurring or eliminating. When the δ_Q was less than the threshold (which means c has less improvement) and the pending images were entire, we applied the second curvature flow function. This approach is used to eliminate the remaining noised pixels.

When the improvement by the first step was no longer significant, we applied the second step curvature flow function which is based on the min/max method[8]. The fundamental idea in min/max method is like the simplest problem, namely, the evolution of a curve under its curvature. The image motion is based on either $\min(\kappa, 0)$ or $\max(\kappa, 0)$. When $F(\kappa) = \min(\kappa, 0)$, it preserves some of the structure of the curve; however, when

$F(\kappa) = \max(\kappa, 0)$, it completely diffuses away the noise pixels. The loop of this algorithm is proportional to the size of the image. In our method, we add a part of mean curvature $\alpha\kappa$ to ensure the evolution.

3. RESULTS

3.1. Simulation. We first examine the method with simulated images as shown in Figure 2, where a phantom with 256×256 pixels was added with different levels of white noise to simulate the aliasing in the low-sampled reconstructions. The signal-to-noise ratio (SNR) varied from 5 dB to 20 dB.

In Figure 2, when the noise level is low, namely the SNR is larger than 15 dB, our method can reduce most noise pixels and reconstruct clear and smooth images with apparent edges and shapes. When the SNR rate is less than 10 dB, our method also reduces most noise pixels. Though the reconstructions still have a few noise pixels, the shapes and edges are clear and apparent.

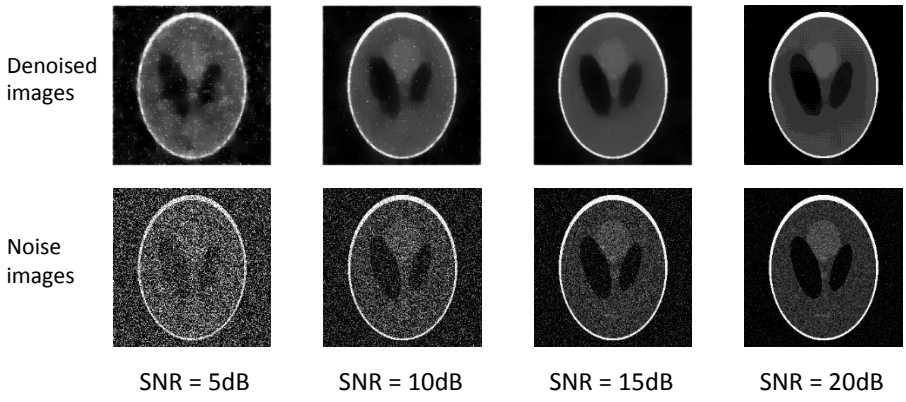

Figure 2. Reconstruction of simulated noised images with different SNR using our method.

3.2. SAR Images. In Figure 3, the photos of the rock samples applied in our applications and the reconstructions from the fully-sampled measurements are shown. There are four different samples, classified based on their different rock density. We placed

a conductor in the middle in each sample. The conductor is a rock with alumina that has a higher reflection coefficient compared to the neighboring normal rocks. In the reconstruction, the area of the conductor is much brighter than the other areas.

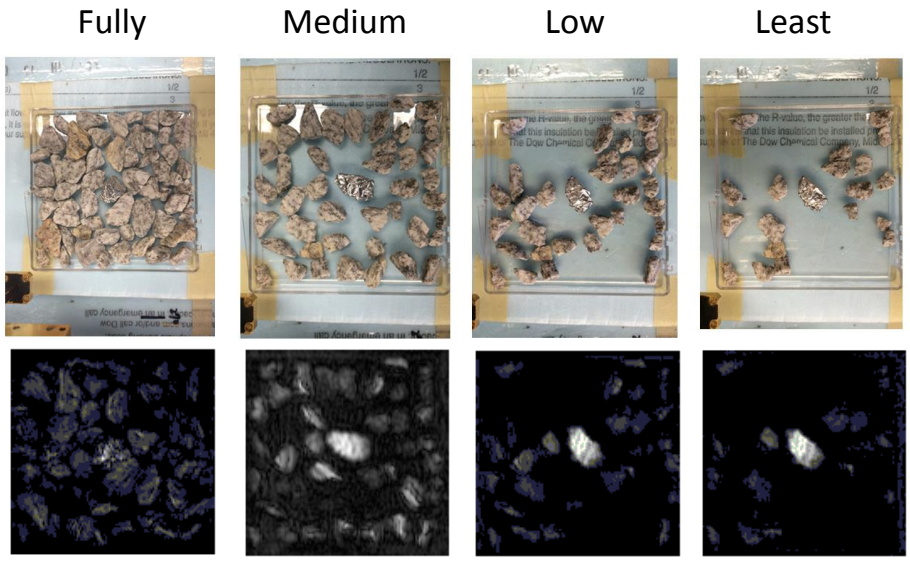

Figure 3. Photos and fully-sampled reconstructions of rock systems under test (SUTs) with different densities.

Consider now the SAR reconstructions from low-sampling rate using the CS-based method, which is shown in Figure 4. In this application, we set $Q_{threshold} = 0.007$, $c_\rho = 0.2$, $\alpha = 0.2$ in our denoised method. These three parameters can be applied to all different rock cases. This shows that our method is robust and adaptive. Here we only use 15% to 30% measurements when using the CS-based method to reconstruct and image, as we introduced in [6]. We used the denoised method proposed in this paper to improve the quality of the reconstruction.

Figure 4 illustrates reconstructions from different methods, where a) is the full density SUT with 15% sampling rate before denoising; b) is the medium density SUT with 20% sampling rate before denoising; c) is the low density SUT with 25% sampling rate before denoising; d) is the least density SUT with 30% sampling rate before denoising; e) is

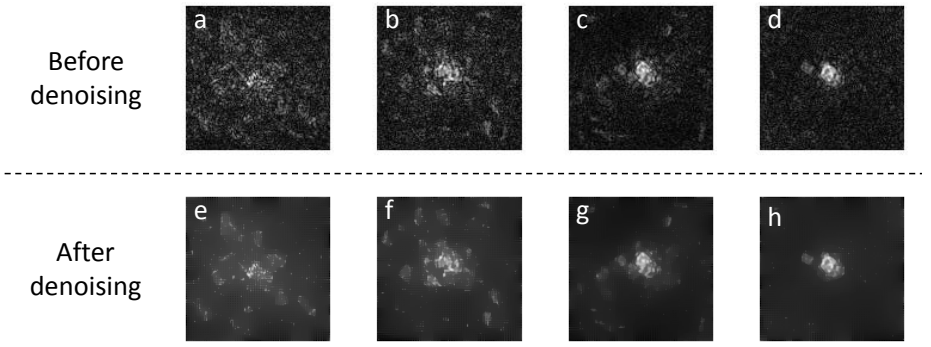

Figure 4. The low-sampling reconstructions with and without the denoising method.

the full density SUT with 15% sampling rate after denoising; f) is the medium density SUT with 20% sampling rate after denoising; g) is the low density SUT with 25% sampling rate after denoising; and h) is the least density SUT with 30% sampling rate after denoising.

In Figure 4, the reconstructions with the sampling rate lower than 30% is shown. When the sampling rate is lower or equal to 20%, shown in a) and b), the noise and aliasing are obvious in this reconstruction. The rocks cannot be clearly identified subjectively. With the denoising method, we can clearly identify each rock subjectively, while the edges are not clear and the images are a little blurred, as shown in e) and f). When the sampling rate is higher than or equal to 25%, the denoised method can perfectly eliminate the noise and aliasing and the rocks are apparent with clear edges and shapes, which can be seen in c), d), h), and g).

As a future test, we applied an image evaluation assessment for our pending SAR images and denoised images with image quality assessment. In Figure 5, the fact that the image quality has been improved by over 3.4 to 5 units, during the iteration, is shown. The pending images compared in Figure 5 are reconstructed from full-density rock measurements. We have also illustrated the denoised image quality versus sampling rate in Figure 6. We have also given the statistics of the computational time when our method was applied

on the rock SAR images by a home PC with Intel(R) Core(TM) i7-4790 CPU @ 3.60GHz with 16GB RAM. One can observe that our method executes in milliseconds. The pending images are reconstructed from full density measurements

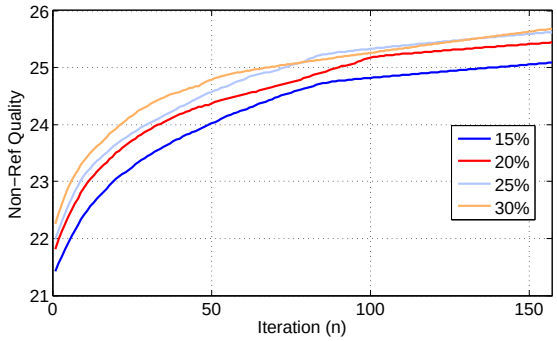

Figure 5. Quality improvements during the iteration in our method.

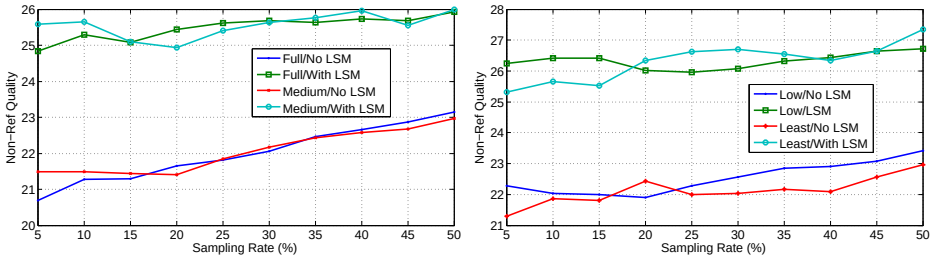

Figure 6. Quality improvements with our method.

From Figure 4, Figure 5, and Figure 6, we can verify the performance of our method. The CS-based method can highly improve the quality of the SAR images reconstructed from low-sampling rate. The computational time is very fast.

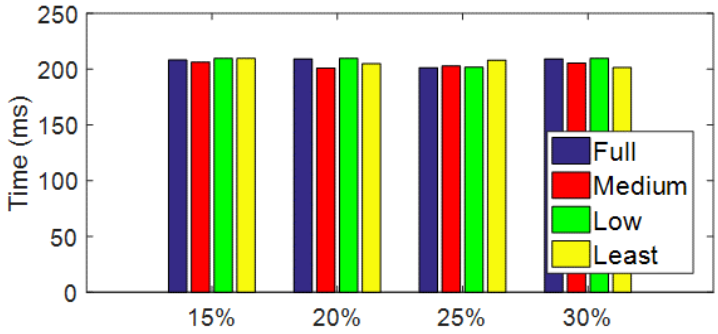

Figure 7. Computational time when our method was applied on the rock SAR images.

4. CONCLUSION

In this study, we have proposed an adaptive level set method algorithm for the SAR images. Simulated and experimental results show that this method could remove the noise in the reconstructed images and significantly improve the quality. This algorithm is designed based on the features of SAR images. We separate the final problem into two sub-problems. The whole algorithm contains two steps with different LSM to solve each sub-problem. With the Non-Ref evaluation criteria, the image quality after our algorithm will improve from 3.5 to 5 units. Noise and aliasing have been effectively reduced. With the LSM and CS-based method, rocks can be identified with only 20%-25% measurements, improved from the 30%-35% measurements that were previously required.

REFERENCES

[1] M. A. Richards, J. A. Scheer, W. A. Holm *et al.*, *Principles of modern radar*. Citeseer, 2010.

[2] M. T. Ghasr, J. T. Case, and R. Zoughi, "Novel reflectometer for millimeter-wave 3-d holographic imaging," *IEEE Trans. Instrum. Meas.*, vol. 63, no. 5, pp. 1328–1336, Jan. 2014.

[3] J. T. Case, M. T. Ghasr, and R. Zoughi, "Optimum 2—D nonuniform spatial sampling for microwave SAR-based NDE imaging systems," *IEEE Trans. Instrum. Meas*, vol. 61, no. 11, pp. 3072–3083, Nov. 2012.

[4] H. Kajbaf, J. T. Case, Z. Yang, and Y. R. Zheng, "Compressed sensing for sar-based wideband three-dimensional microwave imaging system using non-uniform fast Fourier transform," *IET. Radar, Sonar & Navigation*, vol. 7, no. 6, pp. 658–670, May. 2013.

[5] Z. Yang and Y. R. Zheng, "A comparative study of compressed sensing approaches for 3-D synthetic aperture radar image reconstruction," *Elsevier Digital Signal Process.*, vol. 32, pp. 24–33, May 2014.

[6] X. Yang, Y. R. Zheng, M. T. Ghasr, K. M. Donnell, and R. Zoughi, "Microwave synthetic aperture radar imaging using sparse measurement," in *Instrum. Meas. Conf. Proc. (I2MTC), 2016 IEEE International*. IEEE, Jul. 2016, pp. 1–5.

[7] D. L. Donoho, "Compressed sensing," *IEEE Trans. Inf. Theory*, vol. 52, no. 4, pp. 1289–1306, Apr. 2006.

[8] R. Malladi and J. A. Sethian, "Image processing: Flows under min/max curvature and mean curvature," *Graphical models and image processing*, vol. 58, no. 2, pp. 127–141, Dec. 1996.

[9] S. Osher and J. A. Sethian, "Fronts propagating with curvature-dependent speed: algorithms based on hamilton-jacobi formulations," *Journal of computational physics*, vol. 79, no. 1, pp. 12–49, Nov. 1988.

[10] Z. Wang, H. R. Sheikh, and A. C. Bovik, "No-reference perceptual quality assessment of jpeg compressed images," in *Image Process. 2002. Proc. 2002 International Conf. on*, vol. 1. IEEE, Sept. 2002, pp. I–I.

[11] D. Peng, B. Merriman, S. Osher, H. Zhao, and M. Kang, "A pde-based fast local level set method," *Journal of computational physics*, vol. 155, no. 2, pp. 410–438, Jul. 1999.

[12] T. F. Chan and L. A. Vese, "A level set algorithm for minimizing the mumford-shah functional in image processing," *Variational and Level Set Methods in Computer Vision, 2001. Proc. IEEE Workshop on*, pp. 161–168, Aug. 2001.

[13] S. Osher and R. P. Fedkiw, "Level set methods: an overview and some recent results," *Journal of Computational physics*, vol. 169, no. 2, pp. 463–502, May. 2001.

[14] Y. Wu, Y. Huang, and X. Wu, "A equivalent monostatic imaging algorithm for bistatic synthetic aperture radar," in *Synthetic Aperture Radar, 2007. APSAR 2007. 1st Asian and Pacific Conference on*. IEEE, 2007, pp. 94–97.

[15] S. G. Chang, B. Yu, and M. Vetterli, "Adaptive wavelet thresholding for image denoising and compression," *IEEE Trans. Image Process.*, vol. 9, no. 9, pp. 1532–1546, Sep. 2000.

SECTION

2. SUMMARY AND CONCLUSIONS

This dissertation developed an innovative millimeter-wave imaging system capable of producing rapid images using a sparse sampling approach and proposed several CS-based SAR imaging reconstruction methods for the imaging system. The imaging system comprises signal measuring hardware and image reconstruction software. The developed SAR imaging system uses fewer antenna elements, while the resolution size and the quality of the reconstructions are higher than those achieved by conventional SAR imaging systems. The developed imaging system uses electrical switches to replace the raster scanning to speed up the measuring procedure. The software transfers raw, bistatic, non-uniform, under-sampled, wideband SAR measurements to monostatic, uniform, equally-spaced, sparse wideband SAR measurements by several signal preprocessing procedures that have been proven to be accurate and efficient. The CS-based reconstruction method is applied to reconstruct high-resolution-size and high-quality SAR images from the transferred measurements. Several post-processing procedures, such as image denoising and feature detection, also have been outlined in this dissertation. These methods have been proven in simulated and particular experiments, respectively. The innovative millimeter-wave imaging system comprising all the reconstruction methods has shown excellent performance in profoundly reducing the number of measurements, accelerating the scanning time, and maintaining high-quality and high-resolution reconstruction.

This dissertation demonstrated experimental verification of several implementations of 2D imaging in addition to showing that the novel SAR imaging system can reconstruct high-quality images with fewer antenna elements. Furthermore, several high-resolution SAR images that need less than two minutes for measuring and reconstructing with the bistatic configuration model and the proposed method were also demonstrated.

This dissertation analyzed the performance of the image processing methods used in the innovative SAR imaging system. Each of them can be used in the other SAR imaging systems to improve the quality of their reconstruction. This dissertation showed that with the CS-based reconstruction method, only 35% of measurements are necessary for reconstruction. With the proposed detection methods, only 10% of measurements are necessary for detection. When compared to the traditional SAR image reconstruction method, experimental and simulation results illustrate the CS-based method's accuracy, and the computational cost for this method is acceptable. The image post-processing technique for denoising based on an adaptive level set method algorithm for the SAR images also showed its advantages in improving SAR image quality. This denoising method is based on under-sampled SAR images and has low computational cost. Using the denoising method and the first CS-based reconstruction method, the sampling ratio was reduced to only 20%-25%, improving from the previously required 30%-35%. This dissertation also provided the details for mathematic derivation, computational cost analysis, and error estimation for the methods proposed in this dissertation. With the performance analysis for the diverse image reconstructions, the innovative SAR imaging system proposed in this dissertation is proven to be accurate, effective, and efficient for the near-field SAR applications.

APPENDIX A

CS-BASED RECONSTRUCTION METHOD PERFORMANCE ANALYSIS

This dissertation also improves the CS reconstruction method itself. Randomness and sparsity are two essential constraints in CS technology. The randomness has been discussed previously in the radar imaging system section, and this section will analyze the sparsity. Expect the randomness and sparsity. Several usual constraints will also be added to the CS optimization equation to improve the performance, such as total variation. In this dissertation, a new constraint based on image quality has been added to the CS optimization to improve its performance.

Sparsity. A sparsifying transform is an operator mapping a vector of recovered images/signals to a sparse vector where most elements in the sparse vector are zeros. Dr. Candes and Dr. Tao proved that only when the measurements satisfied the restricted isometry property (RIP) conditional is it possible to be perfectly reconstructed for under-sampled measurements. The RIP conditional emphasized the significance of measurement sparsity in CS. In recent years, researchers have proposed extensive sparse operators for sparse image representation. This dissertation applied the sparsifying transformation library possessed in and tested various transformations that have proven robust and effective in sparsifying the real-life images: 1. discrete cosine transform (DCT), 2. wavelet transform with different basis, and 3. identity matrix.

As the central protocol, DCT has been widely used in different applications, such as standard Joint Photographic Experts Group (JPEG) image compression and MPEG video compression. In particular, DCT is a Fourier-related transform similar to the discrete Fourier transform (DFT) but uses only real numbers. There are several different types of DCT that have different computational cost and accuracy. This dissertation tested DCT-II, the most commonly used form, and its formulation is shown in Eq. (A.1).

$$\mathbf{X}_k = \sum_{n=0}^{N-1} \mathbf{x}_n \cos\left[\frac{\pi}{N}\left(n+\frac{1}{2}\right)k\right] \qquad k = 0, \ldots, N-1. \tag{A.1}$$

The wavelet transform is a multi-scale representation of the image and is used in the JPEG-2000 image compression standard. The wavelet transform is similar to the Fourier transform with a completely different merit function or wavelet base. This dissertation tested Beylkin base, Daubechies base, and Symlets base for wavelet transformation.

In DCT or wavelet sparsifying transformation, the principle components are selected in the transformation domain and force other components to zero to create the data on transformation domain sparsity. The computational time of the transformation and the number of zero elements after transformation are two critical conditions to judge the performance of the transformation. Rapid computation and more zeros would profoundly improve the performance of compressed sensing. It should be emphasized that these sparsifying transformations are designed for regular real-life images and the SAR images have its characteristics, in which the performance of the interested sparsifying transformation may be substantially different than when they are applied in the standard real-life image.

To illustrate the difference, this dissertation performed such an experiment on a real-time, fully-sampled SAR rock image. In this testing, the most significant (largest) 5% - 15% coefficients remained and forced others to zeros. The results are depicted in Figure A.1. A raw real-life SAR image has been transformed with identity matrix, DCT, Wavelet-1 (Beylkin base), Wavelet-2(Daubechies base), and Wavelet-3 (Symlets base).

It is apparent that DCT sparsifying transform is not a good choice for the grayscale SAR image, as the DCT reconstructions show deformation. The identity matrix and wavelet transforms have similarly good performance, with slight advantages for the wavelet transform at reconstructions involving 5%-15% of the coefficients. However, the computational costs in three wavelet transforms are much higher than the identity matrix. In compressed sensing iteration, the sparsifying transform and its inverse transform will be computed many times. The accumulated computational cost would increase the reconstruction time. The quantity statics of the computational time and the mean square errors for each reconstruction are shown below.

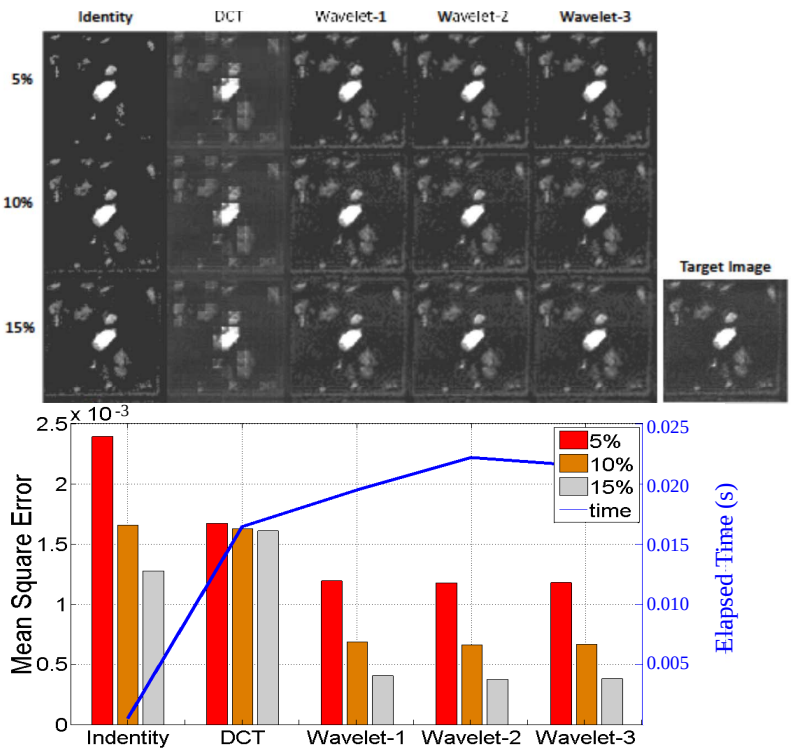

Figure A.1. The testing result for SAR image with different sparsifying transforms.

To balance the image quality and computational cost, this dissertation chose the identity matrix as the sparsifying transformation for this project. However, considering the background of SAR images which have a much smaller reflection rate compared with the interested objects, this dissertation set a threshold Ts for the background measurement zero-forcing the reconstructed images. The threshold is proportional to the mean of the absolute measurement value, $T_s = \alpha_T E\{S\}$, where α is the ratio.

For several more massive and complex targets, using a general average will highly reduce the contrast and details in reconstruction when the reflection ratio drastically changes the whole target and the gap between maximum and minimum is vast. For this situation, local averages replace the general average. The whole specimen under test (SUT) is separated into several small groups, and each group respectively estimates its part average and forces the components smaller than its part average to zero before merging them.

Image quality constraint in CS. In this dissertation, the main purpose for the CS-based reconstruction technology is to improve the reconstruction. However, few papers directly use image quality as a constraint on CS. Most papers only use total variation, which maximizes the absolute gradient for the images instead of the image quality. In this dissertation, a new constraint based on a non-reference image quality metric [56] has been added to the CS optimization problem to replace the common total variation constraint. This constraint is used to maximize the final reconstruction quality, and the total variation is contained in this quality constraint. The details for the gradient of the non-reference quality metric are derived in Appendix. B.

We used the nonlinear conjugate-gradient (CG) descent algorithm with backtracking line search proposed in to solve the CS optimization problem Eq. (B.4). The details for the CG-CS method is illustrated in Algorithm 6.

Algorithm 6 Nonlinear conjugate-gradient iterative algorithm for l_1 optimization

Definition: Sparse measurements $\mathbf{s}$, the Sparse representation domain $\mathbf{\Psi}$, the SAR operator $\mathbf{\Upsilon}$, the Stopping criteria t_{max}; Gradient step size: η, And the estimated recovery image $\hat{\mathbf{g}}$;
Initialization: $t = 0$; $\mathbf{g}_0 = \mathbf{0}$; $\mathbf{m}_0 = \nabla f(\mathbf{g}_0)$; $\triangle \mathbf{g}_0 = -\mathbf{m}_0$
while $(t \geqslant t_{max})$ and $(||\mathbf{g}_t||_2 <$TolGrad $)$ **do**
    $\delta = 1$.
    while $f(\mathbf{g}_t + \eta \triangle \mathbf{g}_t) > f(\mathbf{g}_t) + \alpha\delta \text{Real}[\mathbf{m}_t^* \triangle \mathbf{g}_t]$ **do**
        $\delta = \eta\delta$.
    end while
    $\mathbf{g}_{t+1} = \mathbf{g}_t + \delta \triangle \mathbf{g}_t$
    $\mathbf{m}_{t+1} = \nabla f(\mathbf{g}_t)$
    $\nabla \mathbf{g}_{t+1} = -\mathbf{m}_{t+1} + \dfrac{||\mathbf{m}_{t+1}||_2^2}{||\mathbf{m}_t||_2^2} \triangle \mathbf{g}_t$
    $t = t + 1$.
end while
return $\hat{\mathbf{g}} = \mathbf{g}_{t-1}$.

APPENDIX B

GRADIENT OF THE NON-REFERENCE IMAGE QUALITY OPERATOR

The image quality is a significant feature for the reconstruction. In this project we added one more constraint for the image quality. A non-reference image quality assessment have been proposed in Wang's paper in 2002, 'No-reference perceptual quality assessment of JPEG compressed images'. The quality assessment can be illustrated in (B.1).

$$Q(\mathbf{I}) = \alpha_q + \beta_q B(\mathbf{I})^{\gamma_1} A(\mathbf{I})^{\gamma_2} Z(\mathbf{I})^{\gamma_3}, \text{ where } \mathbf{I} \in \mathbb{R}^{M_i \times M_j} \tag{B.1}$$

where $B = (B_i + B_j)/2$, $A = (A_i + A_j)/2$, and $Z = (Z_i + Z_j)/2$ are three parameters. All of them are the average of horizontal direction and vertical direction shown with i and j subscript, respectively. Their definitions on x-direction are illustrated in (B.2)

$$\begin{cases} B_i = & \frac{1}{M_i(\lfloor M_j/8 \rfloor - 1)} \sum_{x=1}^{M_i} \sum_{y=1}^{\lfloor M_j/8 \rfloor - 1} |d_i(x, 8y)| \\ A_i = & \frac{1}{7}\left[\frac{8}{M_i(M_j-1)} \sum_{x=1}^{M_i} \sum_{y=1}^{M_j - 1} |d_i(x, y| - B_i \right] \\ Z_i = & \frac{1}{M_i(M_j-2)} \sum_{x=1}^{M_i} \sum_{y=1}^{M_j - 2} z_i(x, y) \end{cases} \tag{B.2}$$

where $d_x(x, y) = I(x, y+1) - I(x, y),\ y \in [1, M_y - 1]$ is the difference on y-direction, and $z_i(x, y)$ is zero-crossing (ZC) rate which is defined as

$$z_i = \begin{cases} 1 & , \text{ horizontal ZC at } d_i(m, n) \\ 0 & , \text{ otherwise} \end{cases} \tag{B.3}$$

This dissertation proposes to add the quality metric to the l_1 constrained convex optimization problem (B.4) and replace the TV operator. We proposed the derivation of the gradient of non-reference image quality operator in Algorithm. 7 and shows its relationship between the gradient of the TV operator.

$$\begin{aligned} &\text{minimize} && ||\mathbf{\Psi}\tilde{\mathbf{S}}||_1 \\ &\text{subject to} && ||\mathbf{p} \cdot \mathbf{\Phi}^{-1}\tilde{\mathbf{S}} - \tilde{\mathbf{G}}||_2 < \epsilon_{cs} \end{aligned} \tag{B.4}$$

where $\tilde{\mathbf{S}}$ is the reconstructed image, $\tilde{\mathbf{G}}$ is the interpolated measurements, and ϵ_{cs} controls the fidelity of the reconstruction to the measured data. It should be noticed that all the variables in (B.4) has been vectorizing.

Algorithm 7 gradient of non-reference image quality operator $Q'(\mathbf{I})$

1: The non-reference image quality operator in (B.1): $Q(\mathbf{I}) = \alpha_q + \beta_q B(\mathbf{I})^{\gamma_1} A(\mathbf{I})^{\gamma_2} Z^(\mathbf{I})\gamma_3$, where, $\mathbf{I} \in \mathbb{R}^{M_i \times M_j}$, $B(\mathbf{I}) = \frac{1}{2}(B_i + B_j)$, $A(\mathbf{I}) = \frac{1}{2}(A_i + A_j)$, and $Z(\mathbf{I}) = \frac{1}{2}(Z_i + Z_j)$.

2: Since the γ_3 is much smaller than γ_1 and γ_2, in this study, we just ignore the $Z(\mathbf{I})^{\gamma_3}$ component. Here are the presentations of A_h, A_v, B_h, B_v:

$$\begin{cases} B_i = & \frac{1}{M_i(\lfloor M_j/8 \rfloor - 1)} \sum_{x=1}^{M_i} \sum_{y=1}^{\lfloor M_j/8 \rfloor - 1} |d_i(x, 8y)| \\ B_j = & \frac{1}{M_j(\lfloor M_i/8 \rfloor - 1)} \sum_{x=1}^{M_j} \sum_{y=1}^{\lfloor M_i/8 \rfloor - 1} |d_j(8x, y)| \\ A_i = & \frac{1}{7}\Big[\frac{8}{M_i(M_j-1)} \sum_{x=1}^{M_i} \sum_{y=1}^{M_j - 1} |d_i(x, y| - B_i\Big] \\ A_j = & \frac{1}{7}\Big[\frac{8}{M_j(M_i-1)} \sum_{x=1}^{M_j} \sum_{y=1}^{M_i - 1} |d_i(x, y| - B_j\Big] \end{cases}$$

3: let $\mathbf{I}_1 = \begin{bmatrix} 0 & 0 & \cdots & 0 \\ 1 & 0 & \cdots & 0 \\ 0 & 1 & \cdots & 0 \\ \vdots & \vdots & \ddots & 0 \\ 0 & 0 & \cdots & 1 \end{bmatrix}, \mathbf{I}_2 = \begin{bmatrix} 1 & 0 & \cdots & 0 \\ 0 & 1 & \cdots & 0 \\ \vdots & \vdots & \ddots & 0 \\ 0 & 0 & \cdots & 1 \\ 0 & 0 & \cdots & 0 \end{bmatrix}, \mathbf{a} = [\overbrace{\underbrace{0 \cdots 1}_{8} \; 0 \cdots 1 \; \cdots}^{M_j/M_i}], \mathbf{b} = [\underbrace{1 \; 1 \; \cdots \; 1}_{M_j}]$.

4: With the definitions in step 3, B_i, B_j, A_i, A_j can be rewritten as:(To avoid confusing, we use $\mathbf{x}$ to present the raw image in the following steps):

$$\begin{cases} B_i & = \mathbf{b}^T(\mathbf{x} \cdot (\mathbf{I}_1 - \mathbf{I}_2))^2 \cdot \mathbf{a} \cdot \frac{1}{M_i[\lfloor M_j/8 \rfloor - 1]} \\ B_j & = \mathbf{b}^T((\mathbf{I}_1 - \mathbf{I}_2) \cdot \mathbf{x})^2 \cdot \mathbf{a} \cdot \frac{1}{M_j[\lfloor M_i/8 \rfloor - 1]} \\ A_i & = \mathbf{b}^T(\mathbf{x} \cdot (\mathbf{I}_1 - \mathbf{I}_2))^2 \cdot \mathbf{b} \cdot \frac{8}{7M_i(M_j-1)} \\ & \quad -\mathbf{b}^T(\mathbf{x} \cdot (\mathbf{I}_1 - \mathbf{I}_2))^2 \cdot \mathbf{a} \cdot \frac{1}{M_i[\lfloor M_j/8 \rfloor - 1]} \\ A_j & = \mathbf{b}^T((\mathbf{I}_1 - \mathbf{I}_2) \cdot \mathbf{x})^2 \cdot \mathbf{b} \cdot \frac{8}{7M_j(M_i-1)} \\ & \quad -\mathbf{b}^T((\mathbf{I}_1 - \mathbf{I}_2) \cdot \mathbf{x})^2 \cdot \mathbf{a} \cdot \frac{1}{M_j[\lfloor M_i/8 \rfloor - 1]} \end{cases}$$

5: It is obvious that B_i, B_j, A_i, A_j has similar formulation. When we define $\mathbf{C} = \mathbf{I}_1 - \mathbf{I}_2$, this formulation could be expressed as:

$$f(\mathbf{x}) = \tilde{\mathbf{a}}^T \cdot [(\mathbf{cx}). \times (\mathbf{cx})]\tilde{\mathbf{b}}$$
$$g(\mathbf{x}) = \tilde{\mathbf{a}}^T \cdot [(\mathbf{xc}). \times (\mathbf{xc})]\tilde{\mathbf{b}}$$

.

6: The gradient of $f(\mathbf{x})$, and $g(\mathbf{x})$ are similar. Following steps will only shown the derivation of $\partial f = \tilde{\mathbf{a}}^T[\mathbf{c}\partial\mathbf{x}. \times \mathbf{c}\partial\mathbf{x} + \mathbf{c}\partial\mathbf{x}. \times \mathbf{cx}]\tilde{\mathbf{b}}$.

7: Let $\tilde{\mathbf{z}} = \mathbf{cx}$, and $\partial\tilde{\mathbf{z}} = \mathbf{c}\partial\mathbf{x}$, and the vectorization: $vec\{\partial\tilde{\mathbf{z}}\} = vec\{\mathbf{c}\partial\mathbf{x}\} = (\mathbf{I} \otimes \mathbf{c})vec\{\partial\mathbf{x}\}$, where$\mathbf{I}$ is the identity matrix here.

8: Therefore, $f(\mathbf{x}) = \tilde{\mathbf{a}} \cdot [\tilde{\mathbf{z}}. \times \tilde{\mathbf{z}}] \cdot \mathbf{b}$.

9: Let $\tilde{\mathbf{Y}} = \tilde{\mathbf{z}}. \times \tilde{\mathbf{z}}$.

10: Therefore,

$$\begin{aligned} f(\mathbf{x}) &= \tilde{\mathbf{a}} \cdot \tilde{\mathbf{Y}} \cdot \tilde{\mathbf{b}} \\ \partial f &= \tilde{\mathbf{a}} \cdot \partial\tilde{\mathbf{Y}} \cdot \tilde{\mathbf{b}} \\ &= trace\{\tilde{\mathbf{b}} \cdot \tilde{\mathbf{a}}^T \partial\tilde{\mathbf{Y}}\} \end{aligned}$$

11: Therefore, $\frac{\partial f}{\partial \tilde{\mathbf{Y}}} = \tilde{\mathbf{a}} \cdot \tilde{\mathbf{b}}^T$.

12: Therefore, $\partial f = vec\{\tilde{\mathbf{a}}\tilde{\mathbf{b}}^T\}^T \cdot vec\{\partial\tilde{\mathbf{Y}}\}$.

13: Because, $\partial\tilde{\mathbf{Y}} = \partial\tilde{\mathbf{z}}. \times \tilde{\mathbf{z}} + \partial\tilde{\mathbf{z}}. \times \tilde{\mathbf{z}}$.

14: Therefore, $vec\{\partial\tilde{\mathbf{Y}}\} = 2diag\{vec\{\partial\tilde{\mathbf{z}}\}\} \cdot vec\{\partial\tilde{\mathbf{z}}\}$.

15: Therefore, $\partial f = vec\{\partial\tilde{\mathbf{a}}\tilde{\mathbf{b}}^T\}^T \cdot 2diag\{vec\{\tilde{\mathbf{c}}\mathbf{x}\}\} \cdot (\mathbf{I} \otimes \tilde{\mathbf{c}})vec\{\partial\mathbf{x}\}$.

16: Therefore,

$$\begin{aligned} \partial f &= 2(\mathbf{I} \otimes \mathbf{c})^T \cdot diag\{vec\{\tilde{\mathbf{c}}\mathbf{x}\}\} \cdot vec\{\tilde{\mathbf{a}}\tilde{\mathbf{b}}^T\} \\ &= 2\tilde{\mathbf{c}}^T \cdot (\tilde{\mathbf{c}}\mathbf{x}. \times (\tilde{\mathbf{a}}\tilde{\mathbf{b}})). \end{aligned}$$

The result of Alg.7 actually is equal to the gradient of the total variation operator. Since the gradient of the non-reference operator is a polynomial combination of part of ∂f (also ∂g) and constant values which related to the size of the image, it can be concluded

that the gradient of total variation operator is a part of the gradient of non-reference image quality operator, and optimized the non-reference image quality could be considered as the optimized the total variation simultaneously. In real applications, this constraint could replace the total variant constraint with a proper set of parameters.

APPENDIX C

DETAILS OF MONOSTATIC APPROXIMATION AND ERROR ESTIMATION

In the monostatic approximation procedure, an equivalent transceiver is used to replace the transmitter and receiver, as shown in Figure 3 in Paper I. In the simplest cases, the equivalent transceiver only replace the nearest transmitter and receiver pair, which has the minimum error, and minimum quantity. It is also possible to use extra equivalent transceivers to identify the second of higher nearest transmitter and receiver pairs. This appendix derives the error estimation equation for the monostatic approximation in (C.1).

$$\begin{aligned} err &= \frac{R_r + R_t - 2R}{R_r + R_t} \\ &= 1 - 2\frac{\sqrt{\Delta x^2 + h^2}}{\sqrt{h^2 + (\Delta x + \frac{d}{2})^2} + \sqrt{h^2 + (\Delta x - \frac{d}{2})^2}} \\ &= 1 - 2\frac{\sqrt{(\frac{\Delta x}{h})^2 + 1}}{\sqrt{1 + ((\frac{\Delta x}{h}) + \frac{(d/h)}{2})^2} + \sqrt{1 + ((\frac{\Delta x}{h}) - \frac{(d/h)}{2})^2}} \\ &= 1 - 2\frac{\sqrt{r_x^2 + 1}}{\sqrt{1 + (r_x + \frac{r_d}{2})^2} + \sqrt{1 + (r_x - \frac{r_d}{2})^2}} \end{aligned} \tag{C.1}$$

where $r_x = \frac{\Delta x}{h}$ is the proportion between Δx and h, which is from $0 - 1.5$, and $r_d = \frac{d}{h}$ is the proportion between d and h, from $0.08 - 0.12$ in the proposed imaging system.

The relationship between the error and r_x, r_d is shown in Figure C.1. The error is inverse proportion with r_x and r_d, and is less than -25dB, which is acceptable.

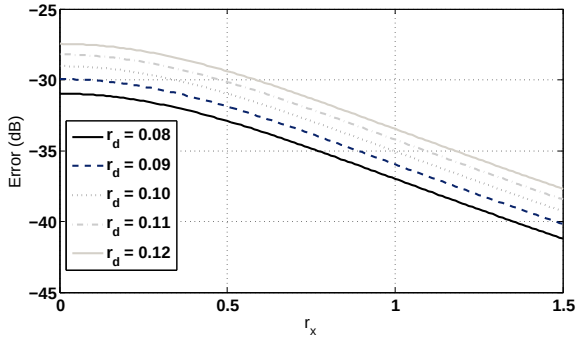

Figure C.1. The relationship between the bistatic error and the r_x, r_d.

In the monostatic approximation, the reconstructions can only consider the equivalent transceiver instead of separately calculating the transmitter and receiver. The accuracy for the monostatic acceptable, while the number of antennas that need to be calculated is reduced by half.

APPENDIX D

PUBLICATION LIST

Journal Paper:

1. **Yang, X.**, Zheng, Y. R., Ghasr, M. T., & Donnell, K. M, "Microwave Imaging from Sparse Measurements for Near-Field Synthetic Aperture Radar." IEEE Transactions on Instrumentation and Measurement 66.10 (2017): 2680-2692.

2. Bi, D., Xie, Y., Ma, L., Li, X., **Yang, X.**, & Zheng, Y. R. "Multifrequency compressed sensing for 2-D near-field synthetic aperture radar image reconstruction." IEEE Transactions on Instrumentation and Measurement 66.4 (2017): 777-791.

3. **Yang, X.**, Zahra. M, Zheng, Y. R., Ghasr, M. T., & Donnell, K. M, "A Low Complexity Image Reconstruction Method for Synthetic Aperture Radar Imaging Systems with Very Sparse Arrays," preparing to submit IEEE Transactions on Computational Imaging, [In preparation]

Conference Paper:

1. **Yang, X.**, Zheng, Y. R., Ghasr, M. T., Donnell, K. M., & Zoughi, R. "Microwave synthetic aperture radar imaging using sparse measurement." Instrumentation and Measurement Technology Conference Proceedings (I2MTC), 2016 IEEE International. IEEE, 2016.

2. **Yang, X.**, Zheng, Y. R., "Synthetic Aperture Radar (SAR) image reconstruction with very sparse measurements." SPIE Paper, 4 - 8 March 2018.

3. **Yang, X.**, Zheng, Y. R., and Ma, L. "Automated cardiac self-gated radial CMRI." Medical Measurements and Applications (MeMeA), 2015 IEEE International Symposium on. IEEE, 2015.

4. **Yang, X.**, et al. "Compressed sensing with non-uniform fast Fourier transform for radial Ultra-short Echo Time (UTE) MRI." Biomedical Imaging (ISBI), 2015 IEEE 12th International Symposium on. IEEE, 2015.

REFERENCES

[1] D. M. Sheen, D. L. McMakin, and T. E. Hall, "Three-dimensional millimeter-wave imaging for concealed weapon detection," *IEEE Trans. Microw. Theory Tech.*, vol. 49, no. 9, pp. 1581–1592, Mar. 2001.

[2] A. S. Milman, "SAR imaging by ω- κ migration," *Int. J. of Remote Sensing*, vol. 14, no. 10, pp. 1965–1979, May. 1993.

[3] S. Kharkovsky and R. Zoughi, "Microwave and millimeter wave nondestructive testing and evaluation — Overview and recent advances," *IEEE Instrum. Meas. Mag.*, vol. 10, no. 2, pp. 26–38, Feb. 2007.

[4] M. Soumekh, *Synthetic aperture radar signal processing*. New York: Wiley, 1999.

[5] J. T. Case, M. T. Ghasr, and R. Zoughi, "Optimum 2—D nonuniform spatial sampling for microwave SAR-based NDE imaging systems," *IEEE Trans. Instrum. Meas*, vol. 61, no. 11, pp. 3072–3083, Nov. 2012.

[6] M. T. Ghasr, J. T. Case, and R. Zoughi, "Novel reflectometer for millimeter-wave 3-d holographic imaging," *IEEE Trans. Instrum. Meas.*, vol. 63, no. 5, pp. 1328–1336, Jan. 2014.

[7] Z. Yang and Y. R. Zheng, "A comparative study of compressed sensing approaches for 3-D synthetic aperture radar image reconstruction," *Elsevier Digital Signal Process.*, vol. 32, pp. 24–33, May 2014.

[8] D. L. Donoho, "Compressed sensing," *IEEE Trans. Inf. Theory*, vol. 52, no. 4, pp. 1289–1306, Apr. 2006.

[9] Z. Wang, H. R. Sheikh, and A. C. Bovik, "No-reference perceptual quality assessment of jpeg compressed images," in *Image Process. 2002. Proc. 2002 International Conf. on*, vol. 1. IEEE, Sept. 2002, pp. I–I.

[10] M. Pastorino, *Microwave imaging*. John Wiley & Sons, 2010, vol. 208.

[11] H. Kajbaf, J. T. Case, Z. Yang, and Y. R. Zheng, "Compressed sensing for sar-based wideband three-dimensional microwave imaging system using non-uniform fast Fourier transform," *IET. Radar, Sonar & Navigation*, vol. 7, no. 6, pp. 658–670, May. 2013.

[12] Z. Yang and Y. R. Zheng, "Near-field 3-D synthetic aperture radar imaging via compressed sensing," in *Acoustics, Speech and Signal Process. (ICASSP), 2012 IEEE Int. Conf. on*. IEEE, Aug. 2012, pp. 2513–2516.

[13] X. Yang, Y. R. Zheng, M. T. Ghasr, K. M. Donnell, and R. Zoughi, "Microwave synthetic aperture radar imaging using sparse measurement," in *Instrum. Meas. Conf. Proc. (I2MTC), 2016 IEEE International*. IEEE, Jul. 2016, pp. 1–5.

[14] Z. Manzoor, M. T. Ghasr, and K. M. Donnell, "Image distortion characterization due to equivalent monostatic approximation in near field bistatic sar imaging," in *2017 IEEE Int. Instrumentation and Measurement Technology Conference (I2MTC)*, May 2017, pp. 1–5.

[15] Y. L. Neo, F. Wong, and I. G. Cumming, "A two-dimensional spectrum for bistatic sar processing using series reversion," *IEEE Trans. Geosci. Remote Sens. Letter*, vol. 4, no. 1, pp. 93–96, Jan. 2007.

[16] I. Walterscheid, J. H. G. Ender, A. R. Brenner, and O. Loffeld, "Bistatic sar processing and experiments," *IEEE Trans. Geosci. Remote Sens.*, vol. 44, no. 10, pp. 2710–2717, Sep. 2006.

[17] O. Loffeld, H. Nies, V. Peters, and S. Knedlik, "Models and useful relations for bistatic sar processing," *IEEE Trans. Geosci. Remote Sens.*, vol. 42, no. 10, pp. 2031–2038, Oct.2004.

[18] Y. Wu, Y. Huang, and X. Wu, "A equivalent monostatic imaging algorithm for bistatic synthetic aperture radar," in *Synthetic Aperture Radar, 2007. APSAR 2007. 1st Asian and Pacific Conference on*. IEEE, 2007, pp. 94–97.

[19] M. Xu and L. V. Wang, "Universal back-projection algorithm for photoacoustic computed tomography," *Physical Review E*, vol. 71, no. 1, p. 016706, Jan. 2005.

[20] I. G. Cumming and F. H. Wong, "Digital processing of synthetic aperture radar data," *Artech house*, vol. 1, no. 2, p. 3, 2005.

[21] D. Bi, Y. Xie, X. Li, and Y. R. Zheng, "Efficient 2-d synthetic aperture radar image reconstruction from compressed sampling using a parallel operator splitting structure," *Digital Signal Processing*, vol. 50, pp. 171–179, 2016.

[22] D. Bi, L. Ma, X. Xie, Y. Xie, X. Li, and Y. R. Zheng, "A splitting bregman-based compressed sensing approach for radial ute mri," *IEEE Trans. on Applied Superconductivity*, vol. 26, no. 7, pp. 1–5, 2016.

[23] D. Bi, Y. Xie, and Y. R. Zheng, "Synthetic aperture radar imaging using basis selection compressed sensing," *Circuits, Systems, and Signal Processing*, vol. 34, no. 8, pp. 2561–2576, Sept. 2015.

[24] E. J. Candès, J. Romberg, and T. Tao, "Robust uncertainty principles: Exact signal reconstruction from highly incomplete frequency information," *IEEE Trans. Inf. Theory*, vol. 52, no. 2, pp. 489–509, Jan. 2006.

[25] B. D. Rigling and R. L. Moses, "Polar format algorithm for bistatic sar," *IEEE Trans. Aerosp. Electron. Syst.*, vol. 40, no. 4, pp. 1147–1159, Oct. 2004.

[26] K. Gröchenig and T. Strohmer, "Numerical and theoretical aspects of nonuniform sampling of band-limited images," in *Nonuniform Sampling*. Springer, 2001, pp. 283–324.

[27] J. Keiner, S. Kunis, and D. Potts, "Using NFFT 3 — a software library for various nonequispaced fast fourier transforms," *ACM Trans. on Mathematical Software (TOMS)*, vol. 36, no. 4, p. 19, Aug. 2009.

[28] J. Bergh and J. Lofstrom, *Interpolation spaces: an introduction*. Springer Science & Business Media, 2012, vol. 223.

[29] F. N. Fritsch and R. E. Carlson, "Monotone piecewise cubic interpolation," *SIAM Journal on Numerical Analysis*, vol. 17, no. 2, pp. 238–246, Jul, 1980.

[30] C. De Boor, C. De Boor, E. U. Mathématicien, C. De Boor, and C. De Boor, *A practical guide to splines*. Springer-Verlag New York, 1978, vol. 27.

[31] M. Lustig, D. L. Donoho, and J. M. Pauly, "Sparse MRI: The application of compressed sensing for rapid MR imaging," *Magnetic Resonance in Medicine*, vol. 58, no. 6, pp. 1182–1195, Oct. 2007.

[32] A. S. Khwaja and J. Ma, "Applications of compressed sensing for SAR moving-target velocity estimation and image compression," *IEEE Trans. Instrum. Meas.*, vol. 60, no. 8, pp. 2848–2860, Aug. 2011.

[33] S. G. Chang, B. Yu, and M. Vetterli, "Adaptive wavelet thresholding for image denoising and compression," *IEEE Trans. Image Process.*, vol. 9, no. 9, pp. 1532–1546, Sep. 2000.

[34] Q. H. Liu and N. Nguyen, "An accurate algorithm for nonuniform fast fourier transforms (nufft's)," *IEEE Microw. and Guided Wave Lett.*, vol. 8, no. 1, pp. 18–20, Jan 1998.

[35] C. D. Austin, E. Ertin, and R. L. Moses, "Sparse signal methods for 3-D radar imaging," *IEEE J. Sel. Topics Signal Process.*, vol. 5, no. 3, pp. 408–423, Jun. 2011.

[36] M. Elad, "Optimized projections for compressed sensing," *IEEE Trans. Signal Process.*, vol. 55, no. 12, pp. 5695–5702, Dec. 2007.

[37] M. A. T. Figueiredo, J. M. Bioucas-Dias, and R. D. Nowak, "Majorization-minimization algorithms for wavelet-based image restoration," *IEEE Trans. on Image Process.*, vol. 16, no. 12, pp. 2980–2991, Dec 2007.

[38] R. C. Gonzalez and R. E. Woods, *Digital image processing,* 3^{rd} *ed.* Addison-Wesley, 2008.

[39] J. Ma, "Improved iterative curvelet thresholding for compressed sensing and measurement," *IEEE Trans. Instrum. Meas.*, vol. 60, no. 1, pp. 126–136, Jan. 2011.

[40] A. Ravelomanantsoa, H. Rabah, and A. Rouane, "Compressed sensing: A simple deterministic measurement matrix and a fast recovery algorithm," *IEEE Trans. Instrum. Meas.*, vol. 64, no. 12, pp. 3405–3413, Dec. 2015.

[41] T. Edeler, K. Ohliger, S. Hussmann, and A. Mertins, "Super-resolution model for a compressed-sensing measurement setup," *IEEE Trans. Instrum. Meas.*, vol. 61, no. 5, pp. 1140–1148, May. 2012.

[42] Y. Tsaig and D. L. Donoho, "Extensions of compressed sensing," *Signal Process.*, vol. 86, no. 3, pp. 549–571, Mar. 2006.

[43] Z. Wang, A. C. Bovik, H. R. Sheikh, and E. P. Simoncelli, "Image quality assessment: from error visibility to structural similarity," *IEEE Trans. Image Process.*, vol. 13, no. 4, pp. 600–612, Apr. 2004.

[44] H. S. Prashanth, H. L. Shashidhara, and M. K. N. Balasubramanya, "Image scaling comparison using universal image quality index," in *2009 International Conference on Advances in Computing, Control, and Telecommunication Technologies*, Dec 2009, pp. 859–863.

[45] D. R. Thompson, D. S. Wettergreen, and F. J. C. Peralta, "Autonomous science during large-scale robotic survey," *Journal of Field Robotics*, vol. 28, no. 4, pp. 542–564, Jun. 2011.

[46] L. Li, W. Huang, I. Gu, and Q. Tian, "Statistical modeling of complex backgrounds for foreground object detection," *IEEE Trans. on Image Process.*, vol. 13, no. 11, pp. 1459–1472, Nov. 2004.

[47] F. P. Preparata and M. Shamos, *Computational geometry: an introduction*. Springer Science & Business Media, 2012.

[48] J. Tropp, A. C. Gilbert *et al.*, "Signal recovery from random measurements via orthogonal matching pursuit," *IEEE Trans. Inf. Theory*, vol. 53, no. 12, pp. 4655–4666, Dec. 2007.

[49] V. Gor, E. Mjolsness, R. Manduchi, R. Castano, and R. Anderson, "Autonomous rock detection for mars terrain," in *AIAA Space Conf. and Exposition*, 2001, p. 4597.

[50] G. C. Feng and P. C. Yuen, "Multi-cues eye detection on gray intensity image," *Pattern recognition*, vol. 34, no. 5, pp. 1033–1046, May, 2001.

[51] M. A. Richards, J. A. Scheer, W. A. Holm *et al.*, *Principles of modern radar*. Citeseer, 2010.

[52] R. Malladi and J. A. Sethian, "Image processing: Flows under min/max curvature and mean curvature," *Graphical models and image processing*, vol. 58, no. 2, pp. 127–141, Dec. 1996.

[53] S. Osher and J. A. Sethian, "Fronts propagating with curvature-dependent speed: algorithms based on hamilton-jacobi formulations," *Journal of computational physics*, vol. 79, no. 1, pp. 12–49, Nov. 1988.

[54] D. Peng, B. Merriman, S. Osher, H. Zhao, and M. Kang, "A pde-based fast local level set method," *Journal of computational physics*, vol. 155, no. 2, pp. 410–438, Jul. 1999.

[55] T. F. Chan and L. A. Vese, "A level set algorithm for minimizing the mumford-shah functional in image processing," *Variational and Level Set Methods in Computer Vision, 2001. Proc. IEEE Workshop on*, pp. 161–168, Aug. 2001.

[56] S. Osher and R. P. Fedkiw, "Level set methods: an overview and some recent results," *Journal of Computational physics*, vol. 169, no. 2, pp. 463–502, May. 2001.

VITA

Xiahan Yang received the B.S. degree in electrical from Tianjin University, in Tianjin, China, in 2009. He received the M.S degree in electrical engineering from Missouri University of Science and Technology (formerly: University of Missouri-Rolla), Rolla, MO, USA, in 2015. He began his Ph.D study in August 2015 at the Department of Electrical and Computer Engineering at Missouri University of Science and Technology, Rolla, MO, USA. His research interests included compressed sensing, image processing, and optimization algorithms. He received his Ph.D. degree in electrical engineering from Missouri University of Science and Technology in December 2018.